Fabrication, Microstructure and Optical Characterization of Transparent Glass Ceramic

M. Tech. Thesis

By
PRABHAT KUMAR DHURVE

DEPARTMENT OF MECHANICAL ENGINEERING
INDIAN INSTITUTE OF TECHNOLOGY INDORE
MAY 2025

Fabrication, Microstructure and Optical Characterization of Transparent Glass-Ceramic

A THESIS

Submitted in partial fulfillment of the requirements for the award of the degree
of
Master of Technology

by
PRABHAT KUMAR DHURVE

DEPARTMENT OF MECHANICAL ENGINEERING
INDIAN INSTITUTE OF TECHNOLOGY INDORE
MAY 2025

INDIAN INSTITUTE OF TECHNOLOGY INDORE

CANDIDATE'S DECLARATION

I hereby certify that the work which is being presented in the thesis entitled **FABRICATION, MICROSTRUCTURE AND OPTICAL CHARACTERIZATION OF TRANSPARENT GLASS CERAMIC** in the partial fulfillment of the requirements for the award of the degree of **MASTER OF TECHNOLOGY** and submitted in the **DEPARTMENT OF MECHANICAL ENGINEERING, Indian Institute of Technology Indore**, is an authentic record of my own work carried out during the time period from June 2024 to May 2025 under the supervision of **Dr. Surya Mohan Gupta, Head, Optical Glass and Ceramics Lab, RRCAT Indore** and **Prof. Pankaj R Sagdeo, Professor, Department of Physics, IIT Indore.**

The matter presented in this thesis has not been submitted by me for the award of any other degree of this or any other institute.

27/5/25

Signature of the student with date
(PRABHAT KUMAR DHURVE)

This is to certify that the above statement made by the candidate is correct to the best of my/our knowledge.

27/5/25

Signature of the Supervisor of
M.Tech. thesis #1 (with date)
(Dr. SURYA MOHAN GUPTA)

27/5/2025

Signature of the Supervisor of
M.Tech. thesis #2 (with date)
(Prof. PANKAJ R. SAGDEO)

PRABHAT KUMAR DHURVE has successfully given his/her **M.Tech. Oral Examination** held on **9th May 2025**.

27/5/25 27/5/2025

Signature(s) of Supervisor(s) of
M.Tech. thesis
Date:

Convener, DPGC
Date: 02-06-2025

Signature of PSPC Member #1
Date:

Signature of PSPC Member #1
Date:

ACKNOWLEDGEMENT

I would like to express my deepest gratitude to my supervisors, **Dr. Surya Mohan Gupta** and **Prof. Pankaj R Sagdeo**, for their invaluable guidance, encouragement, and continuous support throughout the course of this work. Their insights and expertise have been instrumental in shaping both the direction and the quality of this research.

I would also like to sincerely thank **Dr. Sunil Verma**, Head of **Photonic Materials Technology Section (PMTS)**, for providing me with the opportunity to carry out this research within **PMTS**, and for his strong support and leadership.

I am especially thankful to **Shri Sanjib Karmakar** for his unwavering support, involvement, and technical guidance. His contribution throughout the course of this work has been no less than that of a co-supervisor.

I express my hearty thanks to **Shri Sushil Kumar Pathak** for his constant suggestions that helped me to gain stronger practical hands-on experience.

I would like to thank **Dr. Gurvinderjit Singh, Dr. Rajiv Bhatt, Dr. Moh. Sohrab, Dr. S. Satapathy, Mrs. Rachna Selvamani** for their help in this project. I am also thankful to **Shri Prem Kumar and Shri S. Markam** for their constant help during the whole project. I am thankful to all members of PMTS Division.

I am also grateful to all my friends who have been the motivating force behind the successful completion of this work and have contributed directly or indirectly to this thesis.

Finally, I extend my heartfelt gratitude to all those who, directly or indirectly, contributed to the successful completion of this research.

Prabhat

Abstract

Over the past few years, polycrystalline Nd:$Y_3Al_5O_{12}$ (Nd-YAG) ceramic has replaced single crystal from solid state laser because of the possibility of higher at% Nd-doping and ease of fabrication. Development of transparent ceramic becomes more challenging with increase in size. The laser active Nd-ion when added in glass matrix as laser host is better in term of large size fabrication but Nd-glass has poor thermal conductivity compared to YAG crystal. Aim of the present work is to combine size advantages of Nd-glass with excellent thermal conductivity of YAG by precipitating YAG phase in glass. A suitable Nd-doped silicate glass composition based on ytterium-lithium-aluminum-silicate is fabricated having absorption coefficient 0.72 cm^{-1} and ~ 75 % transmission at 1061 nm wavelength. All the major transition observed in the absorption spectra are assigned based on the transition from the ground state $^4I_{9/2}$ to the crystal field state as marked. Emission spectra of Nd-glass revealed a broad peak near 1061 nm when excited with 585 or 808 nm wavelength. It is observed that absorption and emission peaks are broad, which is consistent with the Nd-ions in glass matrix. The change in thickness of Nd-glass (~ 2mm) is measured to determine the thermal expansion coefficient ~ 8.0 x 10^{-6} /^oC. Thermal treatment is given to a section of the glass sample at different temperature (900-1450 ^oC) in air for 1-6-hour dwell. The phases precipitation sequence is studied using X-ray diffraction technique. The β-spodumene ($LiAlSi_2O_6$) phase is precipitated at the surface first around 950 ^oC and then $Y_2Si_2O_7$ phase in the bulk around 1050 ^oC, followed by YAG phase around 1100 ^oC. Single major YAG phase is successfully observed in the 1350 ^oC for 6 hours heat treated PD-1350GC sample. Microstructure and composition investigation has revealed these phase in the glass matrix, whose composition is modified accordingly. Vibrational spectroscopic investigation has also revealed additional absorption band consistent with the phase analysis. Sudden change in the thermal expansion and mechanical hardness measured on the heat treated samples are consistent with this phase evolution sequence. Optical properties measurement clearly shows all the emission peak related to Nd-ions in glass matrix. An extra peak is observed for PD1350GC sample, which is found to be characteristics R-line of Alumina. At present the origin of these peaks are not known.

List of Content

References

List of Figures

List of Table

ACRONYMS

YAG	Yttrium Aluminum Garnet
YAP	Yttrium Aluminum Perovskite
LED	Light Emitting Diode
FWHM	Full Width at Half Maximum
XRD	X-ray Diffraction
SEM	Scanning Electron Microscope / Microscopy
DRS	Diffuse Reflectance Spectroscopy
FTIR	Fourier Transform Infrared Spectroscopy
PL	Photoluminescence
CL	Cathodoluminescence
NBO	Non-Bridging Oxygen
LAS	Lithium Aluminium Silicate
DTA	Differential Thermal Analysis
DSC	Differential Scanning Calorimetry
EDX	Energy Dispersive X-ray
UV-VIS	Ultraviolet–Visible

Chapter 1

Introduction

1.1 Introduction

Neodymium doped yttrium aluminum garnet (Nd-YAG) laser is a most popular solid state laser because of its high emission cross section with long spontaneous emission lifetime, high damage threshold, good mechanical strengths, high thermal conductivity and consequent low thermal distortion of the laser beam. These properties prove its unquestionable supremacy in a variety of laser applications. Nd-YAG possesses a blend of properties favorable for laser operation. The YAG host is hard, possibility of fabricating good optical quality material with ease and has a high thermal conductivity. Moreover, cubic structure of the YAG supports a narrow fluorescent line width, which is responsible for low threshold and high gain for laser operation. In Nd-YAG, neodymium substitution for trivalent yttrium site require no charge compensation. There are three well known solid- state host materials: single crystals, glasses and polycrystalline, and among them Nd:YAG single crystal is the most extensively used laser gain media because of minimal scattering loss.

Over the past few years, ceramic laser is becoming a fast growing field of research and has challenged the monopoly of single crystal as laser host material. Polycrystalline ceramic laser materials have shown laser oscillations comparable to those of single crystals, when the scattering loss is minimized using advanced powder processing and controlled sintering conditions. Ikesue et al. [1] were the first to establish the option of using Nd:YAG ceramics with the necessary optical properties for laser applications. Since then, polycrystalline transparent Nd:YAG ceramics have attracted much attention because of greatly improved optical quality. Numerous recent works have presented that transparent Nd:YAG ceramics are comparable or even better than a single crystal grown by Czochralski method. Ceramic Nd:$Y_3Al_5O_{12}$ (Nd-YAG) lasers have been reported with slope efficiencies comparable with single crystal. Polycrystalline Nd-YAG ceramic up to 3 at.% dopant concentration without much attenuation losses has already been fabricated. Since 1995 researchers have attempted to fabricate ceramic Nd-YAG with low scattering loss and large size [2]. A laser output was obtained in these ceramics which had sufficiently low 0.0009 cm^{-1} scattering loss. It has been possible to attain 99.9% of theoretical density, 10% higher hardness, five times more fracture toughness than single crystal YAG in polycrystalline ceramic. A slope efficiency of 28% with a 600 mW laser diode end-

pumping scheme was reported in 1998-99. Using virtual pump source pumping system, output power 31W at 1064nm was demonstrated under 290W/808 nm pumping in 2000 [3]; output power 72W and 1.46kW at 1064nm was reported later for side pumping Nd-YAG polycrystalline rod in 2001/2002. These Nd-YAG ceramic demonstrated 58.5% laser slope efficiency and up to 1.4 kW of output power laser oscillation characteristics equivalent to those of Nd-YAG single crystal. The Nd-YAG ceramic rods were developed using the nano-crystalline technology and vacuum sintering method. Nano-size spherical particles of starting reagents with least size distribution must be used to fabricate transparent Nd:$Y_3Al_5O_{12}$ (Nd-YAG) ceramic for its laser application. It is utmost important to control agglomeration within the ultra-fine particles. Fine particles tend to aggregate as clusters of primary particles bonded strongly (hard agglomeration) or weekly (soft agglomeration) with interconnecting network of pores. Hard agglomerated powder results in non-uniform density distribution in the pressed disk. Vacuum sintering results into the disk with lots of porosity, which is due to reduce sintering activity. Number of factors which cause light scattering, e.g., scattering by pores or second phase at grain boundaries, absorption and surface roughness, are required to be controlled stringently. Development of transparent ceramic is a painstaking and challenging problem and it becomes a highly tedious job with increase in size.

On the other hand, Nd-glass material is well known as a laser host for high energy laser development. Ease of fabrication along with flexibility in size and excellent optical quality makes Nd-glass lasers quite useful to deliver high laser energy for advanced research fields. The glass host is known to produces inhomogenously broadenend emission lines which is an advantage in Q-switched lasers. It is possible to develop large size homogenous glass with index of refractive variation less than $\pm$ 0.8 x 10^{-6} across 2.5 cm section. Index of refraction of glass can be varied between 1.5 to 2.0 by varying the glass base. Neodymium in silicate, phosphates, germinates and borates glass has been reported to lase [4]. The laser light loss in the transparent glass is mainly due to the absorption by the transition metal ions contaminants. Since the laser Nd-ion emits in the near infrared, Ni, Co, Cu, Fe and V impurities present in the glass results in higher absorption coefficient. The most serious contaminant in glass is Fe^{2+}, which has been reported to give an absorption of 0.1% / cm at 1.06 micron for a concentration of $5x10^{16}$ ions/cm^2. This problem can be

overcome easily by taking high purity starting reagents and powder processing in the clean atmosphere. Another major drawback of glass is its low thermal conductivity, which impose limitation on the size that is needed for continuous wave operation with high repetition rate. The present work is aimed to combine the ease of processing of glass with the superior properties of crystalline ceramics by developing glass-ceramic having Nd-YAG precipitated phase. Investigation of glass-ceramic, which contains Nd-YAG crystals in a glass matrix is also scantly reported in the literature. This approach is speculated to have high mechanical strength, better control over thermal expansion and higher thermal conductivity over parent glass. It is also anticipated that the transmission property of the glass will be affected by the size and concentration of Nd-YAG phase present inside the glass. It is already known that glass-ceramic may transmit light if the crystallites are much smaller than the wavelength of transmitted light. It is also easier to control the precipitated (Nd-YAG) crystallite size through controlled nucleation and growth in glass. The purpose of this study is to investigate the phase evolution inside the Nd-doped silicate glass by thermal treatment at varying temperature (700-1450 ^{o}C) and also by varying dwell time (1-6 hours) at a specific temperature. The phase sequence will be characterized by X-ray diffraction and optical properties of heat treated glass will be correlated with the phase.

Chapter 2

Literature Survey

1.1 Literature Survey

Development of single Er-doped YAG phase in suitable glass matrix is first time reported by Prof. Tanabe group in a series of papers published in reviewed journals [5]. For this, a glass in Y_2O_3-Al_2O_3-SiO_2 based system was chosen. Phase evolution was investigated using X-ray diffraction and single phase YAG crystal was demonstrated to form above 1350 ^oC. Microstructure and compositional studies revealed the incorporation of Er-ions in the YAG micro-crystals. Optical characterization of the glass and glass-ceramics revealed a broad band photoluminescence in the 1450-1670 nm range, which is due to $^4I_{13/2}$ to $^4I_{15/2}$ transition in the Er-doped YAG crystal.

Phase-selective excitation by a field-emission electron gun revealed an Er-doped YAG phase homogeneously distributed in glass. The intensity of cathodoluminescence (CL) for $^4S_{3/2}$ to $^4I_{15/2}$ transition of Er^{3+} reported to differ a large extent between the glass matrix and precipitated phase. The spectral peaks of the phase with higher CL intensity were observed in Er-doped YAG crystal. The lower CL intensity phase is found to be glassy phase, which included a small amount of YAG crystals. The CL from Er-ion in the glass phase was not detected [6], implying incorporation of almost all the Er-ions into YAG phase. The calculated quantum efficiency in the YAG phase was reported to about 100 times as large as that in the glass phase.

Optical transmission is expecting to reduce due to the phase precipitations inside the glass matrix. Further improvement for increasing the transmission is being sought worldwide in this field. Another challenge is the incorporation of other ions of glass components in the precipitated phase, which requires a procedure optimization investigation in details.

In order to control the transmission, an original paper [7] published on transparent glass-ceramic was found interesting. It was reported that glass-ceramic materials will transmit visible light when following conditions are met: (a) the size of crystallites are smaller than the wavelength of visible light, or (b) smaller optical anisotropy (birefringence) within the crystals and refractive index difference between glass and crystals should be very small. It was also reported that these conditions are achieved when solid solutions (ss) of β-quartz, spinel, and mullite are the major crystalline phases in several alumino-silicate glass-ceramic systems. The mullite and spinel transparent glass-ceramics contain considerable glassy phase but are characterized by excellent transparency, even after long periods thermal exposure above 1000 ^{o}C. Transparency is generally due to the extremely fine crystallite size (much smaller than the wavelength of visible light) of these glass-ceramics but if the major precipitated phase attains crystal sizes approaching 1 μm, the optical isotropy of the precipitated phase becomes a critical factor allowing transparency.

Depending upon the precipitated phase, the glass-ceramics can be distributed into three areas: ultra-low expansion materials, refractory, high electrical resistivity--low dielectric loss materials and colourless materials. These three material groups are all characterized by thermal shock resistance, high crystallinity, brilliant chemical robustness, and susceptibility to mechanical strengthening by ion-exchange methods. Thus, suitable heat treatment not only control the transmission but other mechanical or thermal properties also.

Polycrystalline materials formed in this manner are reported to have several distinct advantages over glasses. The most important property of the glass-ceramic is their ability for exceptionally low thermal expansion. Essentially zero or even negative expansion coefficients are fabricated over many temperature ranges with materials whose chemical composition and crystalline structure are suitable. There is another property, thermal stability in transparent glass-ceramics, are observed to show improvement over glasses. The solidus temperature of the glass-ceramic is considerably higher than the softening point of a glass of similar bulk composition.

Potential applications for transparent crystalline materials capable of being shaped by the glass-forming process are also reported. For consumer and laboratory ware, thermal and mechanical shock-resistance are important requirements. Thermal

stability is a major requirement for high temperature lamp applications. Similarly, for reflective optic applications, the extremely low thermal expansions of certain transparent glass-ceramics are an important criterion. Ability of good optical polish in very fine-grained materials is another advantages for its reflective application.

A novel process for preparing very-high-alumina glasses and nanoscale glass - ceramics was reported [8]. It is known that Al_2O_3 is a network-former in conventional silicate glasses but alone it cannot be obtained as a bulk glass. In order to get, glasses comprising continuously linked [AlO_x] polyhedral very fast cooling conditions are necessary but only small article (mm in size) could be obtained. However, it is appropriate to prepare bulk, or monolithic, alumina-rich glasses, with the outlook of superior mechanical, chemical and optical properties.

In this report, glass microspheres were synthesized by a flame-spraying technique in which the precursors were fed into a high-temperature H_2–O_2 flame, in order to produce molten particles, which were quenched in water at a projected cooling rate of 10^3K/s. The size of flame-sprayed beads was less than 140 μm in diameter. Densification of beads by pressure less sintering or hot pressing was conducted in a graphite furnace with a nitrogen atmosphere resulted in transparent glass-ceramic.

With this approach, fully dense bulk articles in net shape are reported through viscous sintering of glass microbeads. Additional heat treatment given to the consolidated transparent glasses converted it to fully crystallized transparent glass-nano-ceramics with similar hardness of alumina. This method is important because it avoids the unachievably high applied pressures (more than 1 GPa) that may require in most cases to prepare nano-crystalline ceramics by sintering, due to the coexisting nature of densification and grain growth under pressure-less conditions.

Development of transparent YAG-based ceramics by pressure less nano-crystallization of Y_2O_3–Al_2O_3 bulk glasses was reported [9]. The mixed 60–200 mg powder having 74 mol% Al_2O_3–26 mol% Y_2O_3 composition was melted by a CO_2 laser at ~2000 °C. To ensure homogeneity, the sample was kept in molten state for about 10–20 s. Switching off the laser then prompted rapid cooling (~300 °C/s) and led to glass beads with a diameter of ~2–5 mm, which were polished into disks (~1 mm thickness) and then heat treated in an open-air atmosphere muffle furnace using a

temperature between 950 and 1100 °C. The glass beads were fully crystallized into transparent ceramics. Appropriate glass crystallization temperatures were reported to determine from differential scanning calorimetry measurements performed at a heating rate of 10 K/ min, using argon as a purging gas and with alumina pans as sample holders. Microstructure investigation of the resulting ceramics showed a fine grains composed of YAG nanocrystals (77 wt.%) separated by small Al_2O_3 crystalline domains (23 wt.%). These biphasic ceramics reveal improved hardness and transparency from the visible up to the near infrared ranges (6 μm) compared to YAG single crystal and transparent ceramics. The hardness of nano-ceramics (YAG-Al_2O_3) is 10% higher than that of single crystals YAG. The combination of these mechanical and optical properties, along with its simple, cost-effective, and inventive preparation method, is reported to motivate the development of advanced materials with possible applications in wide optical fields such as lenses, scintillators, and phosphor converters in high-power white-light LED and laser diode.

The defect induced photoluminescence (PL) peak in α-Al_2O_3 is a complex subject. There are reports in which the PL spectrum discloses a strong red luminescence at 693 nm and three small-shoulder emission bands at 677, 706 and 712 nm, respectively. The sample preparation is directly linked to this rare phenomenon. In one of the samples, a thin Al foil (0.1 mm) was heated to 450 °C in a vacuum-annealing furnace for 30 minutes to release the stress in the foil [10]. Then, the Al foil was heated to 1300 °C in air for eight hours and finally cooled to room temperature. In the second sample, Laser surface modification of plasma sprayed alumina coatings was carried out.

For the first sample, the PL spectrum displays a strong red emission band centered at 693 nm and microstructure investigation revealed highly ordered α-Al_2O_3 micro cones, which were produced by a facile thermal oxidation method. Raman spectrum shows [11] that the Al_2O_3 micro cones match better with single crystal than bulk Al_2O_3, revealing a good crystalline nature. It was reported that variation in inhomogeneous tensile stress of the micro cones resulting in variances in local symmetry of the crystal causing the three unusual emission bands

For the second sample, impurities related to trace quantities of Cr-ions may be responsible for the presence of PL emission peak at 693nm. In high density alumina,

Cr-ions residing in an octahedral coordinated oxygen environment emit sharp R1 and R2 lines at 1.785 and 1.789 eV, respectively, with energy difference of 0.004 eV. Thus a small step scan should be used for determining these R1 and R2 lines in PL-spectra.

Optical properties of Nd_2O_3 doped Al_2O_3 translucent ceramics, which were fabricated [12] using the well-known solid-state reaction and vacuum sintering, revealed the strong absorption peak at around 800 nm with an absorption cross section 3.25 $x10^{-20}$ cm^2 corresponding to the emission wavelength of the commercial laser diode (LD). The PL spectrum of the Nd-3þ:Al_2O_3 showed the characteristic absorption and emission bands of Nd-3þ ions in the host matrix at 1054 nm. The FWHM and the emission cross section of the peak of the material were reported to be 7.53 nm and 1.38 10^{-19} cm^2. There are strong absorption band around 585nm which was not used for the excitation in the emission spectrum investigation for this sample.

Chapter 3

Theoretical Background

3.1 Lasers

Laser is an acronym for "light amplification by stimulated emission of radiation". Lasers generate visible or invisible light depending upon stimulated emission of electromagnetic radiation. Lasers are distinguished from other light sources by their coherence, which produces highly directional and powerful beam of electromagnetic radiation through a process called optical amplification which is based on the stimulated emission of photons.

3.2 Solid state Laser Materials

In solid state lasers, the gain medium is either single crystal, polycrystalline or glass. Mostly, laser crystals are single crystals and are doped with either trivalent rare earth ions or transition metal ions, which are responsible for amplifying light at the laser wavelength via stimulated emission, when energy is supplied to the crystal via absorption of pump light.

3.2.1 Laser-active dopants

The most common laser-active rare earth ions are Nd, Yb, Er, Tm and Ho-ions in 3+ ionic state. When these ions are doped in certain host crystal to generate some typical emission wavelengths as reported in Table 3.1.

Table 3.1: Typical emission wavelengths most common laser-active rare earth ions

Ion	Host crystals	Important emission wavelengths
neodymium (Nd^{3+})	$Y_3Al_5O_{12}$ (YAG), $YAlO_3$ (YALO), YVO_4 (yttrium vanadate), tungstates ($KGd(WO_4)_2$, $KY(WO_4)_2$)	1064, 1047, 1053, 1342, 946 nm
ytterbium (Yb^{3+})	YAG, tungstates (e.g. KGW, KYW, KLuW), YVO_4, borates	1030, 1020–1070 nm
erbium (Er^{3+})	YAG	2.9, 1.6 µm

Ion	Host crystals	Important emission wavelengths
thulium (Tm^{3+})	YAG	1.9–2.1 μm, 1.47 μm, 2.3 μm
holmium (Ho^{3+})	YAG	2.1, 2.94 μm

3.2.2 Properties of Host crystals

The lasing wavelength, upper-state lifetime, bandwidth, transition cross-sections of pump and laser transitions depends upon the host medium. A suitable crystal should have the following important properties for laser host application.

- Should have a good transparency, optical homogeneity, low absorption and scattering in the wavelength of laser radiation.
- Energy transfer processes like non-radiative transitions and thermal population of lower laser level should be minimum.
- Should tolerate maximum doping concentration without quenching effect.
- Should have high thermal conductivity, low thermo-optic coefficients and high resistance to mechanical stress for high-power lasers.
- Crystal structure should be iso-symmetric.
- Material should have high damage threshold in terms of pulse peak intensity.

There is an extensive range of crystalline media, which are known for their important atomic constituents and crystalline structures.

- Garnets such as $Y_3Al_5O_{12}$ (YAG), $Gd_3Ga_5O_{12}$ (GGG), and $Gd_3Sc_2Al_3O_{12}$ (GSGG): hard and chemically inert materials, optical isotropic, with high thermal conductivity.
- Sapphire (Al_2O_3) (e.g. for titanium–sapphire lasers) and aluminates such as $YAlO_3$ (YALO, YAP) for neodymium doping: high hardness and thermal conductivity, anisotropic.
- Sesquioxides such as Y_2O_3, Sc_2O_3: isotropic, high hardness and thermal conductivity.

- Vandata such as YVO_4 and $GdVO_4$: exceptional laser cross-sections of Nd^{3+}, anisotropic.
- Chalcogenides such as ZnSe or ZnS for mid-infrared lasers

For a given dopant and host medium, the doping concentration, uniform doping, level of unwanted impurities, and the optical homogeneities are other important parameters, which are necessary for high energy lasers. Crystals have higher transition cross-sections, higher thermal conductivity, smaller absorption and emission bandwidth, compared with doped glasses,

3.3 Laser glasses

Laser-active glasses are optical silicate and phosphate glasses, which are doped with laser-active trivalent rare earth ions such as Nd^{3+}, Er^{3+}, Yb^{3+}, Pr^{3+}, Tm^{3+} or Ho^{3+}. Laser glasses in cuboids or cylindrical rods having anti-reflection coated end faces are usually used as gain media. Glasses are generally optically isotropic and have the similar optical properties as of laser crystals. The refractive index of laser crystals is higher than that of the glasses. Rare-earth-doped laser crystals often display distinct laser and pump transitions (few nm bandwidth). Laser glasses typically have much broader transitions with tens of nanometers bandwidths. This difference arises due to the presence of surrounding ions around laser active ions. In laser crystals, the laser-active ions see the same surroundings because it occupies a specific site of the crystal lattice. On the other hand, glasses compromise different environments to these laser active ions, producing strong inhomogeneous broadening . Broad bandwidth of pump transitions is advantageous because tight wavelength tolerances for the pump source is not a necessity. Broadband laser transitions are also useful for wavelength tuning of lasers and also required for the producing ultrashort pulses.

The strong microscopic disorder in glass results to a poor thermal conductivity, which is detrimental in high-power lasers. It can cause not only thermal fracture, but also other defects like thermal lensing and thermal depolarization.

Laser glasses are fabricated in a similar way as optical glasses, only exception is the addition of some laser-active substance. The precise chemical composition of a laser glass is frequently not reported in great detail. One may only know that it is a potassium-aluminum-phosphate glass. Laser glasses can be fabricated in very large

size with good optical quality. In contrast, the growth of large laser crystal is challenging and time-consuming. However, now a days, there are ceramic laser gain media, which is replacing single crystal and can be synthesized in large sizes similar to laser glasses.

3.4 Laser gain ceramic material

A ceramic is an inorganic, nonmetallic solid prepared by the action of heat and subsequent cooling. It is anticipated that optical translucency in ceramic could be achieved by reducing the pores and controlling the microstructure. Ceramic laser has thermal conductivity, mechanical strength and large and homogeneously broadened emission cross section than that in single crystal laser.

The major advantages of ceramics over single crystals are:

- As in case of single crystal, no tedious growth is required that makes them less expensive.
- Ceramic laser can be made in larger size as compared to single crystal laser. This is the biggest advantage of ceramic laser over single crystal laser.
- Ceramics can accommodate comparatively higher concentration of dopants, allowing the flexibility in pumping wavelength.
- Dopant concentrations are highly homogeneous in ceramics and can be controlled precisely.
- Firing of ceramic microstructure requires temperature nearly $3/4^{th}$ of the melting temperature.
- Ceramic gain medium can be made in any desired shape.
- Multiple samples can be fired in single furnace at the same time and this saves time.

3.5 Nd: YAG System

Yttrium Aluminum Garnet (YAG) is the host material. The trivalent Nd is the dopant. The gain media for the solid state laser essentially requires high thermal conductivity, ease of fabrication and chemical stability. In addition, following are the critical and indispensable characteristics from lasing point of view:

- Lower lasing threshold
- Stable operation in both continuous and pulse oscillation modes
- A larger product of emission cross section and fluorescence lifetime
- Excellence in laser energy-conversion efficiency

YAG is a host medium which satisfies above mentioned favorable properties, particularly for high-power lasers and Q-switched lasers emitting at 1064 nm and thus is used widely in industrial applications including semiconductor industry, steel industry as well as medical industry. It is unique because of the range of elements that can substitute into the structure. Few selected properties of YAG host material are summarized in table 3.2.

Table 3.2: Properties of YAG host material

Optical Properties	
Refractive Index	1.817 at 1064 nm
Pump Band	808.6 nm
Fluorescence Lifetime	230 μs at 1.0 at% Nd
Thermal Properties	
Thermal Conductivity (20^{o}C)	0.129 W/cm.K
Non Linear Index	3 x 10 $^{-13}$esu
Specific Heat	0.59 J/g.K
Linear Expansion Coefficient	8.2 x 10^{-6} /K <100> 7.7 x 10^{-6} /K <110> 7.8 x 10^{-6} /K <111>
$\Delta n/\Delta t$	+8.9 x 10^{-6} /K
Physical Properties	
Molecular Weight	595.3 g/mol

Crystal Structure	Cubic/Garnet
Lattice Constant	1.201 nm
Melting Point	1970^{o}C
Density	4.55 gm/cm^3
Mechanical Properties	
Young's Modulus	282 GPa (45 x 10^6 psi)
Tensile Strength	280 MPa

3.5.1 Structure of Nd: YAG

YAG ($Y_3Al_5O_{12}$) has a cubic structure (space group Ia3d or O_h^{10}) with 160 atoms (8 formula unit) per unit cell and lattice constant =1.2001 nm where Y^{3+} (0.102nm) occupies dodecahedral coordinated 24(*c*) sites. Al^{3+} occupies two crystallographically dissimilar sites: tetrahedral coordinated 24(*d*) sites (0.039 nm) and octahedral coordinated 16(*a*) sites (0.054 nm). O^{2-}occupies the 96(*h*) sites that make up the vertices between the cation polyhedron. Each O^{2-} is shared between, one Al^{3+} tetrahedron, two Y^{3+} dodecahedra and one Al^{3+} octahedron. Fig. 3.1 below shows the coordination of each cation site schematically. The dodecahedral coordinated 24(*c*) site can accommodate the entire Lanthanide series (Ce-Lu) and many are important optically active ions for laser applications.

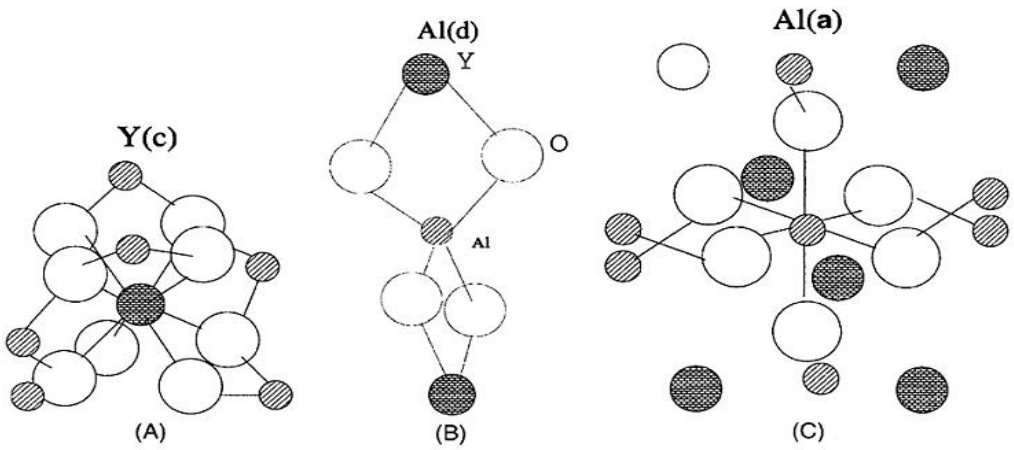

Fig. 3.1: Coordination of Y and Al present in cubic structure.

When YAG is doped with trivalent neodymium, neodymium atoms substitute for trivalent yttrium atoms and hence no charge compensation is required. In laser technology, Nd^{3+} ion is widely used as the laser-active dopant in single crystal, polycrystalline and glass gain media.

The $4F_{3/2} - 4I_{11/2}$ transition of Nd^{3+} has the largest cross section of all active ions, thus it displayed laser operation in the largest number of host crystals and glasses. Optical pumping of the $4F_{3/2}$ level is also efficient due to the large number of closely spaced levels at higher energy levels causing absorption in the visible and near infrared.

3.5.2 Excitation Mechanism in Nd:YAG

Nd:YAG has got a four level gain medium that offers significant laser gain even for moderate excitation levels and pump intensities. Fig. 3.2 shows the energy level diagram of Nd:YAG laser. It has four energy levels. Nd^{3+} ions have two absorption bands and excitation is done by optical pumping either using arc lamp or pump lamp for continuous wave and pulse modes.

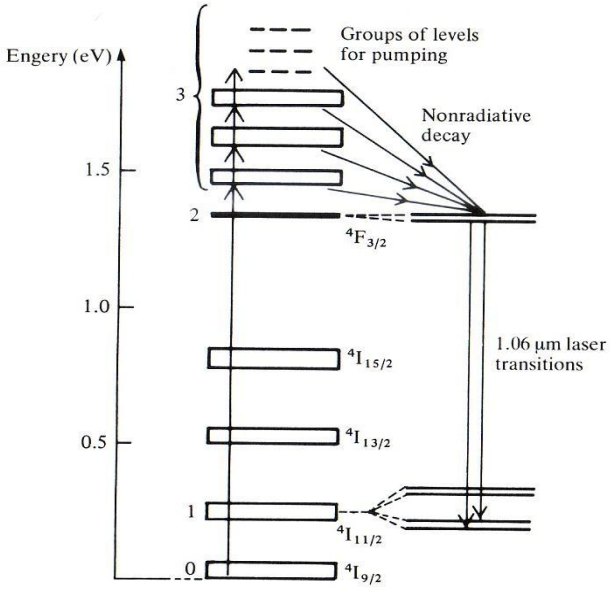

Fig. 3.2: Energy level diagram of Nd: YAG

On pumping, Nd atoms are raised to higher energy pump band $^4F_{5/2}$ from the ground state by absorbing photons impinged over them. Lifetime at this state is very less (10^{-8}s) and after this time atoms decay spontaneously to upper laser level $^4F_{3/2}$. This transition is non-radiative. Fluorescent life time at upper laser level is comparatively more (10^{-3}s) than that of excited state. As lower laser level is virtually vacant a

population inversion is established between the two levels and the lasing action occurs where atoms decay to lower laser level $^4I_{11/2}$. Thus the strongest transition is from $^4F_{3/2}$ to $^4I_{11/2}$ and the wavelength of emitted photons is 1064nm. Non-radiative spontaneous transition takes place from the lower laser level to ground state $^4I_{9/2}$.

3.6 Scattering Centers in transparent material

Ceramics have various scattering sources and shown in Fig. 3.3, these are residual pores, secondary phase, double refraction, inclusions, and surface roughness as shown below.

Scattering loss can be calculated a

Scattering Loss α d^6 / λ^4

Where,

λ –Wavelength,

d – Scattering centre diameter

To develop a transparent ceramic, it is necessary to eliminate all these scattering centers such as porosity, pores at grain boundary, thin grain boundary, secondary phase, small grain size, high surface roughness and isotopic lattice structure.

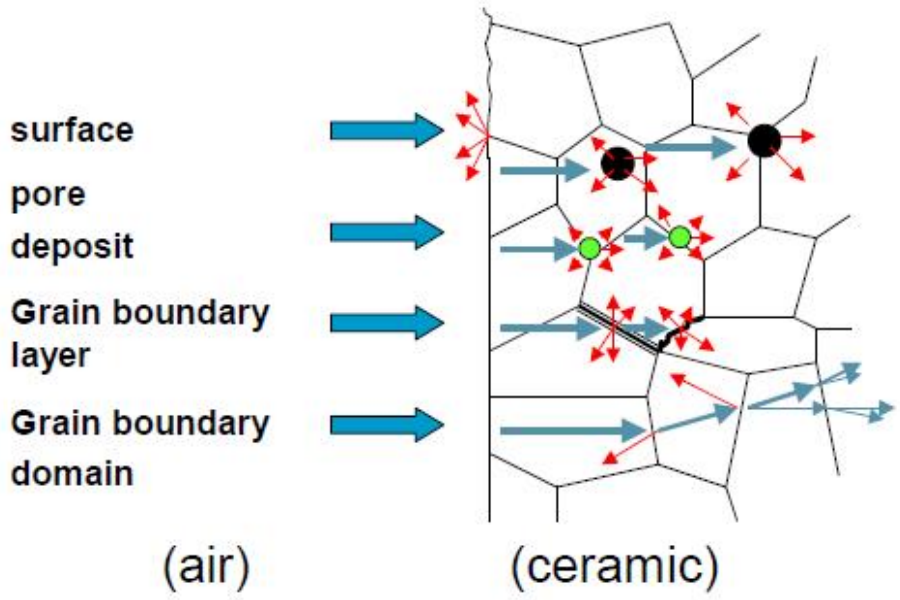

Fig. 3.3: Scattering centers in a polycrystalline ceramic

3.7 Glass

Non-crystalline or glass material are the material, where log order ordering of atoms are missing. There is a drastic difference between crystalline and glass material obtained from its melt. There is no definite temperature where liquid transforms to a solid as in crystalline materials. In fact, a glass continuously becomes more viscous with decreasing temperature. Fig. 3.4 compares specific volume versus temperature plot for crystalline and glass during solidification from its liquid. It is shown that for crystalline material, there is a discontinuous decrease in volume at the melting point, whereas it decreases continuously for glassy materials. A change in slop of the curve occurs at the glass transition temperature "T_g" and generally observed for glass.

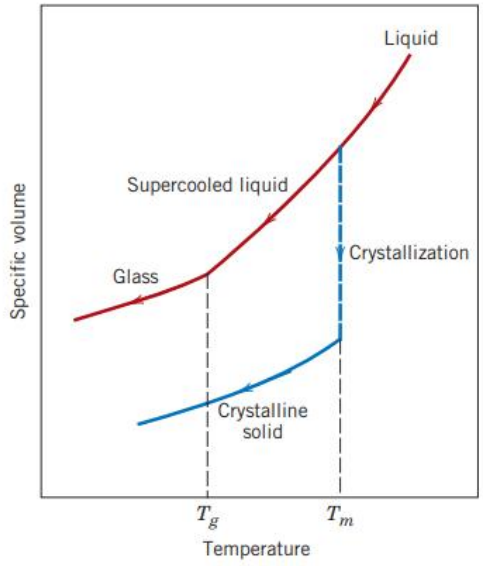

Fig. 3.4: Comparison of specific volume versus temperature behavior of glass and crystalline materials.

3.7.1 Glass forming

Glass is formed by heating the materials to a high temperature above which melting occurs and then cooled to certain temperature at very fast rate. Most commercial glasses are soda lime silicate glass. In the silica sand, Na_2O and CaO are added as soda ash (Na_2CO_3) and limestone ($CaCO_3$). In this, the SiO_2 provide a fixed random three dimensional network and Na^+ and Ca^{2+} ions act as glass modifier. In silicate glass, $(SiO_4)^{4-}$ tetrahedra joined at their corners to form three dimensional network. The Si-O-Si bond angle vary randomly throughout the structure. Alkali and Alkaline

earth ions can cause breaking of Si-O-Si network. Thus glass material do not have the plane of easy cleavage and well-defined melting points.

For most applications, optical transparency is important and it is important that the glass product be pore free and homogeneous. Homogeneity can be achieved by complete melting and mixing of the raw constituents. Porosity are produced from small gas bubbles and should be eliminated by adjusting the viscosity of the molten material.

3.8 Heat Treatment

When a molten material is cooled from its melting point at very high rate, thermal stresses, are generally introduced because of the difference in cooling rate and thermal contraction between the surface and interior regions. These thermal stresses, if not relieved, may lead to fracture. These thermal stresses can be reduced by an annealing heat treatment in which the glassware is heated to the annealing point, then slowly cooled to room temperature. The annealing temperature depends upon the composition of the glass and heating between 600-800 ^{o}C for few hours and slow cooling is sufficient for most silicate based glasses.

3.9 Fabrication of Glass-ceramic

Conversion of the glass into a glass–ceramic is accomplished by proper heat treatment. After forming the desired shape glass, the glass is heat treated as shown in fig. 3.5. After melting and forming processes, nucleation and growth of the crystalline phase particles are carried out isothermally at two different temperatures. The desired phase so produced govern the optical and mechanical properties of the end-product. Glass-ceramic demonstrate considerable advantages over glasses and ceramics. The large variety of compositions and the possibility of developing special microstructure are the main benefits. A glass-ceramic may be highly crystalline or transparent depending upon the extent of crystallization. The new crystal so formed grow in the glass phase resulting in small changes in the remaining glass compositions.

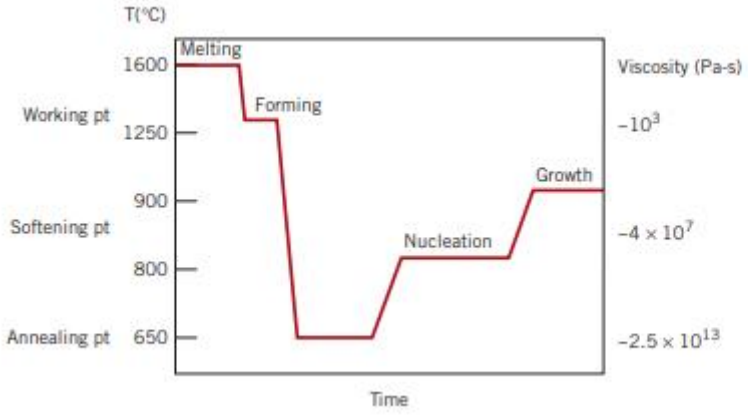

Fig. 3.5: Time versus temperature processing cycle for precipitating phase in a glass to make glass-ceramic.

3.10 Liquid to solid phase transformation:

This type of phase transformations can be divided into two categories. In one case, there is no change in the composition between liquid and solid, which is diffusion-dependent transformations. Examples includes solidification of a pure metal, recrystallization and grain growth. In another, there is some alteration in phase compositions, the final microstructure mainly consists of two or more phases.

3.11 Kinetics of phase transformation

During the phase transformations, at least one new phase is formed that has different physical and chemical characteristics. This new phase generally has a different structure from the parent phase. Generally, phase transformations do not occur instantaneously but begin by the formation of numerous small particles of the new phase (nucleation), which then increase in size (growth) until the transformation is completed. Nucleation comprises the appearance of very small particles, or nuclei, of the new phase, which are capable of growing. During the growth stage, these nuclei increase in size causing in the disappearance of the parent phase.

3.12 Nucleation

There are two types of nucleation: homogeneous and heterogeneous. Differentiation is made according to the site at which nucleating events occur. For the homogeneous

type, nuclei of the new phase form evenly throughout the parent phase. For the heterogeneous type, nuclei form preferentially at structural inhomogeneities, such as insoluble impurities, container surfaces, dislocations, grain boundaries, etc.

3.12.1 Homogeneous Nucleation

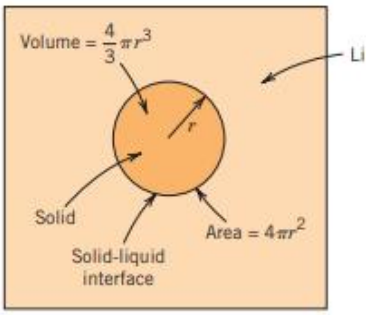

Fig. 3.6: Schematic diagram showing the nucleation of a solid sphere in a liquid.

The solidification of a pure material is considered and it is assumed that nuclei of the solid phase forms in the interior of the liquid as atoms cluster together to form a packing arrangement alike to that found in the solid phase. Let the radius of each spherical nucleus is "r".

The theory of nucleation involves a thermodynamic parameter called free energy "G". The free energy is a function of the enthalpy, H (internal energy) and the entropy, S (the randomness or disorder of the atoms) thermodynamic parameters.

In a solidification transformation, there are two contributions to the total free energy change. The first is volume free energy, ΔG_v, the free energy difference between the solid and liquid phases and its value will be negative if the temperature is below the equilibrium solidification temperature. The magnitude of its contribution to the free energy is the product of ΔG_v and the volume of the spherical nucleus ($4/3\ \pi r^3$). The second free energy contribution is due to the formation of the solid– liquid phase boundary, i.e., a surface free energy "γ", which is positive and the magnitude is the product of "γ" and the surface area of the nucleus ($4\pi r^2$). Finally, the total free energy change is equal to the sum of these two contributions;

$$\Delta G = 4/3\ \pi r^3 * \Delta G_v + 4\pi r^2 * \gamma$$

Fig. 3.7 a-b shows the plot of volume, surface, and total free energy contributions as a function of nucleus radius.

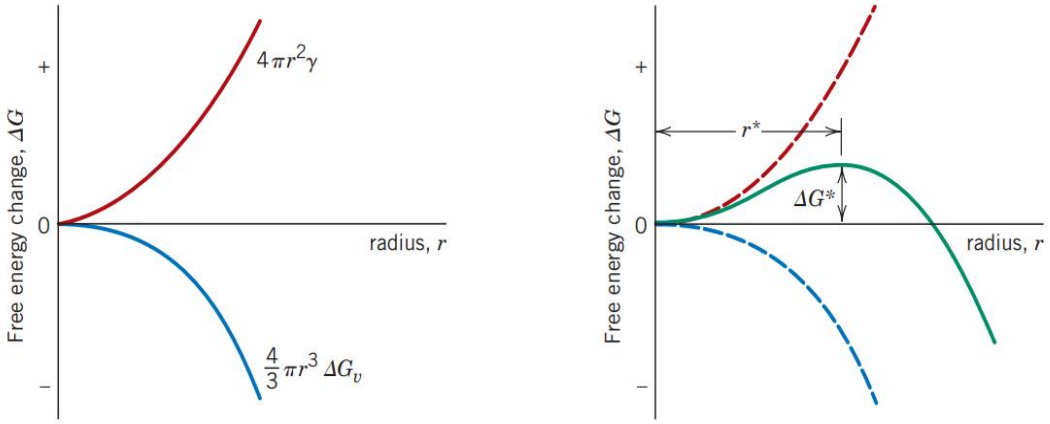

(a) (b)

Fig. 3.7: Schematic plots of (a) volume / surface free energy contribution to the (b) total free energy versus nucleus radius "r".

It may be noted that magnitude of the volume contribution to the free energy is negative and the corresponding curve decreases with the third power of r. For the curve resulting from the surface free energy, whose contribution is positive, resulting increase in the total free energy with the square of the radius. Thus, the curve associated with total free energy first increases, passes through a maximum, and finally decreases as shown in fig. 3.7 b.

In a physical sense, the free energy first increases, as a solid particle begins to form as atoms in the liquid cluster together. If the size of this cluster corresponding to the critical radius r^* , then growth will continue with a decrease in free energy. Otherwise, a cluster of radius less than the critical will shrink and re-dissolve. This subcritical particle is an embryo, whereas the particle of radius greater than r^* is termed a nucleus. The critical free energy, ΔG^*, at the critical radius corresponds to an activation free energy required for the formation of a stable nucleus. It may be considered an energy barrier to the nucleation process.

3.12.2 Heterogeneous Nucleation

Nucleation occurring at surfaces and interfaces than at other sites is termed heterogeneous. To understand this phenomenon, consider the nucleation, on a flat

surface, of a solid particle from a liquid phase as shown in fig. 3.8. It is assumed that both the liquid and solid phases "wet" the flat surface. There are three interfacial energies, represented as vectors in fig. 3.8, that exist at two-phase boundaries—γ_{SL}, γ_{SI}, and γ_{IL} along with the wetting angle θ (the angle between the γ_{SI} and γ_{SL} vectors. Considering a surface tension force balance in the plane of the flat surface, following equation can be written:

$$\gamma_{IL} = \gamma_{SI} + \gamma_S L \cos\theta$$

Using above equation, the critical free energy is derived to

$$\Delta G^*_{het} = \Delta G^*_{hom} \times S(\theta)$$

Where S(θ) is a function of θ (i.e., shape of the nucleus) and for θ angles of 30° and 90°, values of S(θ) are approximately 0.01 and 0.5, respectively.

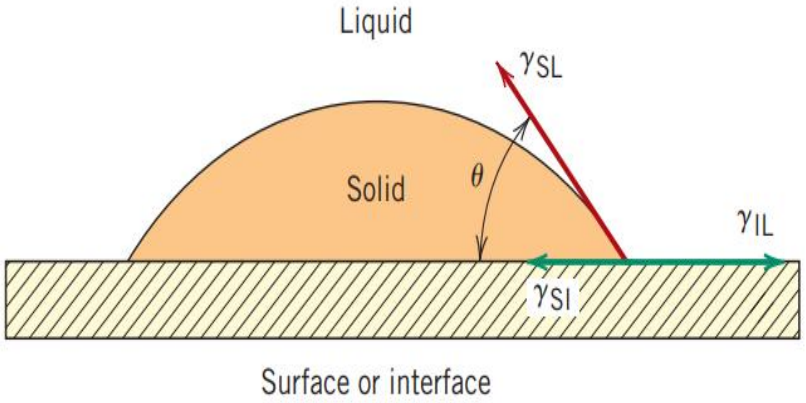

Fig. 3.8: Schematic depicting heterogeneous nucleation of a solid from a liquid.

Fig. 3.9 shows a schematic graph of ΔG versus nucleus radius plots for both types of nucleation. The difference in the magnitudes of ΔG^*_{het} and ΔG^*_{hom}, is clearly shown. The lower ΔG^* for heterogeneous means that a smaller barrier energy needed to overcome during the nucleation process compared to that of homogeneous nucleation. Therefore, heterogeneous nucleation occurs more readily.

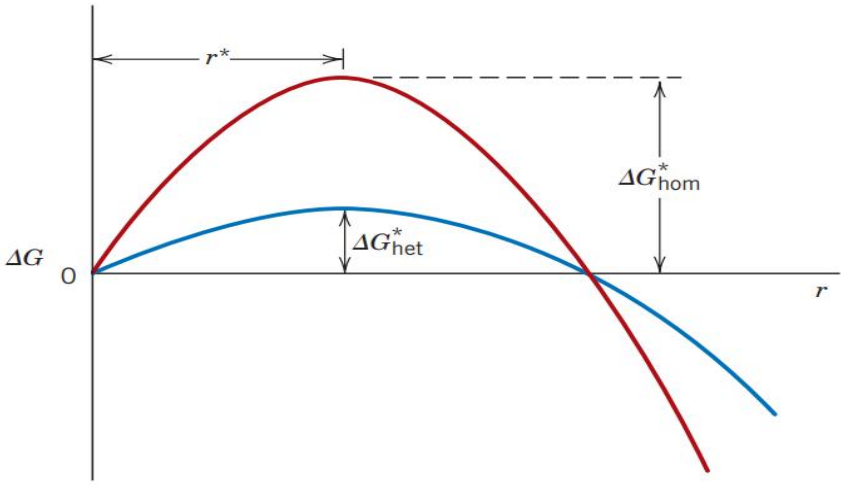

Fig. 3.9: Comparison of free energy versus nucleus radius plot for homogeneous and heterogeneous nucleation.

3.13 Growth

The growth step begins once an embryo has exceeded the critical size and becomes a stable nucleus. This nucleation will continue to grow in size but this growth process will cease in any region where particles of the new phase meet indicating the completion of phase transformation process.

Particle growth involves long range atomic diffusion, which comprises number of steps like, diffusion through the parent phase, across a phase boundary, and then into the nucleus. Consequently, the growth rate is dependent upon the rate of diffusion. Temperature dependent of the growth rate is equivalent as:

Growth rate = constant x exp (- E_a / KT)

Where E_a is the activation energy and K is the Boltzmann constant.

Thus, the size of the product phase particles will depend on transformation temperature. If the transformation temperature is occurring at temperatures near to melting point (T_m), which corresponds to low nucleation and high growth rates, which means few nuclei form that grow rapidly. Thus, the resulting microstructure will consist of few and relatively large phase particles (e.g., coarse grains). Conversely, for transformations at lower temperatures (well below T_m), nucleation rates are high and growth rates low, which results in many small particles (e.g., fine grains).

3.14 Phase Diagram

In the development of glass-ceramics, the most important factors are composition and thermal treatment given to the glass to get the desired microstructure. The parent chemical composition controls the ability to form a glass and determines whether internal or surface nucleation can be achieved. Nucleation agents are generally added in the glass composition if internal nucleation is sought.

The most important glass-forming systems are based on silicate composition. Certain other oxides are added to control the desired phase in the final product. In alumino-silicate glass, the three dimensional network is formed by tetrahedral Si and Al ions. All tetrahedral ions are bonded through oxygen to another tetrahedral ion. These alumino-silicates are also known as stuffed derivatives of silica because Si^{4+} network is replaced by Al^{3+} accompanied by a filling of interstitial vacancies by larger cations to maintain charge neutrality.

In this study, yttrium alumino-silicate glass ternary system is selected because of the presence of a glassy zone in the phase diagram, as shown in fig. 3.10. These glasses have high glass-transition temperature, optical and mechanical property and can be used as a host material in laser application.

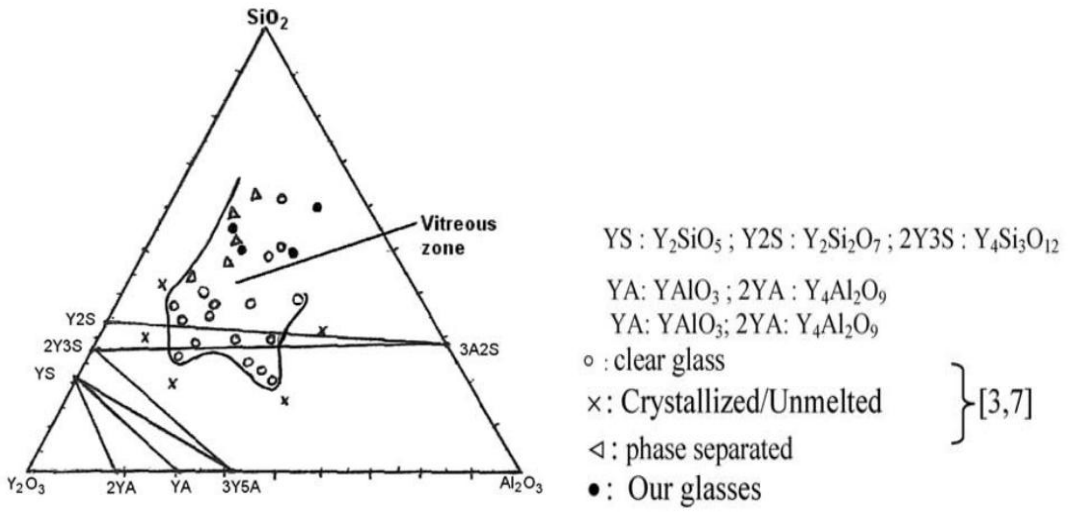

Fig. 3.10: Ternary diagram for Y_2O_3-Al_2O_3-SiO_2 system

Chapter 4

Characterization Techniques

4.1 X-ray Diffraction (XRD)

X-ray Diffraction (XRD) is a fundamental and widely employed analytical technique for investigating the structural properties of crystalline materials. It offers non-destructive characterization and is particularly effective in identifying phase composition, determining crystal structures, and measuring strain, crystallite size, and texture. Owing to its precision and versatility, XRD has become an essential tool in the fields of materials science, solid-state chemistry, mineralogy, and metallurgy.

4.1.1 Principle

XRD operates on the principle of constructive interference of monochromatic X-rays and the periodic atomic planes in a crystalline material. When an X-ray beam is incident on a crystal lattice, it is diffracted by the electron clouds surrounding the atoms as shown in Fig. 4.1. If the path difference between reflected rays from successive atomic planes satisfies the condition for constructive interference, a detectable diffracted beam is produced. This phenomenon is mathematically described by Bragg's Law:

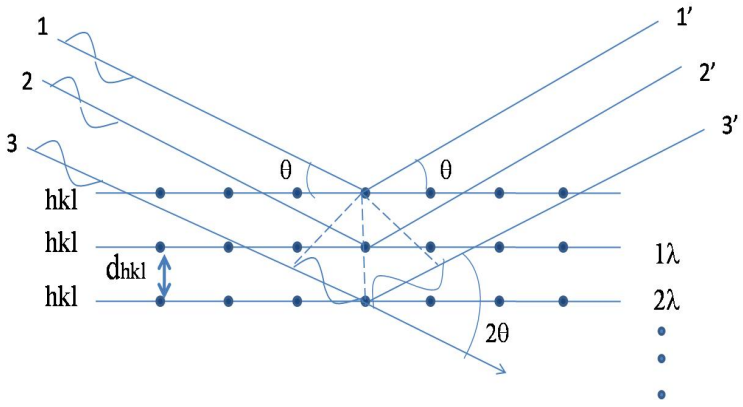

Fig. 4.1: X-Ray diffraction using Bragg's law

$$n\lambda = 2d\sin\theta$$

Where:

n is the order of diffraction,

λ is the X-ray wavelength,

d is the interplanar spacing,

θ is the angle of incidence/reflection.

By varying the angle $\boldsymbol{\theta}$, and measuring the intensity of reflected X-rays, it is possible to derive a diffraction pattern unique to the crystal structure of the sample.

4.1.2 Experimental Setup

An XRD system typically comprises the following key components:

X-ray Source: Usually a copper anode producing Cu Kα radiation (λ = 1.5406 Å).

Sample Holder: Designed to position the specimen accurately in the path of the X-ray beam.

Goniometer: Facilitates controlled rotation of the sample and detector.

Detector: Records the intensity of diffracted X-rays as a function of the angle (2θ).

The most common configuration is the θ–2θ geometry, in which the X-ray tube remains stationary while the sample rotates at an angle $\boldsymbol{\theta}$, and the detector rotates at $\boldsymbol{2\theta}$.

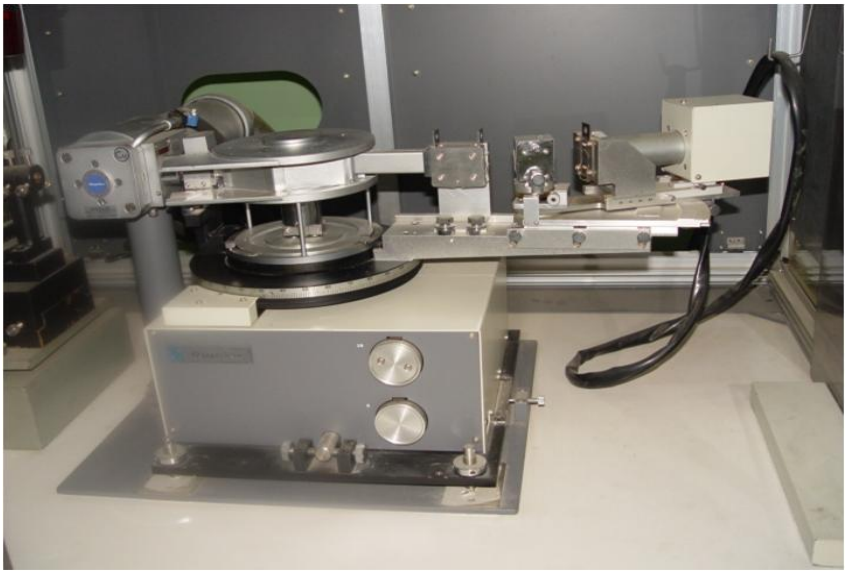

Fig. 4.2: X-Ray Diffractometer

4.1.3 Diffraction Patterns and Analysis

The resulting data from an XRD scan is presented as a diffraction pattern, which plots the intensity of reflected X-rays against the diffraction angle 2θ. Each peak in the pattern corresponds to diffraction from a specific set of lattice planes, defined by Miller indices (hkl). The position, shape, and intensity of these peaks provide critical information:

Peak Positions: Reveal the unit cell dimensions and phase identification.

Peak Intensities: Indicate atomic positions and symmetry.

Peak Broadening: Can be used to estimate crystallite size and microstrain using the Scherrer equation:

$$\boldsymbol{D = \frac{K\lambda}{\beta \cos\theta}}$$

Where:

$\boldsymbol{D}$ is the average crystallite size,

$\boldsymbol{K}$ is the shape factor (typically 0.9),

$\boldsymbol{\beta}$ is the full width at half maximum (FWHM) in radians,

$\boldsymbol{\theta}$ is the Bragg angle.

X-ray Diffraction remains a cornerstone technique in structural analysis, offering a unique and indispensable view into the atomic arrangement of materials. Its precision, versatility, and adaptability make it an essential tool in modern materials research, especially in the synthesis and characterization of novel compounds

4.2 Determination of Thermal Expansion Coefficient Using Dilatometry

The coefficient of thermal expansion (CTE) is a critical physical property that quantifies the tendency of a material to change its dimensions with temperature. This behavior is particularly significant in applications where materials undergo cyclic thermal loading or are used in multi-material assemblies. Thermal mismatch between components can result in stress buildup, cracking, or mechanical failure. The dilatometer is a widely used instrument for measuring the thermal expansion of solids with high precision.

4.2.1 Principle

Dilatometry measures the dimensional change of a specimen as a function of temperature. The coefficient of linear thermal expansion (α) is given by:

$$\boldsymbol{\alpha = \frac{1}{L_0} \cdot \frac{dL}{dT}}$$

Where:

$\boldsymbol{\alpha}$: Linear thermal expansion coefficient ($°C^{-1}$ or K^{-1})

$\boldsymbol{L_0}$: Original length of the sample (mm)

$\boldsymbol{dL}$: Incremental change in length (mm)

$\boldsymbol{dT}$: Incremental change in temperature (K or °C)

In practice, dilatometry provides a continuous recording of the specimen's length change as it is heated or cooled, from which α can be calculated over a specified temperature interval using:

$$\boldsymbol{\alpha = \frac{\Delta L}{L_0 \cdot \Delta T}}$$

This data is especially useful when materials exhibit nonlinear expansion characteristics due to phase transitions or changes in crystal structure.

4.2.2 Data Interpretation

The output from the dilatometer is typically a curve of change in length (ΔL) versus temperature (T). From this, the average or instantaneous α can be determined for different temperature intervals. For materials with non-linear behavior (e.g., polymers or phase-transforming alloys), the curve may show inflection points corresponding to transitions such as the glass transition temperature (Tg) or sintering onset.

The test provides valuable insight into:

Thermal strain

Phase transformations

Structural relaxation

Densification and sintering kinetics (for ceramics and powders)

The dilatometer test is a vital technique for evaluating the thermal expansion behavior of materials. It provides accurate, high-resolution data on dimensional changes over a wide temperature range. The coefficient of thermal expansion, derived from this test, is a fundamental input for thermal stress modeling, failure prediction, and design of thermally robust systems. As materials engineering progresses toward multi-functional and multi-phase systems, reliable thermal expansion data becomes even more critical.

4.3 Vickers Hardness Test

Hardness is a mechanical property that defines a material's resistance to localized plastic deformation, typically by indentation. Among various methods used to quantify hardness, the Vickers Hardness Test (VHT) is one of the most widely adopted due to its accuracy, versatility, and applicability to a wide range of materials, including metals, ceramics, and thin films. The Vickers test employs a geometrically defined indenter and offers the advantage of a continuous hardness scale, making it ideal for both micro and macro hardness evaluations.

4.3.1 Principle

The Vickers hardness test uses a square-based diamond pyramid indenter with an angle of 136° between opposite faces. When a known load is applied, the indenter penetrates the surface of the material, creating a square-shaped indentation. The Vickers hardness number (VHN or HV) is calculated based on the applied force and the surface area of the indentation, using the formula:

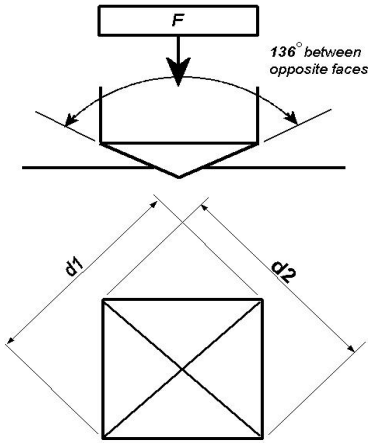

Fig. 4.3: Vickers Hardness test Diamond indenter

$$HV = \frac{1.8544 \cdot F}{d^2}$$

Where:

HV: Vickers hardness number

F: Applied load (in kgf)

d: Average length of the two diagonals of the indentation (in mm)

This relationship allows the test to provide a consistent measure of hardness regardless of the test load, assuming a homogeneous material response.

4.3.2 Experimental Setup

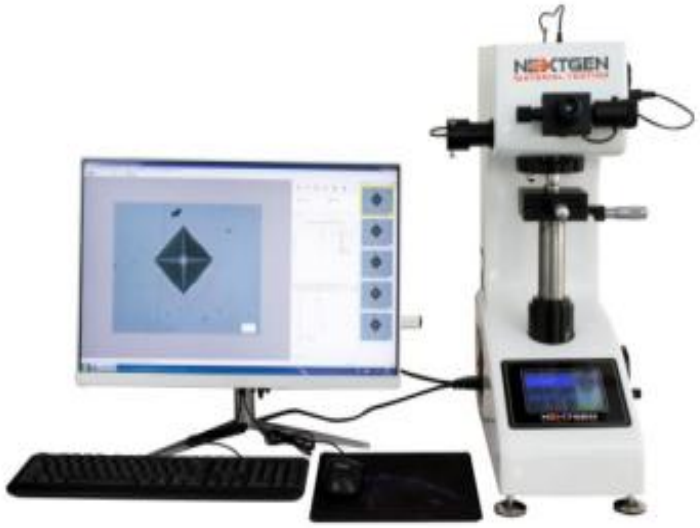

Fig. 4.3: Vickers Hadness test Setup

- **Diamond pyramid indenter**
- **Loading mechanism** (typically 10 g to 100 kg depending on application)
- **Optical microscope** with micrometer eyepiece for diagonal measurement
- **Stage and focusing mechanism** for accurate placement and imaging

In research, Vickers hardness data often complements microstructural studies, phase analysis, and fatigue testing, providing a link between material composition and mechanical behavior.

The Vickers hardness test remains a cornerstone in mechanical property characterization due to its adaptability, accuracy, and ease of interpretation. Its ability to assess materials at both micro and macro scales makes it invaluable for research and industrial applications alike. When properly conducted, the VHT provides critical insight into material strength, deformation behavior, and wear resistance—qualities that are vital in the development and evaluation of modern engineering materials.

4.4 Scanning Electron Microscopy (SEM)

Scanning Electron Microscopy (SEM) is a powerful imaging technique that provides high-resolution images of the surface topography and composition of materials. SEM is a vital tool in fields such as materials science, biology, nanotechnology, and forensic analysis. By scanning a focused electron beam across a specimen, SEM allows for the detailed study of surface features at a microscopic to nanoscopic scale.
The SEM's capability to deliver high magnification and depth of field has revolutionized various fields, offering insight into the morphology, structure, and material properties of a broad range of specimens.

4.4.1 Principle of SEM

SEM operates by directing a finely focused beam of electrons onto a specimen's surface. As the electron beam interacts with the atoms on the surface, several signals are emitted, including secondary electrons, backscattered electrons, and X-rays. These signals are then detected by various detectors, providing valuable information about the specimen.

1. **Electron Source:** The electron beam is generated by an electron gun, typically a tungsten filament or a field emission gun (FEG).
2. **Beam Scanning:** The beam is focused and scanned across the specimen in a raster pattern.
3. **Signal Detection:**
    - **Secondary Electrons (SE):** These low-energy electrons are emitted from the outer surface layers and are used to generate high-resolution topographical images.
    - **Backscattered Electrons (BSE):** These electrons are reflected from the specimen and provide contrast based on atomic number (Z contrast), useful for imaging material composition.
    - **X-rays:** Characteristic X-rays can be generated by electron-beam interactions, and energy dispersive X-ray spectroscopy (EDS) can be used to determine the elemental composition of the specimen.

4. **Image Formation:** The detected signals are converted into an image on a monitor. The intensity of the detected signal correlates with the surface characteristics of the sample, such as texture, shape, and material composition.

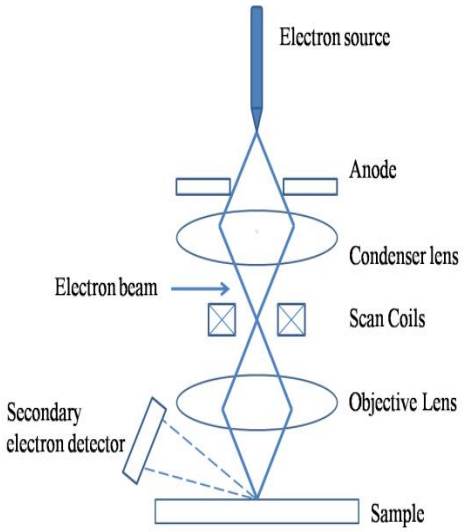

Fig. 4.4 : Schematic diagram of Scanning Electron Microscope

4.4.2 Test Procedure

The procedure for SEM imaging typically involves the following steps:

1. **Specimen Preparation:** Specimens must be conductive or coated with a conductive layer, such as gold or carbon, to prevent charging under the electron beam. Biological samples often require additional treatments, such as dehydration and sputter coating.
2. **Mounting:** The specimen is mounted on a sample stage, which is typically placed under a vacuum in the SEM chamber to allow electron flow.
3. **Scanning and Imaging:** The electron beam is directed onto the specimen, and the emitted signals are captured and used to create images at varying magnifications.
4. **Data Analysis:** In addition to imaging, the SEM can provide additional analytical data through energy-dispersive X-ray spectroscopy (EDS), electron backscatter diffraction (EBSD), or other techniques.

Fig. 4.5 : Carl Zeiss Sigma FESEM instrument

Scanning Electron Microscopy is an indispensable tool in modern scientific and industrial research. Its ability to provide high-resolution imaging and detailed elemental analysis makes it invaluable in a variety of fields. Despite challenges related to sample preparation and the high cost of equipment, SEM continues to be a powerful technique for examining the intricate structures of materials and biological samples. As SEM technology evolves, it will continue to play a critical role in advancing our understanding of the micro and nanoscale world.

4.5 Archimedes' Density Measurement

The Archimedes' density measurement is one of the oldest and most widely used methods for determining the density of an object, particularly when the object is irregular in shape. This technique, attributed to the ancient Greek mathematician and physicist Archimedes, relies on the principle of buoyancy, which states that a body submerged in a fluid experiences an upward force equal to the weight of the fluid displaced by the body. The Archimedes' principle can be applied to measure the density of an object by calculating the volume of displaced fluid when the object is immersed in a liquid.

Density, defined as the mass per unit volume, is a critical property in various scientific and industrial applications. The Archimedes' method is particularly useful

for measuring the density of solid objects with irregular shapes that cannot be easily measured using traditional geometric formulas.

4.5.1 Principle of Archimedes' Density Measurement

The principle behind Archimedes' density measurement is based on Archimedes' Principle, which states that:

> "A body immersed in a fluid experiences a buoyant force equal to the weight of the fluid it displaces."

To determine the density of an object using this principle, two key parameters are required: mass and volume. The density $\boldsymbol{\rho}$ of an object can be calculated using the formula:

$$\boldsymbol{\rho} = \frac{\boldsymbol{m}}{\boldsymbol{V}}$$

Where:

- $\boldsymbol{\rho}$ is the density of the object,
- $\boldsymbol{m}$ is the mass of the object,
- $\boldsymbol{V}$ is the volume of the object.

While the mass of an object can be directly measured using a balance, the volume is determined by the displacement of a fluid when the object is submerged.
"Weight of solid in air - weight of solid when immersed in liquid = loss in weight of solid"

"Loss in weight of solid = weight of the liquid displaced"

Density of any sample can be calculated by using formula given below:

$$\frac{\text{Density of object}}{\text{Density of fluid}} = \frac{\text{Weight of object}}{\text{Weight of displaced fluid}}$$

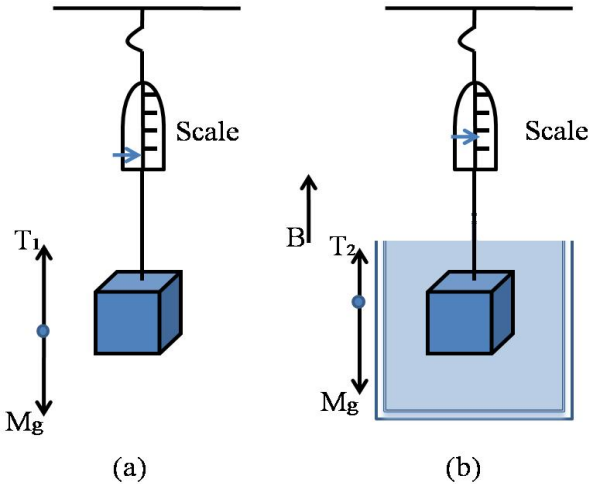

Fig. 4.6: Archimedess experimental set up

Archimedes' density measurement remains a simple, effective, and reliable method for determining the density of solid objects, particularly those with irregular shapes. Despite some limitations, such as the need for accurate fluid displacement and temperature calibration, the method is widely used in various industries, including material science, geology, engineering, and forensic investigations. Its non-destructive nature, low cost, and broad applicability make it an indispensable tool for density measurement in both academic research and industrial applications.

4.6 Diffuse Reflectance Spectroscopy (DRS)

Diffuse Reflectance Spectroscopy (DRS) is a powerful analytical technique used to investigate the optical properties of solid and powdered materials. Unlike conventional transmission spectroscopy, DRS is ideal for opaque or highly scattering samples, making it especially valuable in materials science, catalysis, soil science, and pharmaceuticals. The method is based on the measurement of diffusely reflected light from a sample when it is irradiated by a light source across a defined spectral range. The resulting reflectance data can be correlated with the material's electronic transitions, molecular vibrations, or compositional features, depending on the spectral region used (UV-Vis, NIR, or IR).

4.6.1 Principle of DRS

When light interacts with a rough or powdered solid, it undergoes multiple scattering events within the material. A portion of the light is absorbed, and the rest emerges

from the surface as diffusely reflected light. This diffusely reflected light carries spectral information analogous to that of absorbance in transmission measurements.
To interpret DRS data, the Kubelka-Munk function is commonly used. It relates the reflectance of a sample to its absorption (K) and scattering (S) coefficients:

$$\boldsymbol{F(R) = \frac{(1-R)^2}{2R} = \frac{K}{S}}$$

Where:

- $\boldsymbol{F(R)}$: Kubelka-Munk function
- $\boldsymbol{R}$: Reflectance of the sample (relative to a non-absorbing standard)
- $\boldsymbol{K}$: Absorption coefficient
- $\boldsymbol{S}$: Scattering coefficient

This transformation allows the reflectance spectrum to be interpreted similarly to absorbance spectra, aiding in qualitative and semi-quantitative analysis.

4.6.2 Instrumentation and Methodology

A typical DRS setup includes the following components:

Light Source: A broadband lamp (e.g., deuterium for UV, tungsten-halogen for visible-NIR) provides incident light.

Integrating Sphere: A specialized optical component that collects diffusely reflected light from all angles.

Sample Holder: Designed to accommodate powders, pellets, or irregular solids, ensuring uniform exposure.

Detector: Sensitive photodiodes or CCD detectors record the intensity of reflected light.

Reference Standard: A highly reflective material (e.g., Spectralon or $BaSO_4$) is used for baseline calibration.

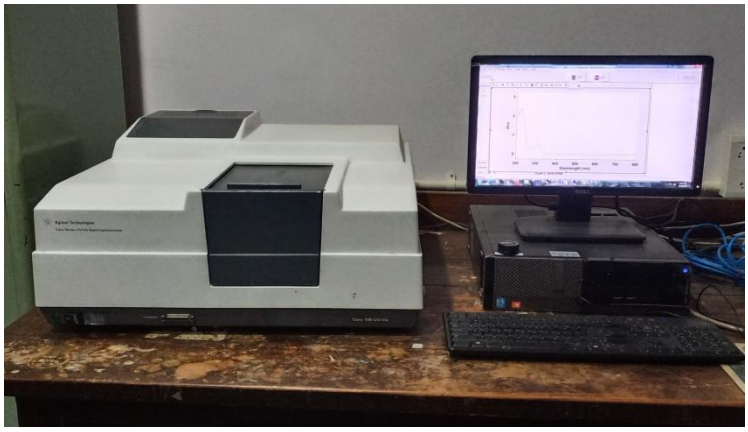

Fig. 4.7: UV-VIS spectrophotometer

The measurement involves directing light onto the sample and comparing the reflected intensity to that from a reference material. The resulting spectrum is processed to calculate reflectance or Kubelka-Munk units, revealing information about the sample's electronic and molecular characteristics.

Diffuse Reflectance Spectroscopy is a vital technique in modern analytical science, offering a non-invasive approach to studying opaque and scattering materials. Through careful calibration and analysis, DRS provides insights into band structure, composition, and surface properties that are invaluable in research and industrial quality control. Its broad applicability and ease of use continue to make it a preferred method for solid-state characterization in diverse scientific disciplines.

4.7 Fourier Transform Infrared Spectroscopy (FTIR)

Fourier Transform Infrared Spectroscopy (FTIR) is a powerful and versatile analytical technique used to obtain the infrared spectrum of absorption or emission of materials. By studying the interaction between infrared radiation and matter, FTIR allows researchers to identify molecular structures, chemical bonds, and functional groups within a sample. FTIR is widely used in fields such as chemistry, biology, material science, pharmaceuticals, and environmental studies due to its non-destructive nature and rapid, high-resolution analysis.

FTIR is an improvement over traditional infrared spectroscopy, as it utilizes a mathematical technique called the Fourier Transform to process raw data. This method offers enhanced sensitivity, faster analysis, and better resolution compared to conventional dispersive infrared spectrometers.

4.7.1 Principle of FTIR

FTIR operates on the principle that molecules absorb infrared radiation at specific frequencies that correspond to the vibrational modes of the chemical bonds within the molecule. When infrared light is passed through or reflected from a sample, different functional groups absorb radiation at characteristic frequencies, resulting in a spectrum that can be used to identify the material's composition.

The key feature of FTIR is the Fourier Transform process. Unlike traditional infrared spectroscopy, which scans through individual wavelengths, FTIR collects data across a wide range of frequencies simultaneously. This approach creates an interferogram—a time-domain signal—which is then converted into a frequency-domain spectrum using a Fourier Transform. This method significantly improves the speed and sensitivity of spectral acquisition.

The general relationship between the frequency of light absorbed and the vibrational modes of molecules can be summarized by the equation:

$$\boldsymbol{v = \frac{1}{2\pi}\sqrt{\frac{k}{m}}}$$

Where:

- $\boldsymbol{v}$ is the vibrational frequency of the bond,
- $\boldsymbol{k}$ is the bond force constant,
- $\boldsymbol{m}$ is the reduced mass of the atoms involved.

Thus, each functional group or bond has a characteristic vibrational frequency that appears as a peak in the FTIR spectrum.

4.7.2 Instrumentation

1. IR Source: Emits broad-spectrum IR radiation (4000–400 cm^{-1}).
2. Interferometer: Splits and recombines the IR beam to create an interferogram.
3. Sample Holder: Accommodates solids (KBr pellets), liquids (sandwiched between IR-transparent windows), or gases (gas cells).
4. Detector: Converts transmitted light into electrical signals (DTGS or MCT types).
5. Computer & Processor: Performs the Fourier Transform and displays the IR spectrum.

The sample is prepared based on its physical form and exposed to infrared radiation. The interferogram collected by the detector is transformed into an absorption spectrum, where each peak represents a specific vibrational mode. Comparison with reference databases allows identification of chemical structures.

Fourier Transform Infrared Spectroscopy (FTIR) is a powerful and versatile analytical technique used to identify molecular structures and chemical compositions with high sensitivity and resolution. It is indispensable in fields ranging from pharmaceuticals to material science, environmental monitoring, and forensic analysis. Despite some limitations such as interference from water and complex spectra, FTIR remains a cornerstone technique in analytical laboratories due to its speed, non-destructive nature, and comprehensive analytical capabilities.

4.8 Absorption Spectroscopy

Absorption spectroscopy is a widely used analytical technique that measures the absorption of light by a sample across different wavelengths of the electromagnetic spectrum. This technique is employed to analyze the composition of substances. By measuring the amount of light absorbed by a sample, absorption spectroscopy can provide detailed information about the sample's molecular structure, concentration, and the presence of specific compounds.

The fundamental principle behind absorption spectroscopy is that when light passes through a sample, certain wavelengths are absorbed by the material depending on its molecular composition. The amount of absorption at each wavelength is related to the energy transitions of the molecules in the sample, and by analyzing these absorptions, we can gain insights into the sample’s properties.

4.8.1 Principle

The technique is governed by Beer-Lambert’s Law, which relates absorbance (A) to concentration (c), path length (l), and the molar absorption coefficient (ε):

$$\boldsymbol{A = \varepsilon c l}$$

Absorbance is logarithmically related to transmittance (T), the fraction of light passing through the sample:

$$\boldsymbol{A = -\log(T)}$$

When a sample is irradiated with light, specific wavelengths are absorbed depending on the molecular structure. Plotting absorbance versus wavelength yields an

absorption spectrum, with peaks corresponding to energy transitions within the sample.

4.8.2 Instrumentation

A basic absorption spectrophotometer includes:

1. Light Source – Provides continuous radiation (e.g., tungsten for visible, deuterium for UV).
2. Monochromator/Filters – Isolate specific wavelengths.
3. Sample Holder – Holds the sample (liquid cuvettes are typically glass or quartz).
4. Detector – Measures transmitted light and converts it to an electrical signal (e.g., photodiode, PMT, CCD).
5. Readout System – Displays the absorbance spectrum using a computer interface.

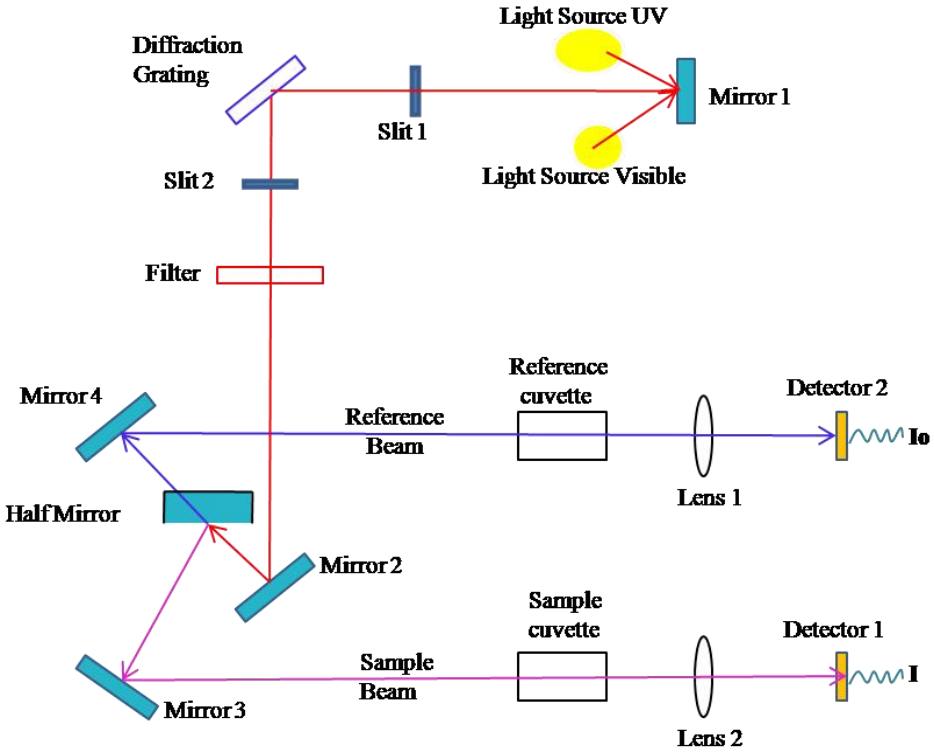

Fig. 4.9: Optical system diagram of spectrophotometer

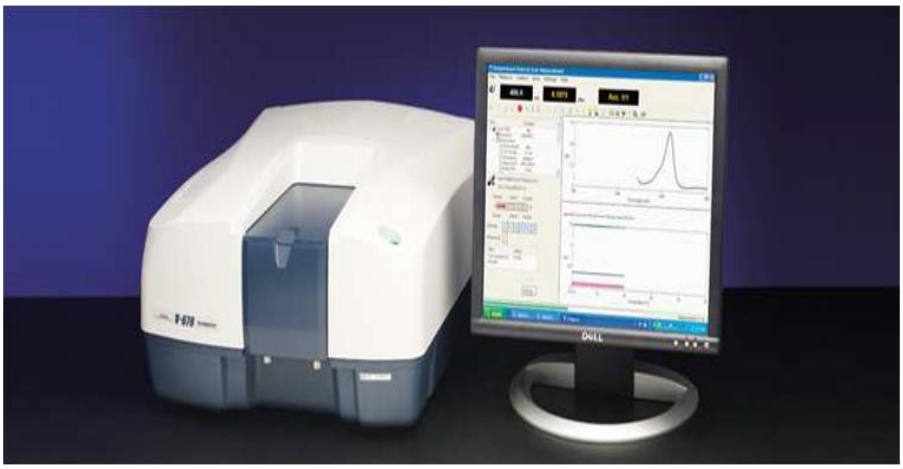

Fig. 4.8: UV-VIS-NIR Spectrophotometer (JASCO V-670)

Absorption spectroscopy is a versatile and widely used technique in analytical chemistry and various scientific disciplines. It provides valuable information about the molecular composition, concentration, and properties of a sample by measuring its absorption of light at different wavelengths. Despite some limitations, such as interference from other compounds and the need for careful sample preparation, absorption spectroscopy remains a cornerstone method for both qualitative and quantitative analysis in laboratories worldwide.

4.9 Photoluminescence Spectroscopy

Photoluminescence (PL) spectroscopy is a widely used technique for characterizing the electronic and optical properties of materials, particularly semiconductors, organic compounds, and nanomaterials. This technique measures the light emitted from a material after it has absorbed photons, providing valuable insights into the material's energy levels, band gaps, and defect structures. PL spectroscopy is non-destructive, highly sensitive, and capable of providing both qualitative and quantitative data, making it essential in research and development across various fields, including materials science, nanotechnology, and biophotonics.

4.9.1 Principle of Photoluminescence Spectroscopy (PL)

Photoluminescence occurs when a material emits light after absorbing photons. Upon excitation—usually by a laser—electrons are promoted to higher energy states. These excited electrons then relax and recombine with holes, emitting light at a lower energy than the absorbed photons. The emitted light reflects the material's band gap or

energy-level differences, revealing critical information about its electronic structure, defects, and impurities. The emission spectrum, plotted as intensity versus wavelength or energy, highlights features like peaks or broad bands tied to specific electronic transitions.

4.9.2 Instrumentation

A typical PL setup includes:

1. Light Source – Often a laser (e.g., UV or visible) to excite the sample.
2. Sample Holder – May be temperature-controlled to study temperature-dependent properties.
3. Monochromator – Selects excitation and emission wavelengths.
4. Optical Elements – Lenses, mirrors, and filters focus and direct light.
5. Detector – PMTs or CCDs convert emitted light into electrical signals.
6. Computer & Software – For controlling instruments, recording spectra, and analyzing data.

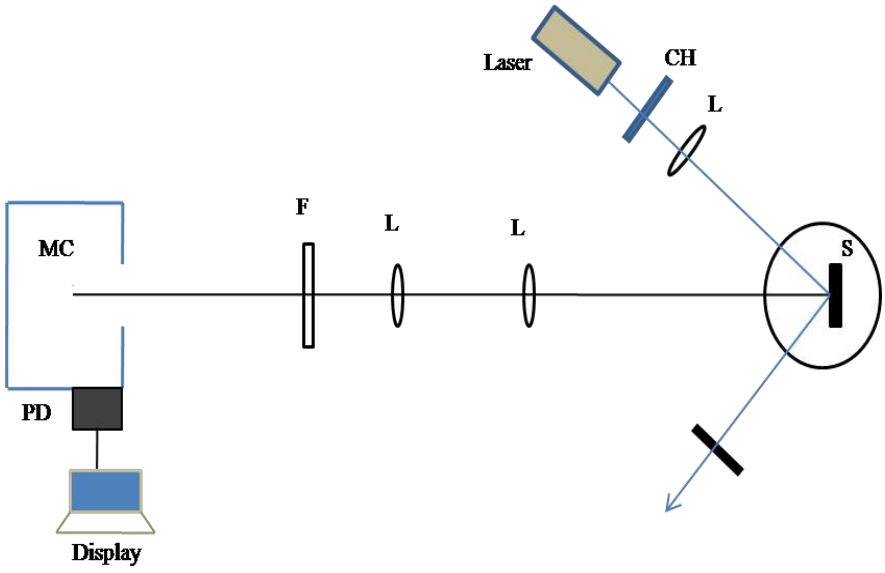

Fig. 4.10: Schematic of experimental setup for PL measurements

Fig. 11: Edinburghs FLS 920 fluorescence spectrometer

Photoluminescence spectroscopy is a powerful tool for studying the optical and electronic properties of materials. It provides valuable insights into the behavior of semiconductors, nanomaterials, organic compounds, and biological systems. While it has some limitations, such as sample sensitivity and the need for careful data interpretation, its high sensitivity, non-destructive nature, and wide range of applications make it an essential technique in both research and industry.

Chapter 5

Experimental

5.1 Experimental

The starting chemical reagents, Nd_2O_3 (99.9%, Alfa Aesar), Y_2O_3 (99.9%, Alfa Aesar), Al_2O_3 (99.8%, LOBA Chemie), SiO_2 (99.9%, LOBA Chemie), Li_2O (99.9%, Sigma-Aldrich), TiO_2 (99.9%, Sigma-Aldrich), ZrO_2 (99.9%, S.d. Fine Chem Ltd.) were used to synthesize the glass. The desired glass composition has the following chemical constitutes in weight%.

Table 5.1 Glass composition (in wt%)

Constituents	Y_2O_3	Al_2O_3	SiO_2	Li_2O	Nd_2O_3	TiO_2	ZrO_2
Weight %	26	30	37	3.0	1.5	1.0	1.5

The powder was mixed using a ball-mill for 4 hours and then melted in a platinum crucible at 1500 ^oC for 2 h and finally poured into a carbon mold kept on a hot plate around ~ 200 ^oC. The glass bar so obtained was then slowly heated to 600 ^oC at a rate of 2 ^oC/minute and kept it for 12 hours before cooling (2 ^oC/min) it slowly to room temperature to remove thermal stresses. As fabricated glass rod (10mm x 120mm) is shown in fig. 5.1(a). The annealed rod was cut into small samples as shown in fig. 5.1(b).

(a)

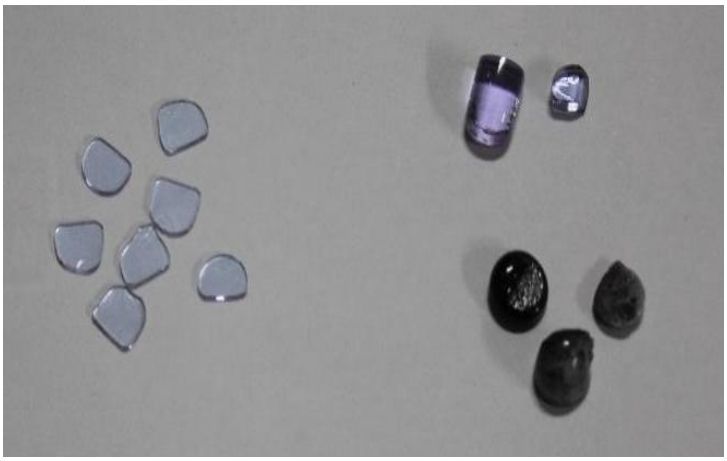

(b)

Fig. 5.1: Images of the as-prepared rod (a) after thermal annealing. Section of a rod is also shown (b) for thermal treatment.

The rod was cut into small thin (~ 2-3mm) pieces. The small thin glass was subjected to crystallization under the heat-treatment profile shown in Fig. 5.2. These heat treated Nd-glass section was used for the measurement of thermal expansion, refractive index, heat treatment at various temperature, hardness and microstructure.

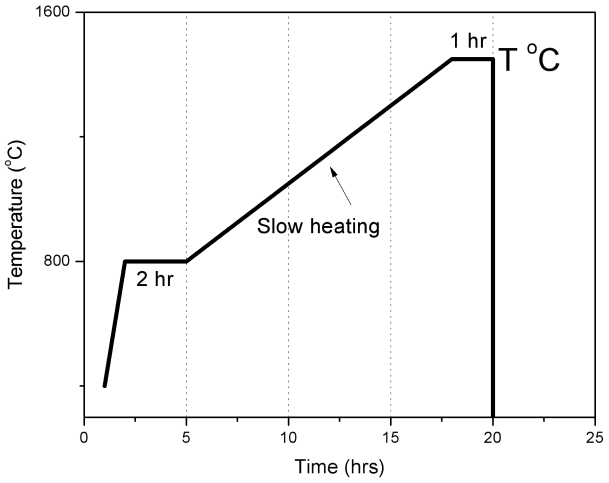

Fig. 5.2: Heat-treatment profile for crystallization (T = 900, 950, 1000, 1050, 1100, 1150, 1200, 1250, 1300, 1350, 1400, 1450, 1500 °C-0h).

The cut sample was given a heat treatment (900 to 1450 °C) for 1 to 6-hour dwell in air. Fig. 5.3: shows the scan images of the sample after heat treatment.

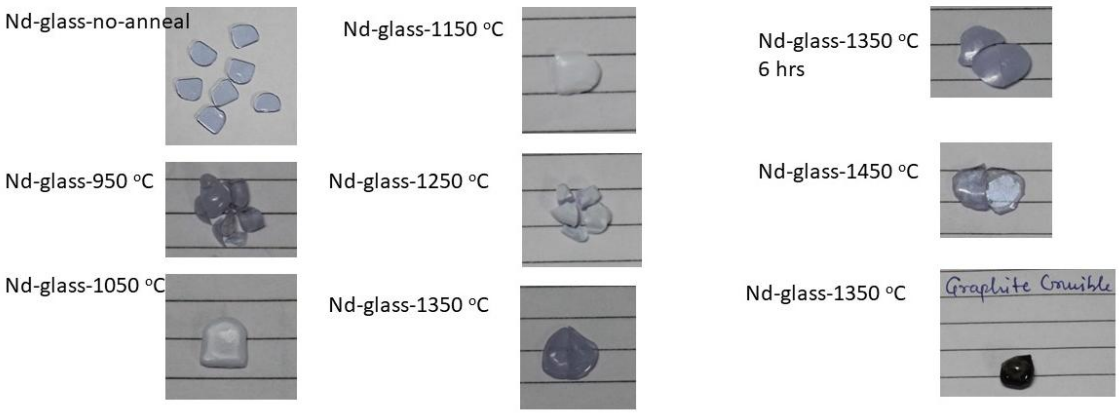

Fig. 5.3: Scan images of heat treated Nd-glass sample. Temperature next to the image shows the sample heated to the temperature in air for 1 hour.

To determine if the precipitation is occurring in the bulk or at the surface or both, the thermally treated sample was cut from the middle. Fig. 5.4 shows the scan images of the sample after heat treatment. It is clear from these scan images that surface precipitation starts first around 950 °C. No precipitation in the bulk is observed. Precipitation at the surface and also in the bulk is shown in the Nd-glass sample heat treated at 1050 °C. It is clear from these scan images that surface precipitation occurs first followed by another phase precipitation in the bulk. The PD-1050 °C sample was opaque stating that the size of the precipitated phase may by micron or more.

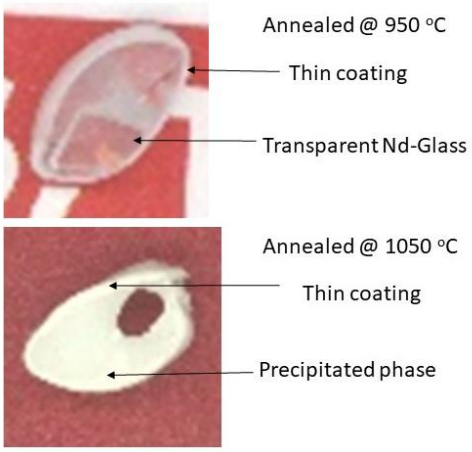

Fig. 5.4: Scan images of Nd-glass heat treated at 950 and 1050 °C. Surface precipitation at 950 °C and bulk precipitation at 1050 °C is shown.

Fig. 5.5 shows the sample holder used for polishing the rod sample. Optical polishing of the sample was carried out in-house. The surface quality of the polishing was better than λ/10 where λ= 632 nm. Scattering of the laser light (632 nm) was investigated inside the polished rod.

Fig. 5.5: Nd-glass rod holder used for polishing.

Fig. 5.6 shows laser light 632nm scattering inside the rod. The sample rod was held as shown in fig.5.6(a) and the laser light was allowed to pass through one end face. The rod was adjusted to ensure that laser light was falling on the rod-surface perpendicularly. An optical path could be observed inside the rod, which is more clear in the dark room and shown in fig. 5.6(b).

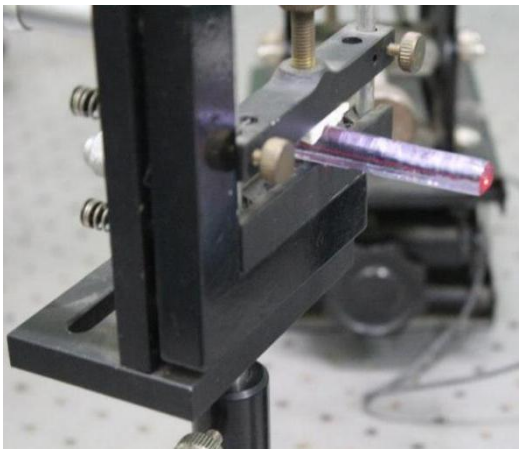

(a)

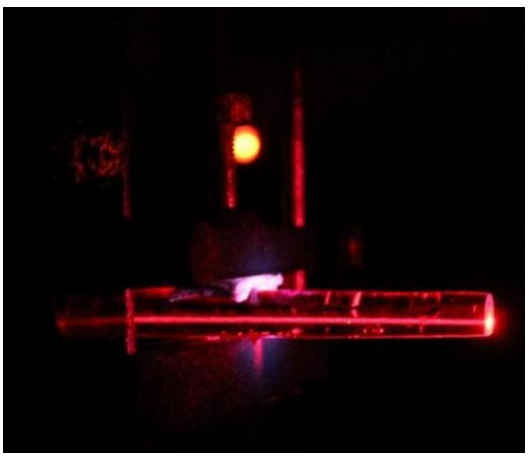

(b)

Fig. 5.6: (a) Nd-glass rod held during the scattering study and (b) optical path of laser light through the glass rod.

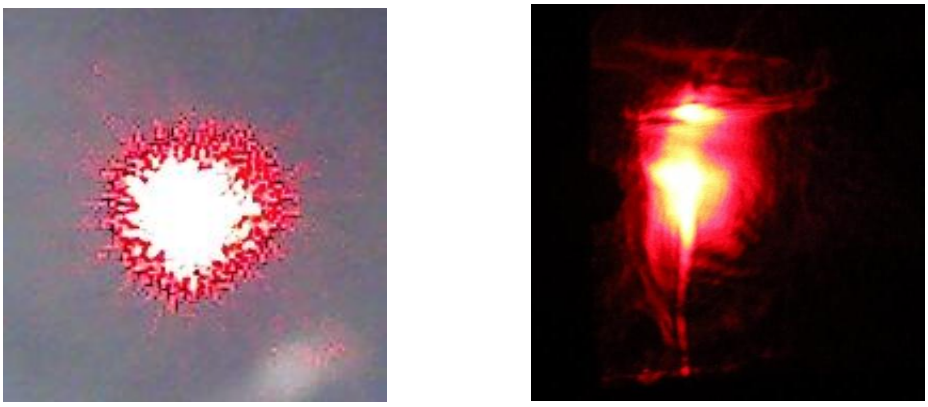

(a) (b)

Fig. 5.7: Laser light spot on the screen (a) before and (b) after keeping the sample in the path of the laser light.

Fig. 5.7 shows the spot size of the laser on the screen before and after passing through the Nd-glass rod. It is clear that small angle scattering of the light is causing a distortion in the spot size. The transmission of the laser light was calculated by relating the value observed on energy meter before and after inserting the rod in the path of the laser light. The calculated value of transmission is 68% at 632nm. This value if inferior to that observed ~ 81% transmission observed for section of the un-annealed sample, which is mainly due to scattering of the light. At present it is not known why the light is scattered inside the glass rod as there is no porosity or bubbles visible to the naked eye.

For comparison of spectroscopic characteristics, polycrystalline YAG was also synthesized using solid state route. The mixed raw materials of stoichiometric YAG composition containing 1.5 wt.% Nd_2O_3 were synthesized at 1750 ^oC for 4 h in a vacuum of 10^{-6} torr. The XRD data was recorded on a Rigaku X-ray diffractometer (Cu K_α source with $\lambda = 1.54$ Å) using a scan rate of 0.5°/min with 0.01° step size in the 2Θ range 20°–70° to confirm the crystal structure and the phase of the precipitates. The microstructure of the glass–ceramics were observed by a Field Emission Scanning Electron Microscope (FE-SEM, Carl Zeiss, SIGMA) equipped with energy dispersive spectroscopy (Oxford Inca X-Act LN2 free) for determination of precipitate size, morphology and elemental determination from a cut surface. The cut surfaces were sputtered by gold. The optical transmission spectra were recorded using

JASCO V670 spectrophotometer at room temperature in 200-1200 nm wavelength range with 0.5 nm step. The emission spectra were recorded with a FLS920-s fluorescence spectrometer (Edinburgh Instruments Ltd.) upon excitation at 585 and 808 nm in the range 600-1200 and 800-1200 nm wavelength range, respectively.

Chapter 6

Results and Discussion

6.1 XRD

The density of Nd-glass was measured by liquid displacement method using the Archimedes principle and found to be ~ 3.19 gm/cc. The refractive index was measured using refractometer and found to be 1.62 at 532 nm.

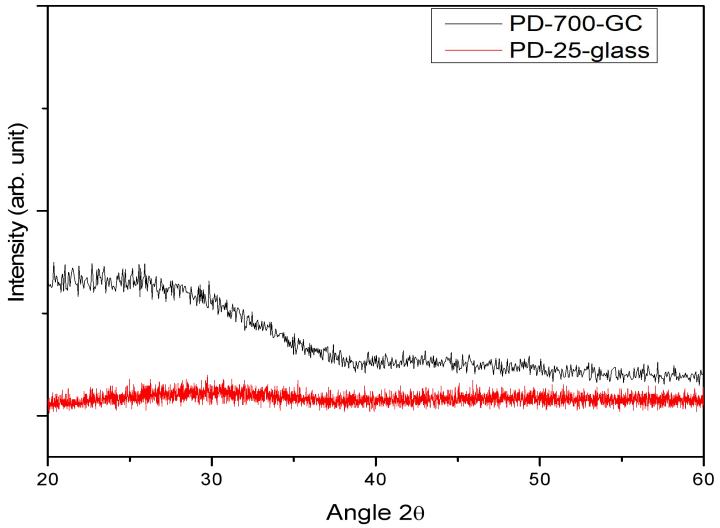

(a)

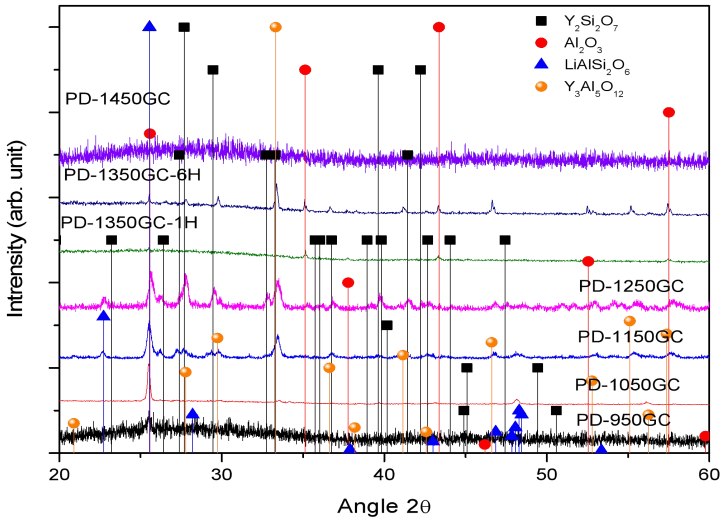

(b)

Fig. 6.1: Comparison of the powder X-ray Diffraction pattern of Nd-glass (a) before and after annealing at 700 ºC and (b) heat treated Nd-glass at 950-1450 ºC in air.

Fig. 6.1(a) compares the XRD pattern of the glass powder sample as prepared and annealed at 700 ºC one hour. There was no sharp diffraction peak observed for

Nd-glass consistent with its glassy nature and annealing at 700 °C also shows no crystalline nature. The XRD of the powder of heat treated sample at 950, 1050, 1150, 1250, 1350-1H, 1350-6H and 1450 °C are compared in Fig. 6.1(b). The sample annealed at 1450 °C is also glassy in nature and XRD pattern is similar to Nd-glass. Phase analysis for the glass annealed at 950 °C has revealed few minor peaks revealing the initiation of crystallization and on comparing with the JCPDF file 35-0797, it is determined that phase precipitated is $LiAlSi_2O_6$. The precipitation is observed to present only on the surface also shown in fig. 5.5(a). The interior of the sample remains transparent. Further annealing at 1050 °C resulted in second phase precipitation, which is established to be $Y_2Si_2O_7$ phase (JCPDF-38-0440). This precipitation is observed in the interior of the sample fig. 5.5(b) and the glass sample turned into an opaque glass. High temperature annealing (at 1150 °C) has resulted in the formation of another phase $Y_3Al_5O_{12}$ (YAG, JCPDF-33-40) along with other two initial phase, as shown in fig. 5.4(d). With increase in annealed temperature further (~ 1250 °C), the concentration of YAG phase increases and all three phases are present in different concentrations.

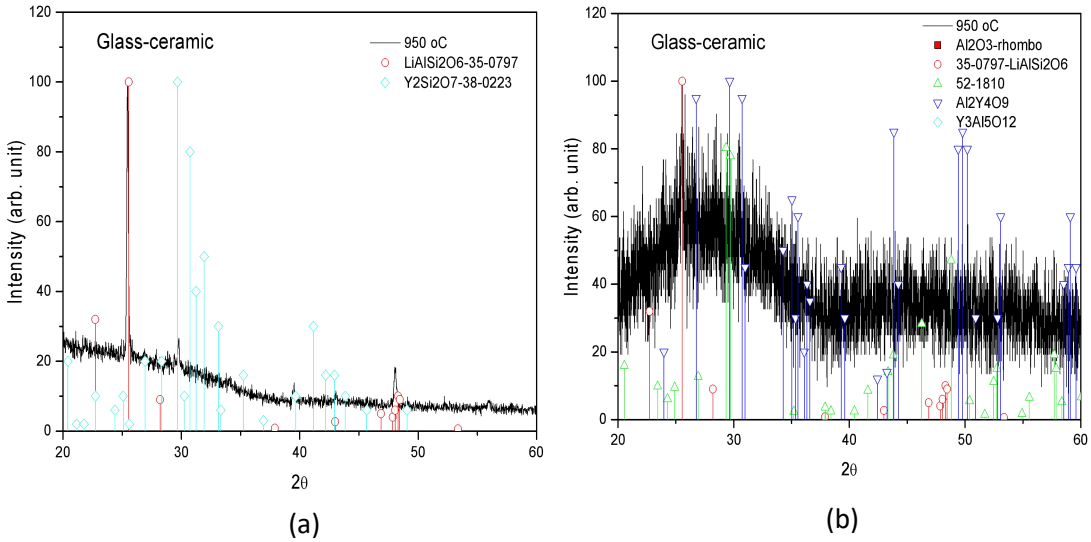

Fig. 6.2: XRD pattern of glass ceramic PD-950 sample (a) surface and (b) powder

Fig. 6.2 compares the XRD pattern of PD-glass annealed at 950 °C sample's surface and powder. A sharp peak of the annealed sample's surface is assigned to the $LiAlSi_2O_6$ phase but the XRD of the powder of this sample is similar to the glass having few crystalline peak superimposing on the noise. The powder XRD pattern of

the PD-1050, PD-1150 and PD-1250 are compared in Fig. 6.3. It is clear from this Fig. that as the annealing temperature increases from 1050 to 1250 °C, number of X-ray diffraction peaks are increased, which signifies the presence of multi-phase. After the first phase precipitation ($LiAlSi_2O_6$), the second phase $Y_2Si_2O_7$ concentration increases with annealing temperature followed by the third phase $Y_3Al_5O_{12}$ and $Y_3Al_4O_9$ formation at 1250 °C.

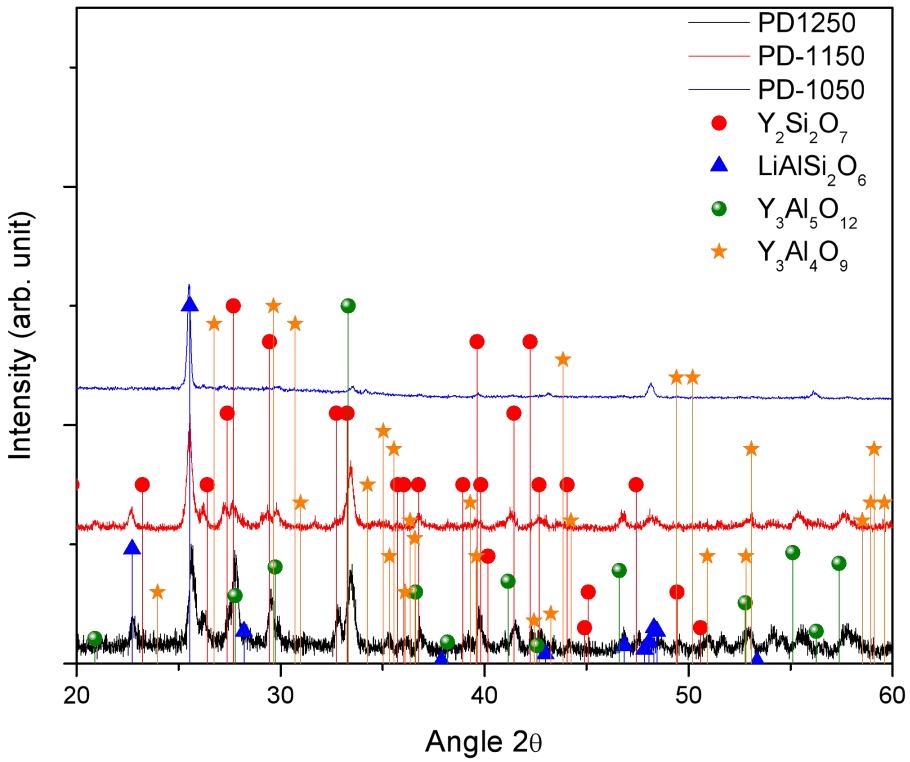

Fig. 6.3: Powder XRD pattern of PD-glass sample annealed at (a) 1050, (b) 1150 and (c) 1250 °C for 1 hour in air.

Higher temperature (1350 °C for 1 hour) treatment resulted in solubility of all initial precipitated phase, as shown in fig. 6.4(a). Few minor peaks are assigned to the presence of Al_2O_3 phase (JCPDF-10-173). No peaks corresponding to other three phases are observed. With increase in the dwell time at 1350 °C from 1 hour to 6 hours has resulted in the precipitation of major $Y_3Al_5O_{12}$ phase along with minor Al_2O_3 phase. All these precipitates finally dissolved in samples heat treated at 1450 °C for 1 hour, even higher dwell time of 6 hours has not resulted in any phase precipitation. Thus single YAG phase is observed in the Nd-glass sample which is

heat treated at 1350 °C for 6 hours. Precipitation of minor Al_2O_3 phase in this sample is unexpected, which seems to increase in concentration with heat treatment time.

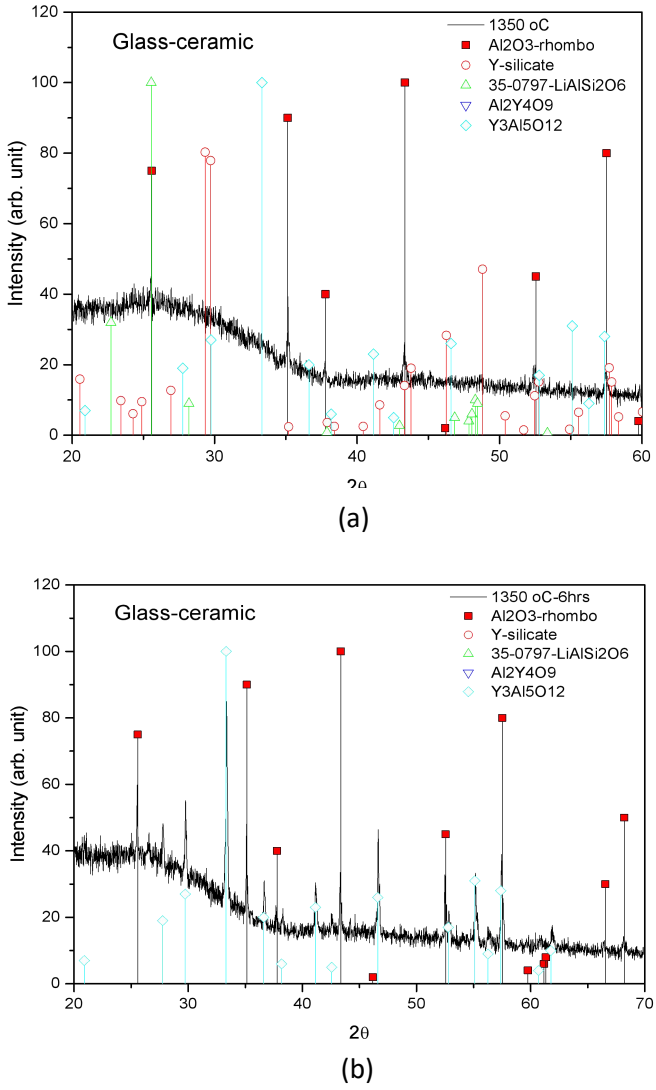

Fig. 6.4: Powder XRD pattern of Nd-glass sample annealed at 1350 °C for (a) 1hour and (b) 6 hours in air.

6.2 Fourier Transform Infra-red Spectroscopy

The infrared spectra of the all heat treated glass samples in 400-4000 cm^{-1} wavenumber range are compared in Fig. 6.5. A broad band near 3286-3600 cm^{-1} corresponds to the O-H stretching frequencies of water molecules attached to the surface. Similarly, an absorption band near 2834-2896 cm^{-1} corresponds to the C-H stretching frequencies of ethanol used during the cleaning of sample's surface. A dual absorption peak around 2361 cm^{-1} is known characteristics absorption peak of the

C=O bond stretching of atmospheric carbon dioxide. The peak around 1634 cm^{-1} is due to water molecule absorbed on the surface. An abnormality around 1407-81 cm^{-1} is attributed to the stretching vibrations arising from C-O, -CH_2 groups. The absorption band in the range 400-1200 cm^{-1} are assigned to the functional group of inorganic compounds, which is important for the present study. It is well reported that the building block for Nd-glass is the SiO_4 tetrahedron in which O-atom act as bridge between two tetrahedrons ultimately forming a fully polymerized network. Addition of Li (alkyl cation) acts as modifiers breaking oxygen bonds to form non-bridging oxygen (NBO) and the Li-ions are generally located close to the negatively charged NBOs at the interstitial site in the tetrahedral network to maintain the charge neutrality.

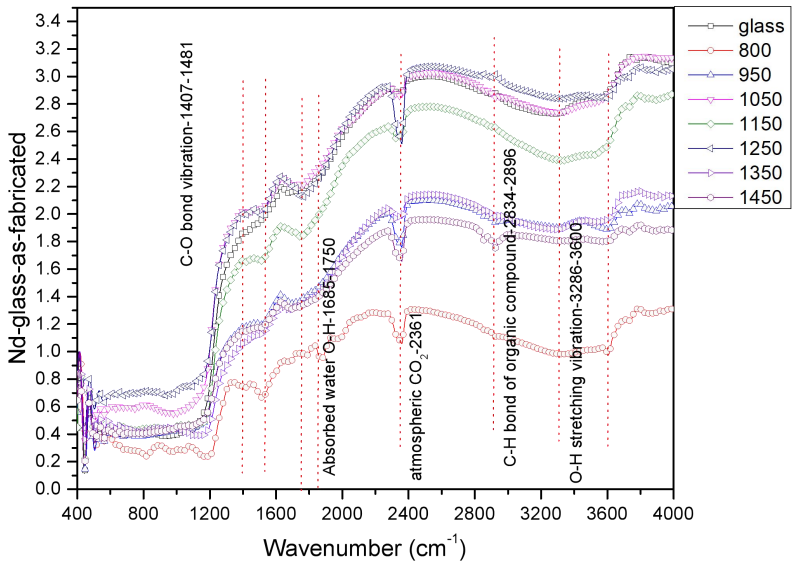

Fig. 6.5: Comparison of the heat treated Nd-glass samples IR-spectra in 400-4000 cm^{-1} wavenumber range. Major absorption bands are assigned.

Fig. 6.6 shows comparison of glass ceramic samples FTIR spectra in 400-800 cm^{-1} wavenumber range. A sharp peak in the range 400-500 cm^{-1} is due to the rocking vibration of Si-O-Si or Si-O-Al bonds present in the glassy network formed by SiO_4 and AlO_4 tetrahedral network bridging by O-atoms. Another sharp features in the range 500-600 cm^{-1} are assigned to the stretching vibration Y-O (563 cm^{-1}) and Al-O (505 cm^{-1}) or YAG. The medium intense peak around 563 cm^{-1} is attributed to the presence of yttrium silicate ($Y_2Si_2O_7$) and it corresponds well with the phase analysis. All the weak peaks in 600-700 cm^{-1} are due to stretching vibration of the Al-O bond

in AlO_6 or AlO_4, i.e., Al-ions in six or four-fold coordination around 621 or 686 cm^{-1}, respectively. A weak band around 752-756 cm^{-1} corresponds to AlO_4 tetrahedral substitution by SiO_4 through diffusion process, resulting in formation of β-spodumene $LiAlSi_2O_6$ phase. It has been reported (J. Sol.Gel.Sci & Tech (2024) 111, 718-24) that the tetrahedral arrangement of Al-ion and Si-ion share same occupancy site in random position within spodumene crystalline lattice structure. Thus the band around 750 cm^{-1} corresponds to vibration of Al-O bond in AlO_4 tetrahedral in spodumene and Al-ion substitution in SiO_4 tetrahedral.

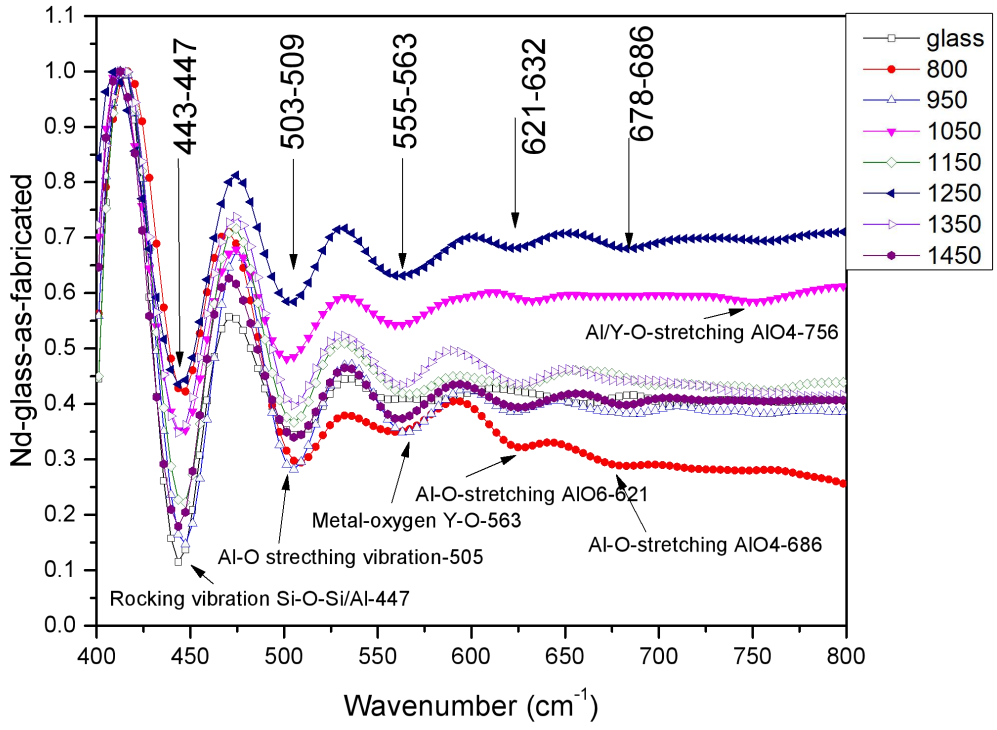

Fig. 6.6: Comparison of the heat treated Nd-glass samples IR-spectra in 400-800 cm^{-1} wavenumber range. All the major absorption bands are marked.

It should be noted that bending vibration of Si-O-Si and Si-O-Al generally observe at lower wavenumber than stretching vibration of Si-O-Si/Al and can be assigned to distinctive peak around 460 and 600-850 cm^{-1}, respectively. Moreover, asymmetrical vibration is observed at high wavenumber than symmetrical vibration and the wavenumber band in 800-1250 cm^{-1} range are assigned to asymmetrical vibration.

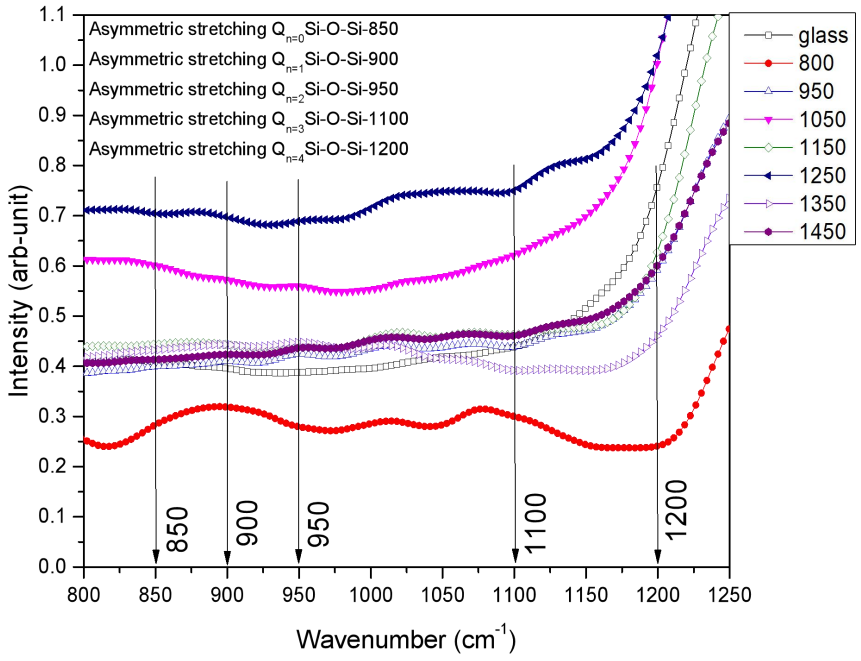

Fig. 6.7: Comparison of the heat treated Nd-glass samples IR-spectra in 800-1200 cm^{-1} wavenumber range. The absorption bands are due to the asymmetric stretching of Si-O-Si bond.

Fig. 6.7 shows number of weak bands in 800-1200 cm^{-1} wavenumber range corresponding to stretching vibration of SiO_4 tetrahedron with a different number of bridging oxygen. Peaks corresponding to stretching Si-O-Si and bending Si-O bonds are recognized at 1040 and 820 cm^{-1}, respectively. There are three vibrations bands corresponding to rocking, bending and stretching motions of O-atoms around 450, 800 and 1075-1150 cm^{-1} wavenumber, respectively reported in literature for vitreous SiO_2. It is also reported that the dominant feature in the IR absorption spectrum of SiO_2 is associated with stretching motion of the O-atoms and this motion is believed to couple with Si-atom motion in which both Si and O atoms move in opposite directions. Thus all O-atoms around a given Si-atom of SiO_4 building block move with the same phase and the Si-atom move with opposite phase. It is also mentioned that in-phase and out-of phase motion between Si and O-atom results into peak near 1075 cm^{-1} and at broad shoulder center around 1150 cm^{-1}, respectively. It is known that in yttrium aluminum-silicate glass, a wide distribution of structural unit Q_n varying from 0 to 4 are present, where Q refers to SiO_4 tetrahedral with n bridging O-atoms. It is also reported that the Al-ions are in 4 and 6-fold co-ordination.

It is well known that the symmetric and the anti-symmetric stretching modes of the Si-O-Si bonds of the Q_n units are active in the 800-1300 cm^{-1} region. The absorption bands of the Q_n units with n = 4,3,2,1 and 0 are centered around 1200, 1100, 950, 900 and 850 cm^{-1}, respectively and as marked in Fig. 6.7. This values shifts to lower wavenumbers when Al-atom replaces Si-atom due to the weaker Al-O bond. Generally, for the LAS glasses broad absorptions band are observed in FTIR spectra. Lack of sharp features is considered as disorder in the silicate network with a wide distribution of Q_n units. It may be noted that as-prepared Nd-glass has a main absorption band centered at about 937 cm^{-1} with a shoulder peak around 1095 cm^{-1}. This result indicates a distribution of Q_n units centered around the Q_2 or Q_3 unit. A weak absorption peak of Q_2 and Q_3 units is observed at lower wavenumber suggesting the substitution of Al-ions in SiO_4 tetrahedral. Intensity of the absorption band around 690 cm^{-1} with heat treatment temperature reflects the presence of Al-atoms in four-fold coordination. The absorption band at 918-929 cm^{-1} becomes prominent upon thermal treatment indicating the presence of more depolymerized units with lower n values, i.e., producing non-bridging O-atoms.

Fig. 6.8 compares the FTIR spectrum in the wavenumber region 800-1250 cm^{-1} of as prepared Nd-glass (PD-RT) and heat treated Nd-glass at 950 ^oC. There are number of extra absorption band at 922, 970 1038 and 1100 cm^{-1} clearly observed in PD-950 sample compared to PD-RT. The band at 1100 cm^{-1} is assigned to the Q_3 and suggesting that Si atom has one O-bridge less in Si-oxygen tetrahedron network suggesting breakdown of the SiO_4 tetrahedron network. Presence of new bands in PD950 sample suggests that different frequency required for new chemical bonding that has formed in this sample to absorb light passing through them and translated to an absorption. Correlating with X-ray diffraction study suggests that new absorption peaks are due to the precipitation of crystalline ($LiAlSi_2O_6$) phase from the amorphous phase. This phase precipitation phase after annealing has modified the chemical bonding in glass which has resulted in change in the absorption band wavenumber.

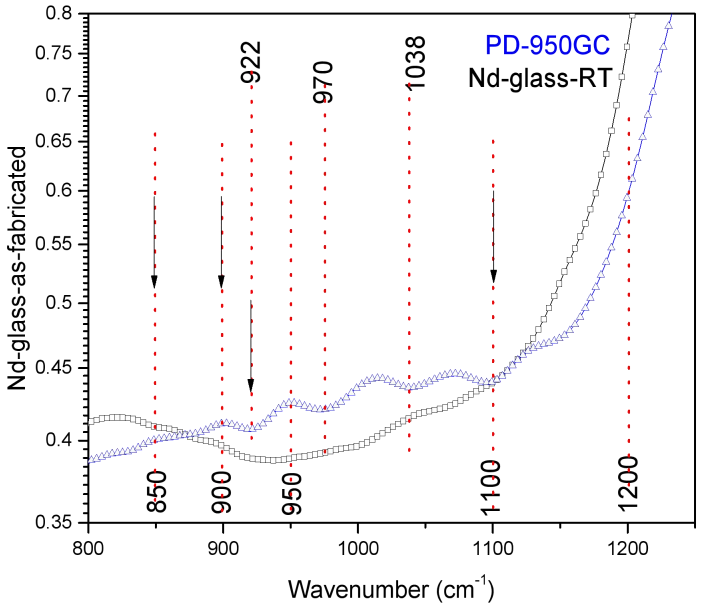

Fig. 6.8: Comparison of glass IR-spectra in 800-1200 cm^{-1} wavenumber range for heat treated Nd-glass PD-950 sample with not treated Nd-glass. The absorption bands are due to the asymmetric stretching of Si-O-Si bond.

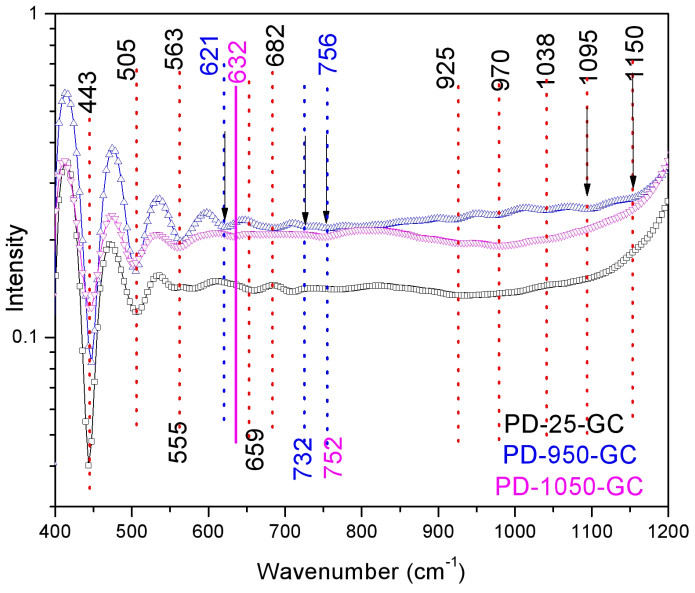

Fig. 6.9: Comparison of IR-spectra in 400-1200 cm^{-1} wavenumber range for heat treated Nd-glass PD-950 and PD1050 sample with not treated Nd-glass.

Fig. 6.9 compares the FTIR spectra of PD-RT and heat treated Nd-glass at 950 and 1050 °C. It may be noted that high temperature treated sample (PD-1050) has broad band similar to the parent glass in 800-1250 cm^{-1} wavenumber range. A new weak band around 631 cm^{-1} is assigned to the stretching modes of Al-O in hexa-coordination in AlO_6 units. This band is related to the structural relaxation in SiO_4 units and also to yttrium involvement in crystalline phase. (YAS-ceramic international, 44 (2018)) Absence of modes in 1050 to 1100 cm^{-1} wavenumber range is attributed to the presence of $Y_2Si_2O_7$ phase, which is also confirmed from XRD phase analysis. The band at 756 cm^{-1} is assigned to the Al-O stretching vibration in $LiAlSi_2O_6$ phase. Thus PD-1050 sample has two precipitates phase and this is consistent with the XRD-analysis.

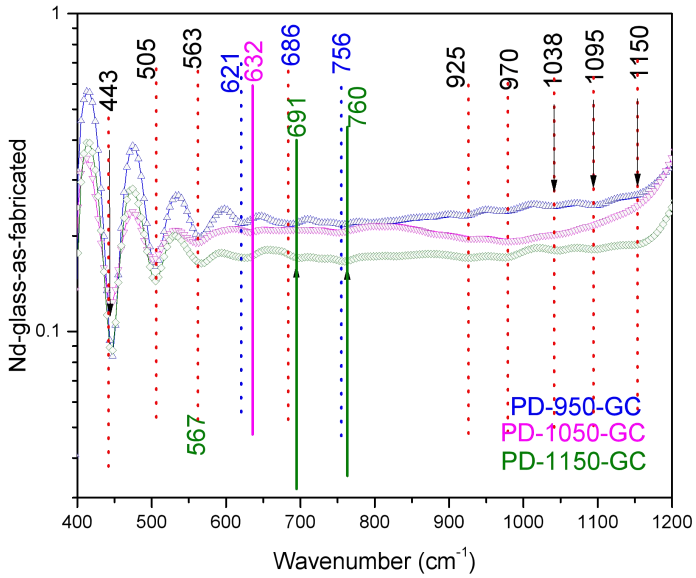

Fig. 6.10: Comparison of IR-spectra in 400-1200 cm^{-1} wavenumber range for heat treated Nd-glass PD-950, PD1050 and PD1150 sample.

Fig. 6.10 compares the IR spectra of PD-RT glass thermally treated at 950, 1050 and 1150 °C. There are two sharp bands near 443 and 505, which does not change with annealing temperature and are attributed to the rocking of Si-O-Si and stretching of Al-O in AlO_4 tetrahedral. A band at 560 cm^{-1} is due to Al-O in Al_2O_3 and clearly shifted to higher wavenumber from 563 to 567 cm^{-1}. It may be noticed that the spectra of PD-950 and PD-1150 are similar in 800-1200 wavenumber range but the band at 686 and 756 cm^{-1} are observed to shift by 4-5 cm^{-1}, which is due to the

presence of another phase. Phase analysis has revealed that a new YAG phase is formed along with $LiAlSi_2O_6$ and $Y_2Si_2O_7$ phase.

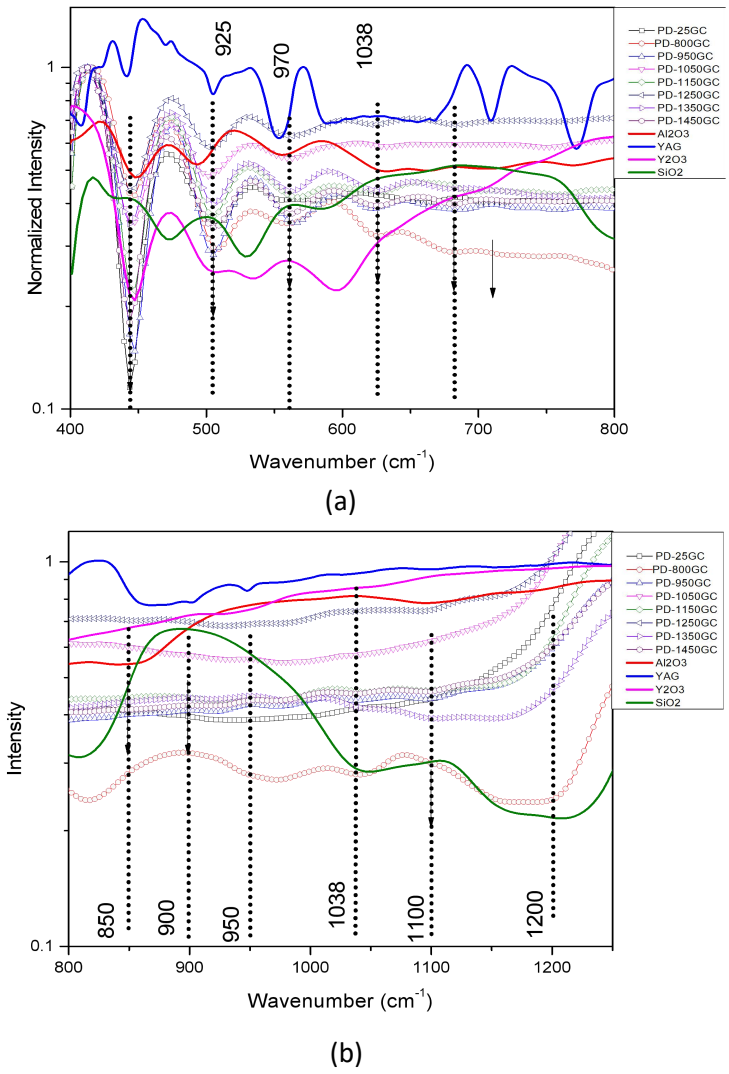

Fig. 6.11: Comparison of heat treated Nd-glass IR-spectra in (a) 400-800 and (b) 800-1250 cm^{-1} wavenumber range with Al_2O_3, Y_2O_3, SiO_2 and YAG IR-spectra.

Fig. 6.11 compares the FTIR spectra of Nd-glass annealed at different temperature with the spectra of Al_2O_3, Y_2O_3, YAG and SiO_2 powder in 400-800 and 800 to 1250 cm^{-1} wavenumber range. All the absorption peaks are also presented in Table 6.1. It is clear from this comparison that four strong absorption peaks are mainly due to the metal Y/Al-O stretching and shift in the absorption peak is due to the ion present in different surroundings, stating the precipitation of the phase.

Absorption peak in 800-1250 cm^{-1} wavenumber is due to the asymmetric/symmetric stretching of Si-O with different Q_n. Presence of different Q_n indicates the breaking of SiO_4 tetrahedral linkage giving lower Q_n resulting in non-bridging O-atoms.

Table 6.1: Wavenumber comparison for absorption band present in heat treated sample against the standard SiO_2, Y_2O_3, Al_2O_3 and YAG sample.

SiO_2	Y_2O_3	Al_2O_3	YAG	GC-25	GC-950	GC-1050	GC-1150	GC-1250	GC-1350	GC-1350-6H	GC-1450	Identification
431	447	447	442	443	447	443	447	443	443	443	443	R Si-O-Si, Al/Y-O in Y/AlO_4
474	501	494	504	505	505	501	505	505	505	505	505	S Y/Al-O in Al_2O_3, Y_2O_3 or YAG
528	536	555	552	555		559			559	559		S Al-O in YAG
					563		567	563			563	S Al-O in Alumina
586	598		589	578								S Y-O
		632			621	632	625	621	625	629	625	S Al-O in AlO_6
												Sym S Si-O-Si
		663	667	659	686		690	683	678		682	S Al/Y-O in Y/AlO_4
		706	709	710	732		729			721	729	S Y-O
					756	752	760	756	745			S Al-O in $LiAlSi_2O_6$
		771	770							771		S Al-O in YAG
850			863					856		856		Asym S Si-O-Si, $Q_n = 0$
			881			879						S Al-O in AlO_6
900			902		922		926	929	918	918	925	Asym S Si-O-Si, $Q_n = 1$
950			948	937		933						Asym S Si-O-Si, $Q_n = 2$
			978		972	980	976	976	983	980	970	S Al-O in YAG
1050					1037	1041	1045		1041		1038	S Si-O-Si in SiO_4
										1072		Asym S Si-O-Al
1100				1095	1100		1100	1091			1095	Asym S Si-O-Si, $Q_n = 3$

								1153	1157		1150	
1200												Asym S Si-O-Si, $Q_n = 4$

R = Rocking, S = Stretching, Sym = symmetric stretching, Asym = Asymmetric stretching,

Qn = SiO_4 with O bridge (= 0, 1, 2, 3, 4)

400-600 Bending vibration of Si-O-Si or Si-O-Al linkage

600-800 Stretching vibration of the Al-O bonds in AlO_4 (Al-ions in four-fold coordination)

800-1200 Stretching vibration on SiO_4 tetrahedron with a different number of bridging oxygen

Fig. 6.12(a) compares the IR spectra of PD-RT glass thermally treated at 1350 ^oC for 1 and 6-hours. There are two sharp bands near 443 and 505 cm^{-1}, which does not change with heat treatment time and are attributed to the rocking of Si-O-Si or stretching of Y/Al-O in Al_2O_3 or Y_2O_3 tetrahedral. A band at 563 and 629 cm^{-1} is due to Al-O in Al_2O_3 and clearly shifted to lower wavenumber by 4-5 cm^{-1} with increase in heat treatment time at 1350 ^oC, which may be related to the presence of YAG phase. Phase analysis has revealed that a new YAG phase is formed in PD-1350 with increase in time. Fig. 6.12(b) compares the IR spectra of Nd-glass with heat treated Nd-glass PD-1350 and PD-1450. Absorption band at 578, 659 and 710 cm^{-1} for PD-RT glass is absent in heat treated PD-1350 and PD-1450 samples, suggesting compositional changes in these sample. Phase analysis has revealed that all these samples are glass without any significant crystallization. Higher temperature heat treatment (PD-1450) dissolves all the precipitated phase and glass composition may be adjusted towards its original glass composition.

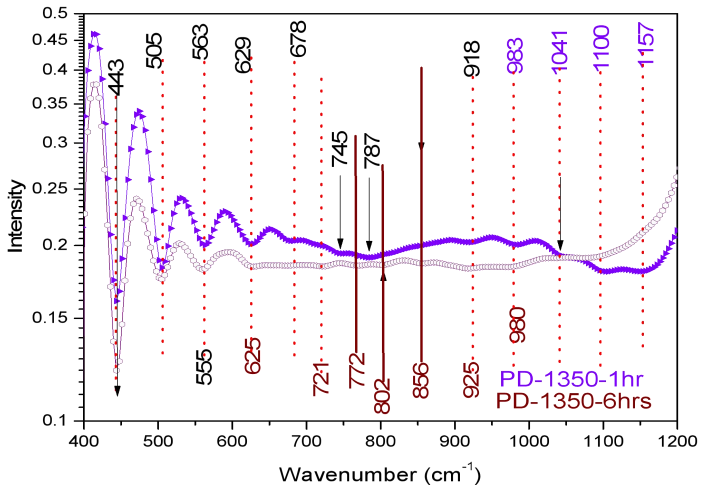

(a)

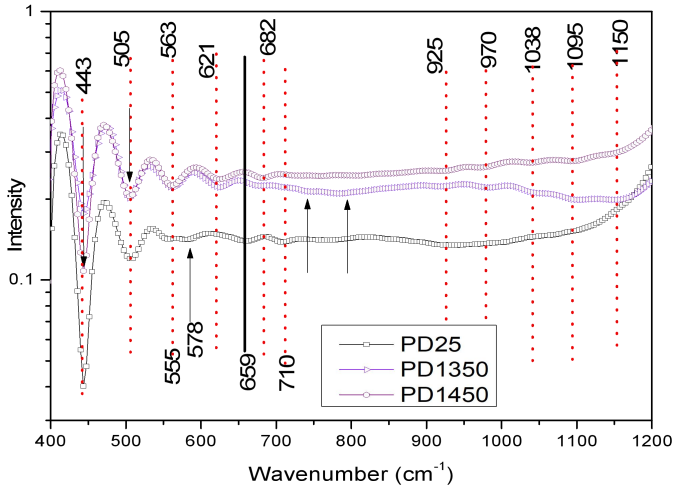

(b)

Fig. 6.12: Comparison of IR-spectra in 400-1200 cm^{-1} range for (a) heat treated Nd-glass at 1350 °C for 1 and 6 hours, (b) Nd-glass before and after heat treatment at 1350 and 1450 °C.

6.3 Hardness Test

The Vickers hardness test is used to determine the hardness of the glass and heat treated glass at different temperature. In this test, an indenter of square shape is pressed under a load of 50 gm for 10 seconds into the sample and then removed. The diagonals of the resulting indentation are measured. The angle between the two faces of diamond indenter used in Vickers hardness test is 136° and the faces makes an angle 22° with the horizontal, as shown in Fig. 6.13.

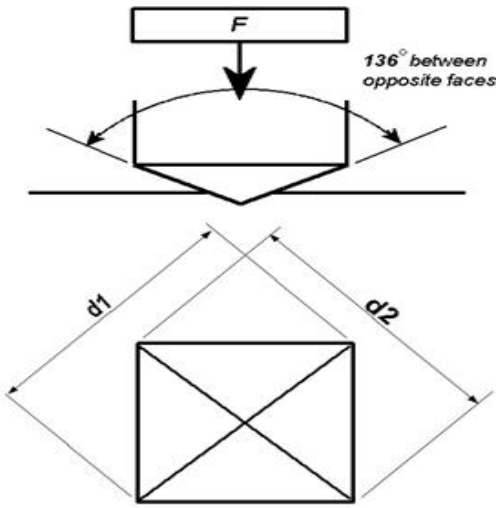

Fig. 6.13: schematic of the indenter used for determining the hardness.

Hardness number is measured at three places on the sample and average value is mentioned in Table 6.2. It is clear from this table that as-prepared glass has average Vickers hardness number 887 which decreases to 842 as the heat treatment temperature is increased to 950 ^{o}C, where $LiAlSi_2O_6$ phase is precipitated at the surface. As the heat treatment temperature is increased further, yttrium silicate and YAG phases are formed in the bulk and average Vickers hardness is increased to 1017 for PD-1150. Further heating resulted in dissolution of the yttrium silicate and $LiAlSi_2O_6$ phases and average Vickers hardness decreases to 922 for PD-1350. Heating to 1450 ^{o}C dissolve all the precipitated phase and the glass so obtained has a Vickers hardness number 867. It is known that yttrium silicate is a hard material and precipitation of this phase in the heat treated Nd-glass correlate well with hardness number.

Table 6.2: Hardness of the heat treated Nd-glass sample

Sample	Hardness-1	Hardness-2	Hardness-3	Average hardness number Kg/mm^2	Average Hardness number GPa
Pd-25GL	856	867	938	887	90.5

PD-750	867	845	845	852	86.9
PD-950	824	824	878	842	85.9
PD-1050	1004	926	1018	983	100.3
PD-1150	1063	1063	926	1017	103.8
PD-1350	938	913	915	922	94.0
PD-1350-6hr	890	926	951	922	94.0
PD-1450	878	845	878	867	88.5

6.4 Thermal Expansion Coefficient Investigation

The Nd-glass sample is heated to different temperature in order to precipitate phases. Depending upon the temperature, different phases are precipitated in the glass matrix. Phase precipitation is believed to take place through nucleation and growth process. Differential Thermal Analysis (DTA) or differential Scanning Calorimetry (DSC) are mainly reported to determine the nucleation and crystal growth temperatures in the glass sample. Few reports also highlight the usage of Dilatometer technique to determine these temperatures.

In the present study, the Nd-glass sample is heated at 4 ^{o}C/minute rate to 950 ^{o}C and change in the thickness of the sample is measured. The sample is heated in vacuum (~ 5 x 10^{-7} torr) and the sample is held under 250mN force to ensure physical contact between the sample and control rod. The measured displacement is corrected for the thermal expansion of the graphite rod.

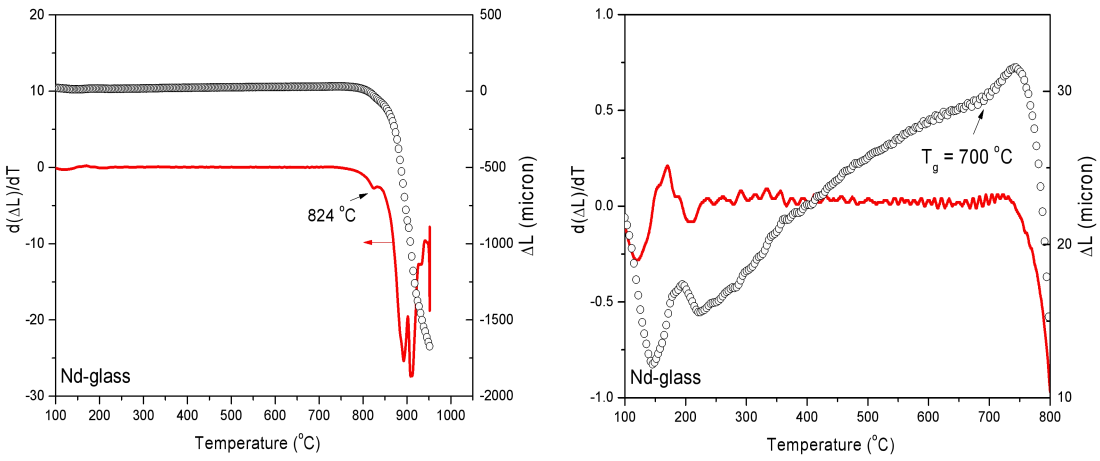

(a) (b)

Fig. 6.14: shows (a) change in thickness of Nd-glass sample and its derivative during heating from 25 °C to 950 °C, (b) expanded view revealing the T_g of the glass.

Fig. 6.14(a) shows change in thickness of Nd-glass sample during heating from 25 °C to 950 °C. This Fig. also shows a derivative plot clearly showing three anomalies. The first anomaly is near 824 °C may be related to the nucleation of the phase. Another two anomalies near 880-900 °C may be growth of the phase and melting of the sample, respectively. After the dilatometer test, the sample was melted and found sticking to the sample holder.

Fig. 6.14(b) shows enlarge portion of the plot showing an anomaly corresponding to T_g near 700 °C, which is consistent with the earlier report in which sudden upward change in the thickness is assigned to the glass transition temperature.

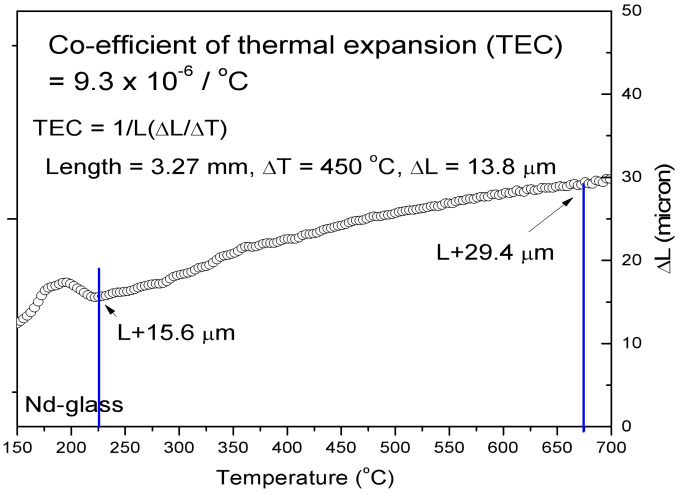

(a)

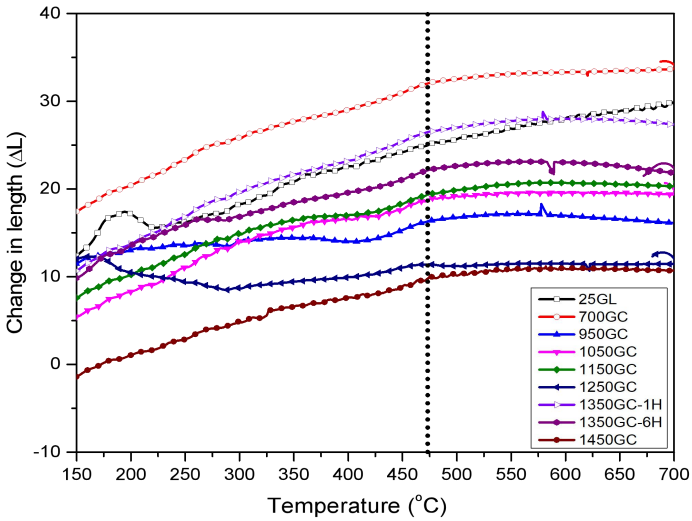

(b)

Fig. 6.15: shows (a) change in thickness of Nd-glass sample and TEC calculation during heating from 225 °C to 675 °C, (b) comparison of dimensional change for all heat treated samples.

Almost linear change in thickness between 250 to 600 ^{o}C is used to determine the linear thermal expansion coefficient. Fig. 6.15(a) shows dimensional change used in determining the thermal expansion coefficient (TEC) of 9.3 x 10^{-6} / ^{o}C for Nd-glass. Initial abnormal change in the sample thickness up to ~200 ^{o}C is due to the thermal lag between the sample and furnace temperature during initial controlling.

All the Nd-glass cut samples is heat treated to different temperature (700-1450 ^{o}C) in an atmospheric furnace to facilitate the precipitation. For TCE measurement, all these samples are heated to 700 ^{o}C and change in thickness is compared in Fig. 6.15(b). It is clear that there are two regions in which the change in thickness differ and are separated with a vertical line. The calculated TEC values between 150-400 ^{o}C and between 500-600 ^{o}C region are compared in Table 6.3

Table 6.3 comparison of TEC for all heat treated Nd-glass sample in different temperature range.

Sample	TEC (150-400 ^{o}C) x 10^{-6}	TEC (500-600 ^{o}C) x 10^{-6}
PD-25-glass	9.3	9.3
PD-700GC	38.6	5.0
PD-950GC	14.2	3.1
PD-1050GC	37.1	3.1
PD-1150GC	26.2	5.6
PD-1250GC	4.7	1.5
PD-1350GC-1H	45.1	8.9
PD-1350GC-6H	24.8	2.6
PD-1450GC	35.4	7.4

This table clearly shows that as prepared Nd-glass sample has a thermal expansion coefficient 9.3 x 10^{-6}/^{o}C in 150-600 temperature range. Heating Nd-glass to higher temperature has minimal effect on the TEC in 500-600 ^{o}C regime. The TEC is found to increase when the Nd-glass is heated to 700 ^{o}C but for this sample no precipitation is observed. An increase in the TEC may be due to glass composition readjustment. Further heating (950 ^{o}C) has shown a decrease in the TEC, which is due to the $LiAlSi_2O_6$ phase formation on the surface. The TEC of the sample annealed at 1050

^{o}C is higher because of the $Y_2Si_2O_7$ phase precipitation in the glass. With increase in the annealing temperature to 1150 ^{o}C, these phases are present in different fraction along with a new YAG phase. The TEC decreases drastically from 26.2 to 4.7 x 10^{-6} / ^{o}C when the annealing temperature is increased from 1150 to 1250 ^{o}C, which is attributed to the change in the concentration of different phase precipitations.

Phase analysis has revealed that YAG phase is a major phase in PD-1350-6H sample, which has lower thermal expansion coefficient that PD-1350-1H. This reveals that YAG phase has lower thermal expansion coefficient than heat treated Nd-glass (PD-700GC). Heating Nd-glass to 1450 ^{o}C dissolve all the precipitated phase and the sample is transparent as glass but the TEC is similar to thermally treated Nd-glass (PD-700GC). This study clearly shows that TEC of the glass ceramic can be controlled by heating the glass and optimizing the precipitates concentration.

6.5 Scanning Electron Microscopy

Heat treated Nd-glass at 900 and 1300 °C is examined for crystallization, composition and impurites present inside the sample under a scanning electron microscope. These samples had a thin layer of gold on the annealed surface to avoid charging during microstructure investigation. In the middle of the sample, big chunk and few dark features are observed (fig. 6.16a-b). The area near the edge of the sample is dipicted in (fig. 6.16c-d), which presents the begining of phase precipitation. The precipitation phase is $LiAlSi_2O_6$ as confirmed from X-ray diffraction study. The size of the precipitation is clearly nanometer in size. A dark line in fig. 6.16(d), is a crack present inside the glass sample, which may have happened during cutting of the sample for SEM investigation.

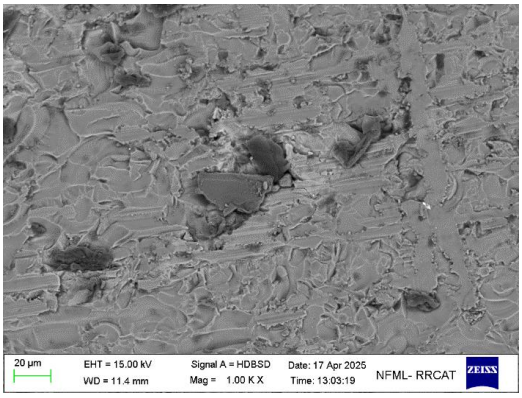

(a)

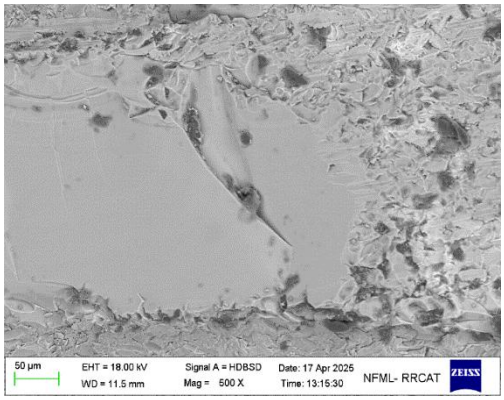

(b)

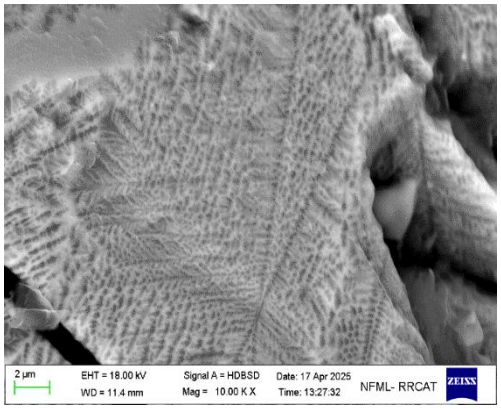

(b)

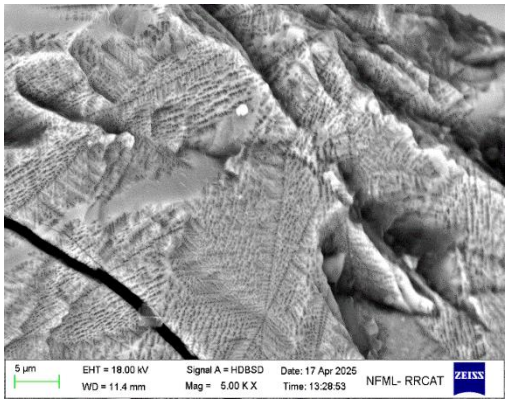

(d)

Fig. 6.16: SEM image of the Nd-glass annealed at 900 °C. Dendrite like features are observed near the edge of the sample.

Further energy dispersive X-ray spectroscopic analysis is carried out to determine the precipitate phase and glass matrix composition.

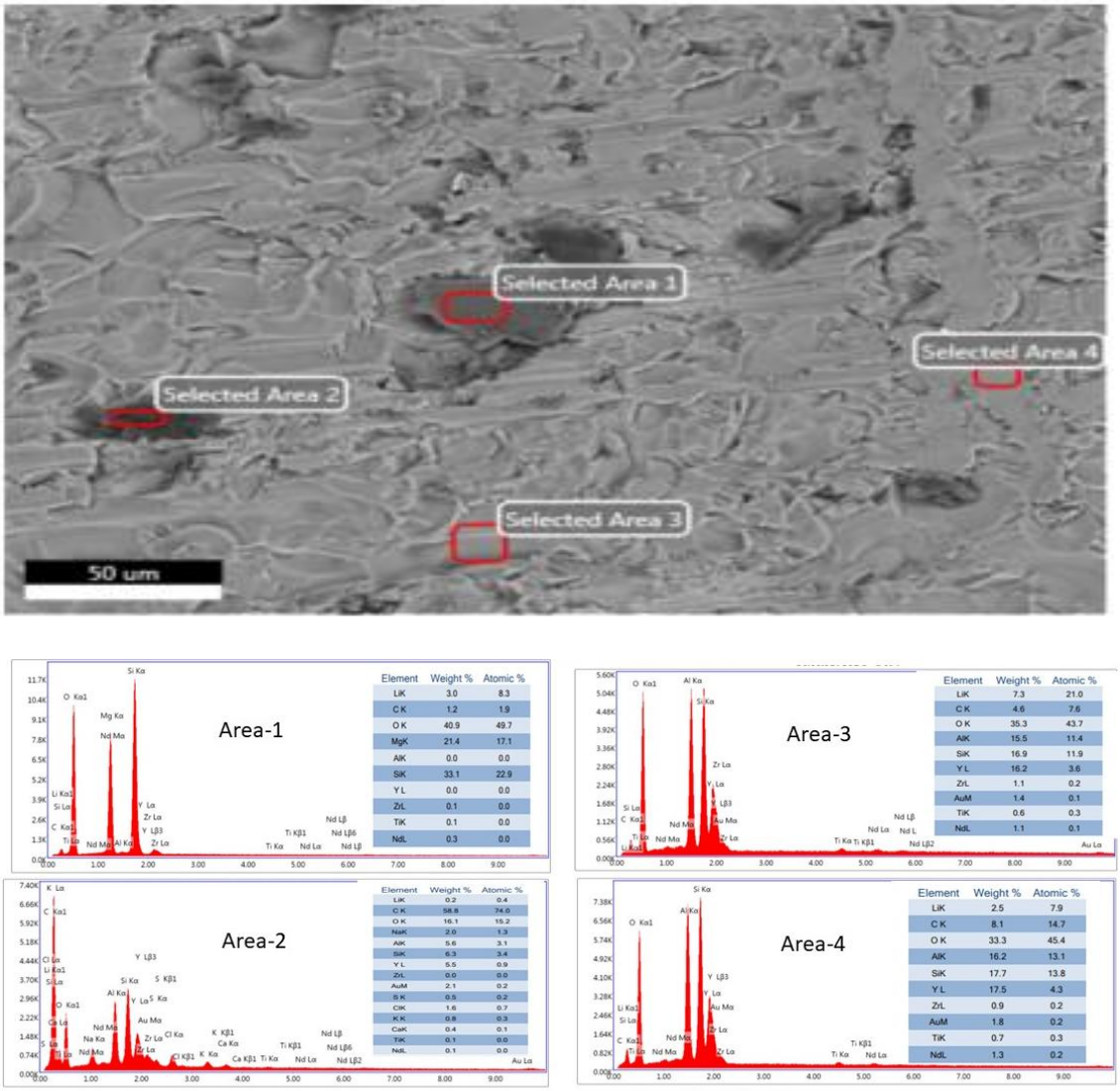

Fig. 6.17: SEM image and EDX spectra of central part of Nd-glass annealed at 900 ^{o}C for 1 hour. Area for which the EDX spectra is shown are marked as area 1, 2, 3 and 4.

Fig. 6.17 reveals the secondary electron images and energy-dispersive x-ray spectrographs of Nd-glass annealed at 900 ^{o}C for 1 hour in Ar-atmosphere. The number with selected area marked on the SEM images corresponds to the EDX spectra shown in fig. 6.17. Table 6.4 compares the elemental composition at a specific area to the glass composition used initially. It is observed from the EDX spectra of area 3-4 that the sample has small carbon impurities (~ 4.6 -8.1 wt.%). The

area 2 has large carbon impurity (~ 58.8 wt.%) along with minor Na, K, Ca-impurities. The carbon impurity is due to the fact that these samples are heat treated in graphite crucible. Presence of Na, Ca and K impurities in the selected area 1 may be due to the starting laboratory reagents used to prepare these samples.

Table 6.4: Comparison of various element present in region as marked with Nd-glass composition.

sample	Li	O	Al	Si	Y	Zr	Ti	Nd	Impurity (wt.%)
Nd-glass composition (Wt.%)	1.4	42.0	15.9	17.3	20.5	1.1	0.6	1.3	-
Area-1	3.0	40.9	0	33.1	0	0.1	0.1	0.3	Mg (21.4), C (1.2)
Area-2	0.2	10.1	5.6	6.3	5.5	0	0.1	0.1	C(58.8), Na(2.0), K (0.8)
Area3	7.3	35.3	15.5	16.9	16.2	1.1	0.6	1.1	C(4.6)
Area-4	2.5	33.3	16.2	17.7	17.5	0.9	0.7	1.3	C(8.1)

Table 6.4 compares the concentration in weight percent of various element present in the 1-4 area with that of the glass composition. The area 4 is the glass having composition similar to the glass powder. The region (area 3) is a Lithium-ion rich glass suggesting that precipitation of lithium compound phase may occur in nearby area. The area 1 corresponds to flakes where lithium silicate phase precipitation has already occurred. It is interesting to note that no Al-ion concentration has been detected stating that no $LiAlSi_2O_6$ phase has been formed at 900 ^oC, which is consistent with the scan image where the precipitation is mainly on the surface.

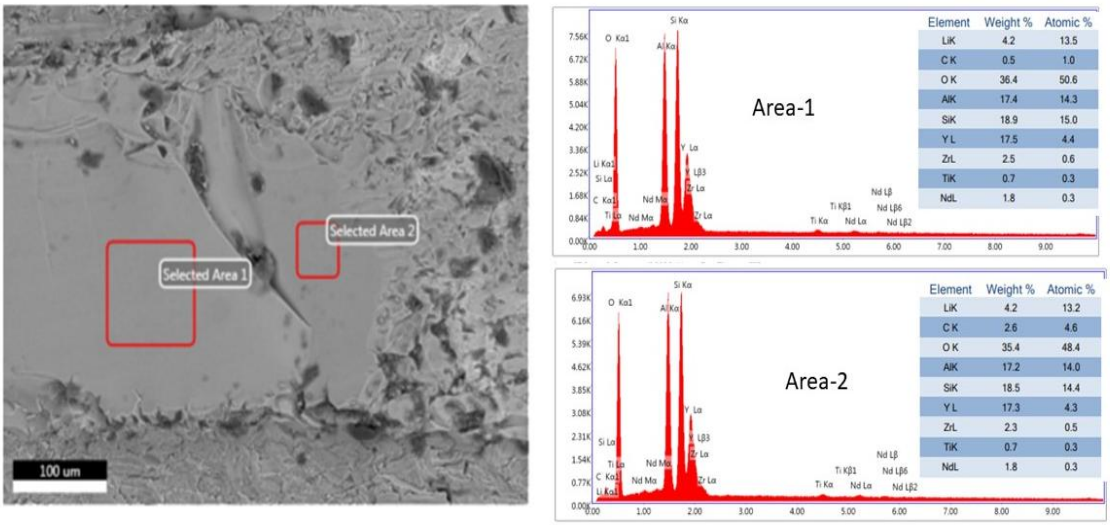

Fig. 6.18: SEM image and EDX spectra of near the edge of Nd-glass annealed at 900 oC for 1 hour. Area for which the EDX spectra is shown are marked as area 1, and 2.

Table 6.5: Comparison of various element present in region as marked with Nd-glass composition.

sample	Li	O	Al	Si	Y	Zr	Ti	Nd	Impurity (wt.%)
Nd-glass composition (Wt.%)	1.4	42.0	15.9	17.3	20.5	1.1	0.6	1.3	-
Area-1	4.2	36.4	17.4	18.9	17.5	2.5	0.7	1.8	C(0.5)
Area-2	4.2	35.4	17.2	18.5	17.3	2.3	0.7	1.8	C(2.6)

Fig. 6.18 shows the SEM images of area near the edge of the sample. Both EDX spectra are similar to each other as shown in Table 6.5. The comparison of element weight % with the starting glass composition suggests that this region is Li, Al and Si-rich revealing the presence of $LiAlSi_2O_6$ phase. As one can see that this region has low Y-concentration, which suggests that this is not the glass region and presence of high concentration of Zr confirms that Zr-ions are acting as nucleating site for $LiAlSi_2O_6$ phase.

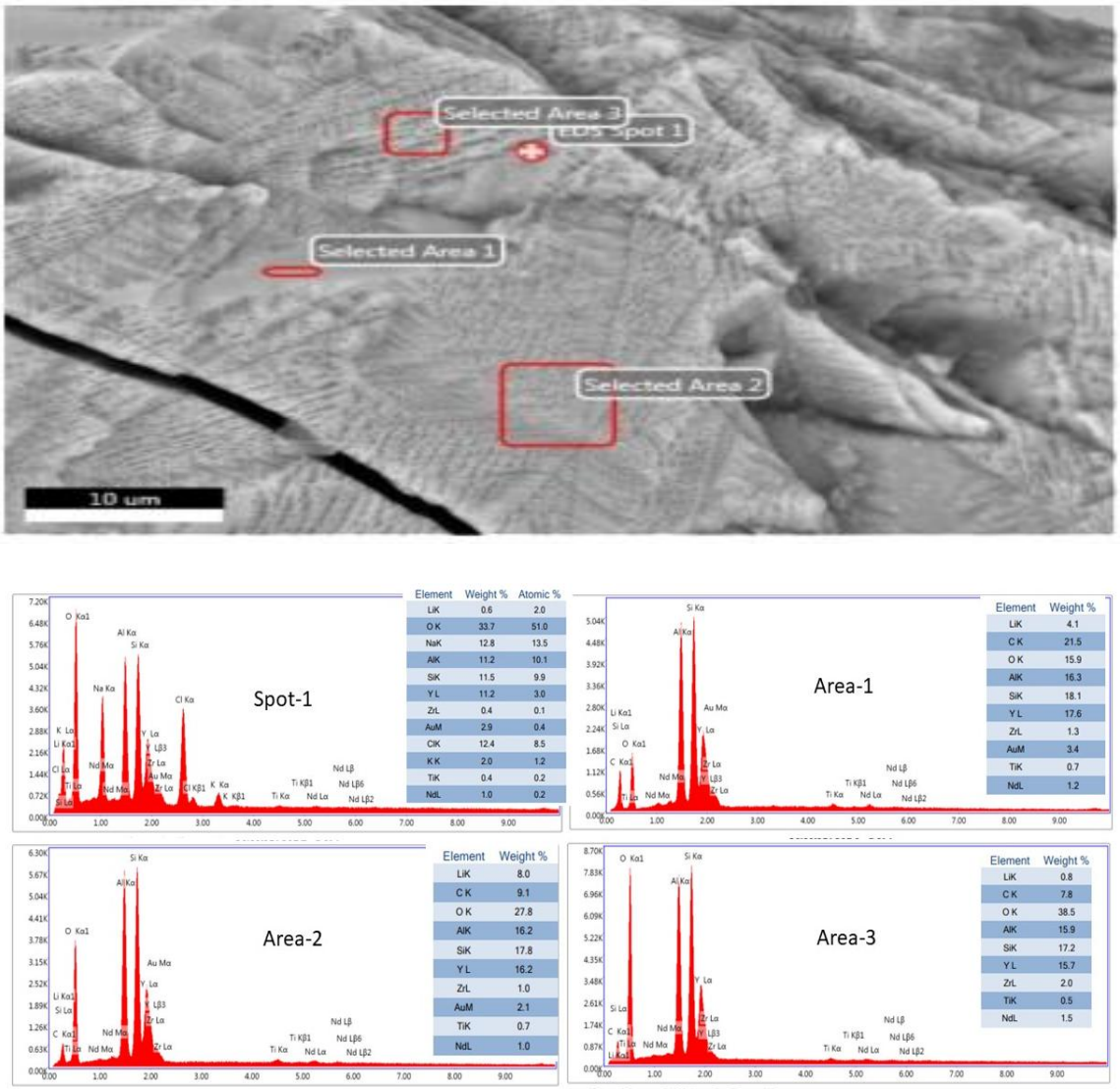

Fig. 6.19: SEM image and EDX spectra taken at the edge of Nd-glass annealed at 900 ^{o}C for 1 hour. Area for which the EDX spectra is shown are marked as area 1, 2, 3 and 4.

Table 6.6: Comparison of various element present in region as marked with Nd-glass composition.

sample	Li	O	Al	Si	Y	Zr	Ti	Nd	Impurity (wt.%)
Nd-glass composition (Wt.%)	1.4	42.0	15.9	17.3	20.5	1.1	0.6	1.3	-

Spot-1	0.6	33.7	11.2	11.5	11.2	0.4	0.4	1.6	C(12.4), Na(12.8), K (2.0)
Area-1	4.1	15.9	16.3	18.1	17.6	1.3	0.7	1.2	C(21.5)
Area-2	8.0	27.8	16.2	17.8	16.2	1.0	0.7	1.0	C(7.1)
Area-3	0.8	38.5	15.9	17.2	15.7	2.0	0.5	1.5	C(7.8)

Fig. 6.19 shows that SEM images near the edge, where dendrite like features are clearly seen. Table 6.6 compares the weight % of the element present with the as-prepared glass composition. It is clear that spot 1 has composition with deficiency of all the elements. This region has mainly carbon and sodium ion impurities. Near to the spot 1, there is a region (area1), where Li, Al and Si are in higher concentration suggesting that precipitation of $LiAlSi_2O_6$ phase is due to the diffusion of the elements within the glass matrix. Region 2 and 3 on the Fig. 6.19.where dendrite like precipitation has already occurred, has composition Li-rich and Li-deficient, respectively. This study has confirmed that precipitation of first phase ($LiAlSi_2O_6$) has occurred near the surface and Li-diffusion mainly responsible for the nucleating of the phase at the Zr-site.

Fig. 6.20 shows SEM images of the Nd-glass sample thermally heated at 1300 ^oC. There are regions where plates like white regions (2-5 micron) size are clearly seen. Few clusters of white flake are also observed near to the regions, which shows dendrite like growth. The size of the precipitation is clearly nanometer in size. Dendrite like growth is also accompanied by regions where the growth has resulted into large size precipitates. Dendrite like phase precipitates near the molten regions. To determine the precipitate phase and glass matrix composition, an energy dispersive x-ray spectroscopic analysis is presented.

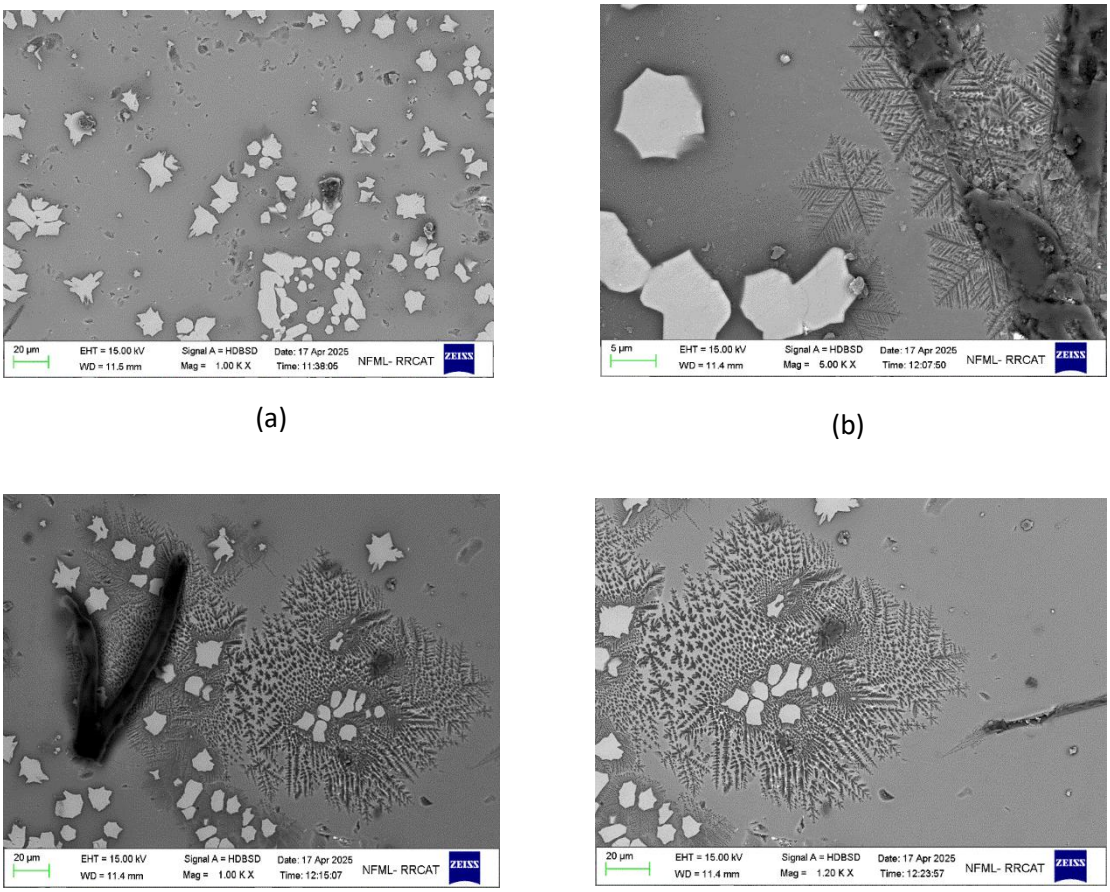

(a) (b)

(c) (d)

Fig. 6.20: SEM image of the Nd-glass annealed at 1300 ºC. Dendrite like features along with particulates are observed in the center of the sample.

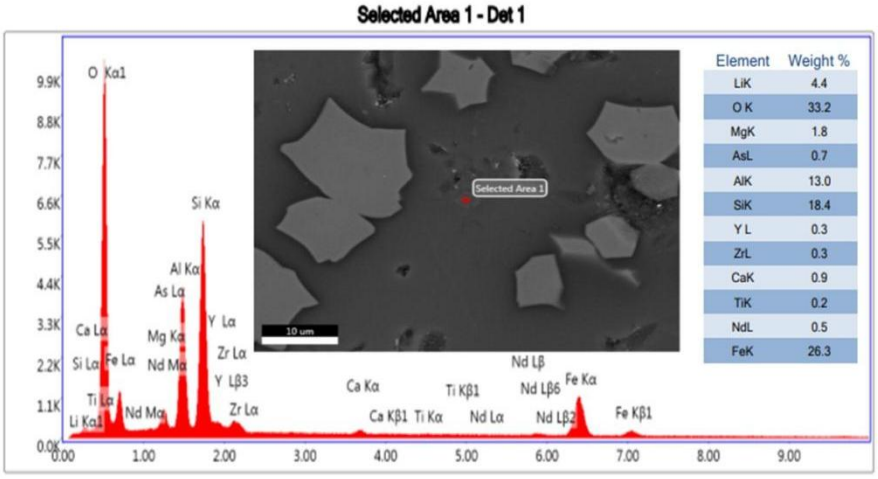

Fig. 6.21: SEM image (inset), EDX spectra and table with weight % of various element present in area 1 of thermally treated Nd-glass sample.

Fig. 6.21: reveals the secondary electron images and energy-dispersive x-ray spectrographs of Nd-glass thermally treated at 1300 ºC for 1 hour in Ar-atmosphere. This glass has an impurity of Fe (26.3 wt%) in area 1 along with Mg, As and Ca as presented in Table 6.7. This region has composition Y-ion deficient on comparing with the initial glass composition. It is known that Fe-impurities are detrimental to the heating of the sample under testing for high power lasing application. The source of this impurity is not clear at present.

Table 6.7: Comparison of various element present in region as marked with Nd-glass composition.

sample	Li	O	Al	Si	Y	Zr	Ti	Nd	Impurity (wt.%)
Nd-glass composition (Wt.%)	1.4	42.0	15.9	17.3	20.5	1.1	0.6	1.3	-
Area-1	4.4	33.2	13.0	18.4	0.3	0.3	0.2	0.5	Fe(26.3), Mg(1.8), Ca (0.9)

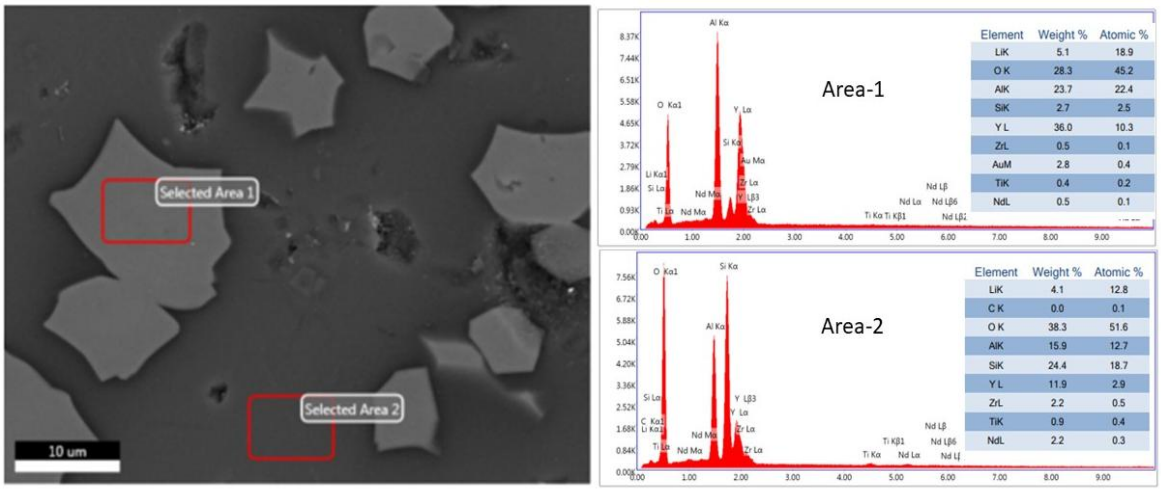

Fig. 6.22: SEM image, EDX spectra and table with weight % of various element present in area 1 and 2 of thermally treated Nd-glass sample.

Fig. 6.22 shows SEM image and the area where EDX spectra is taken during microstructure composition examination. The number with selected area marked on the SEM images corresponds to the EDX spectra shown in fig. 6.22. It is observed

that area 1 (white plate) is Nd-YAG precipitation which has higher Li-concentration. The area 2 is the glass matrix region having composition Li, Si-rich and Y-deficient. This suggests that the glass matrix composition is modified when compared with the original glass composition as shown in Table 6.8.

Table 6.8: Comparison of various element present in region as marked with Nd-glass composition.

sample	Li	O	Al	Si	Y	Zr	Ti	Nd	Impurity (wt.%)
Nd-glass composition (Wt.%)	1.4	42.0	15.9	17.3	20.5	1.1	0.6	1.3	-
Area-1 Plate	5.1	28.3	23.7	2.7	36.0	0.5	0.4	0.5	-
Area-2-Matrix	4.1	38.3	15.9	24.4	11.9	2.2	0.9	2.2	-

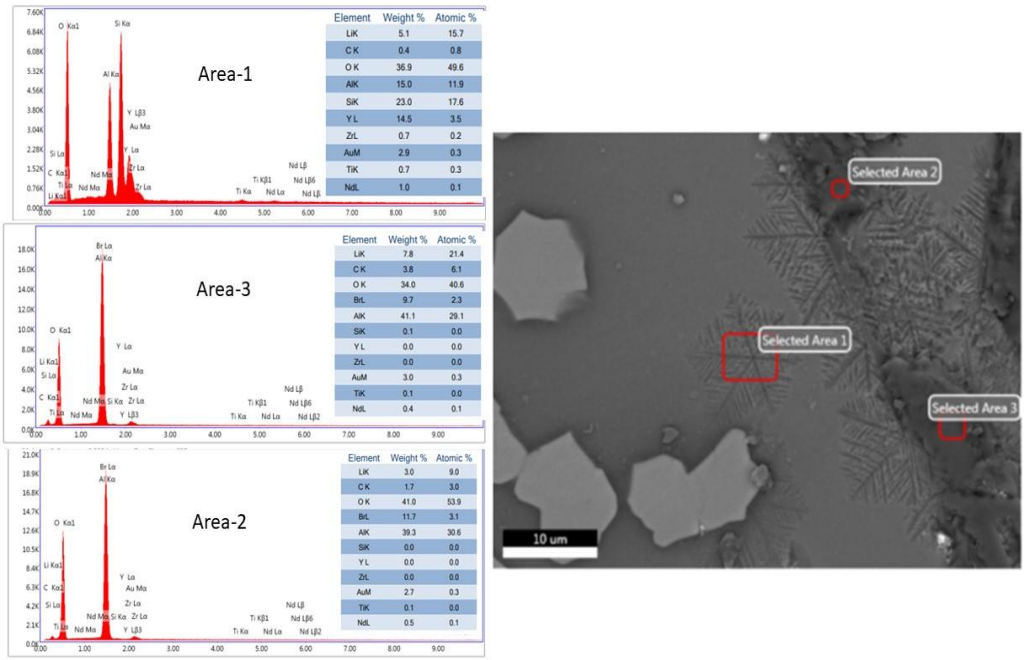

Fig. 6.23: SEM image and EDX spectra of thermally treated Nd-glass (1300 ^{o}C). Area for which the EDX spectra is shown are marked as area 1, 2 and 3. Table in the inset of EDX spectra reveals the element present at the specific area.

Fig. 6.23: reveals the secondary electron images and energy-dispersive X-ray spectrographs of thermally treated Nd-glass at 1300 ^{o}C, where three features are

clearly seen. White precipitates are mainly YAG phase. The area 1 is the area where dendrites are clearly observed, area 2 and 3 are molten regions. Carbon impurities are less compared to the sample annealed at 900 °C. Table 6.9 compares the weight % of the element present at area 1, 2 and 3 with the as-prepared glass composition. Region 1 has composition Li and Si-rich compared to that of the un-heated glass. Region 2 and 3 are mainly Al-rich region with different Li-concentration. Region 3 has higher Li-concentration than that at region 2. It may be noted that this region has no Y or Si element presence.

Table 6.9: Comparison of various element present in region as marked with Nd-glass composition.

sample	Li	O	Al	Si	Y	Zr	Ti	Nd	Impurity (wt.%)
Nd-glass composition (Wt.%)	1.4	42.0	15.9	17.3	20.5	1.1	0.6	1.3	-
Area-1-Dendrite	5.1	36.9	15.0	23.0	14.5	0.7	0.7	1.0	C(0.4)
Area-2	3.0	41.0	39.3	0	0	0	0.1	0.5	C(1.7)
Area-3	7.8	34.0	41.1	0.1	0	0	0.1	0.4	C(3.8)

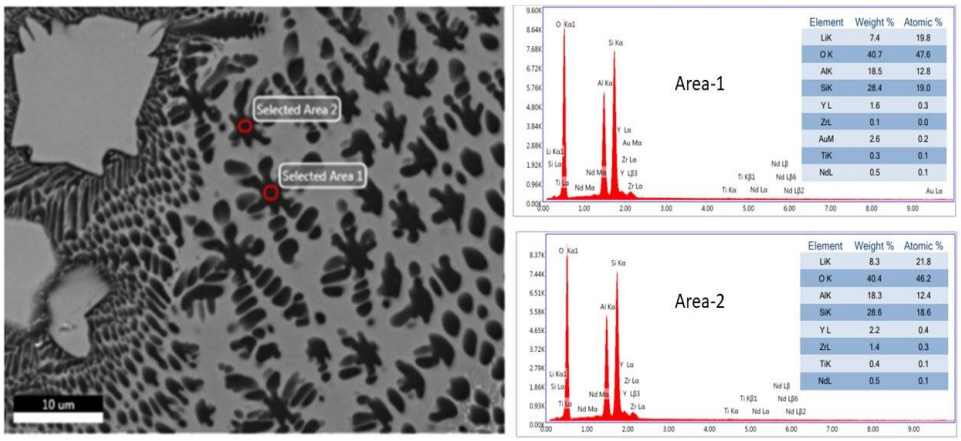

Fig. 6.24: SEM image and EDX spectra of thermally treated Nd-glass (1300 °C). Area for which the EDX spectra is shown are marked as area 1 and 2. Table in the inset of EDX spectra reveals the element present at the specific area.

Fig. 6.24 clearly depicts the dendrites and its compositional analysis. It is clear from the EDX spectra that both regions are identical and has similar concentration of all the elements. Table 6.10 compares the composition of these regions with the glass composition. It is clear that these regions are rich in Li-Al and Si- elements suggesting the presence of $LiAlSi_2O_6$ phase precipitation. This investigation has revealed that precipitation of $LiAlSi_2O_6$ phase is initiated near the surface with mainly Li-diffusion as shown in SEM images of Nd-glass annealed at 900 ^oC sample but the dendrite images in 1300 ^oC thermally treated Nd-glass sample is dissolution of $LiAlSi_2O_6$ phase.

Table 6.10: Comparison of various element present in region as marked with Nd-glass composition.

sample	Li	O	Al	Si	Y	Zr	Ti	Nd	Impurity (wt.%)
Nd-glass composition (Wt.%)	1.4	42.0	15.9	17.3	20.5	1.1	0.6	1.3	-
Area-1-dendrite	7.4	40.7	18.5	28.4	1.6	0.1	0.3	0.5	-
Area-2-densrite	8.3	40.4	18.3	28.6	2.2	1.4	0.4	0.5	-

It will be interesting to examine other sample (heat treated at 1050-1250 ^oC) where second phase ($Y_2Si_2O_7$) is confirmed in XRD analysis. Efforts are being made to carry out the SEM-EDX analysis of these samples.

6.6 Optical Properties

Transmittance and absorbance of light can occur when light passes through or is reflected from a sample. The amount of light absorb is the difference between the incident radiation (I_o) and the transmitted radiation (I) assuming no light scattering loss. The amount of light absorbed is expressed as absorbance. Transmittance, or light that passes through a sample, is usually given in terms of percentage and is defined as follows:

$\%T = I / I_o \times 100$

Absorbance is defined as follows: A = – log T. Here absorbance coefficient is used since the relationship between absorbance and path length is linear.

Fig. 6.26(a-d) shows room temperature UV-visible transmission and absorption coefficient of as fabricated Nd-glass and annealed at 750 ^{o}C. The major absorption bands with peak positions near 525, 585, 680, 750, 800 and 880 nm are seen, which corresponds to spin allowed $^{4}I_{9/2}$ to excited energy level as marked in the fig. 6.26a. This transition is due to electron transitions of Nd^{3+} ion in glass matrix. The details of the energy-level structure of Nd^{3+} ion is shown in Fig. 6.25. It is important to know that width of absorption band at 585 nm consists of a multiplicity of levels where transition from ground state to $^{4}G_{5/2}$ and $^{2}G_{7/2}$ are involved. The adjacent energy levels often overlap in glass matrix because of inhomogeneous local field interaction.

The location, intensity and breadth of the absorption peak bands are due to the interaction of the Nd^{3+} ion with the local crystalline field. These peaks are broad and consistent with the glassy nature of matrix. The intensity of the absorption peaks is different, which suggests the selection of strong absorption of the wavelength suitable for the emission spectra study. The position of the absorption peaks in the spectra is consistent with the absorption by Nd^{3+} ion as reported in the literature. The strong absorption peak near 585 nm is located in the visible regions. The second most intense absorption peak is near 806 nm and generally use for creating population inversion in this material when used as laser host.

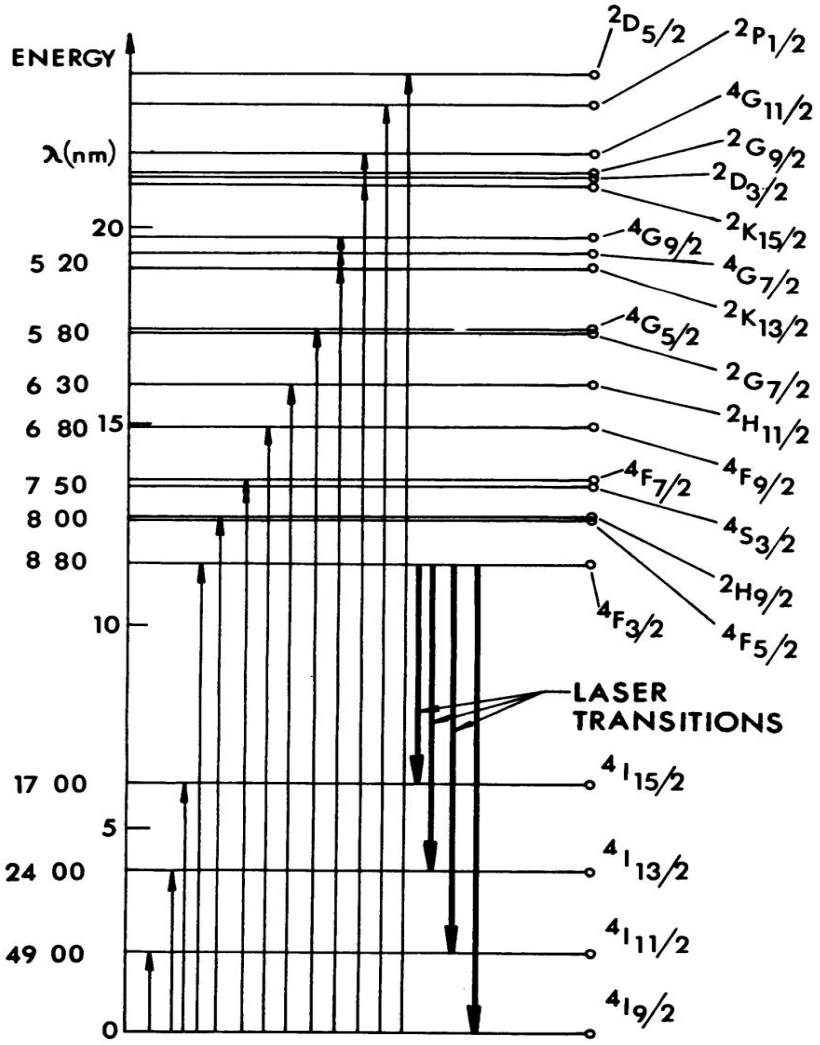

Fig. 6.25: Energy levels of Nd^{3+} ions in glass host.

The absorption coefficient α is calculated from Beer-Lambert's law:

$\alpha = 2.303\ \mathrm{Log}(I_o/I_t)/L$, where L is the thickness of the ceramic in cm.

The background absorption coefficient ~ 0.75 cm^{-1} at 1061 nm is still higher than 0.1% / cm required for lasing. The absorption coefficient, 5.3 cm^{-1} at 350 nm, is higher in the UV region and it decreases with increase in wavelength towards near-IR through visible region. The UV edge is a characteristics of silicate glass and main cause of thermal problems in Nd-silicate glass used as laser host if Xe-flash lamp is used for pumping.

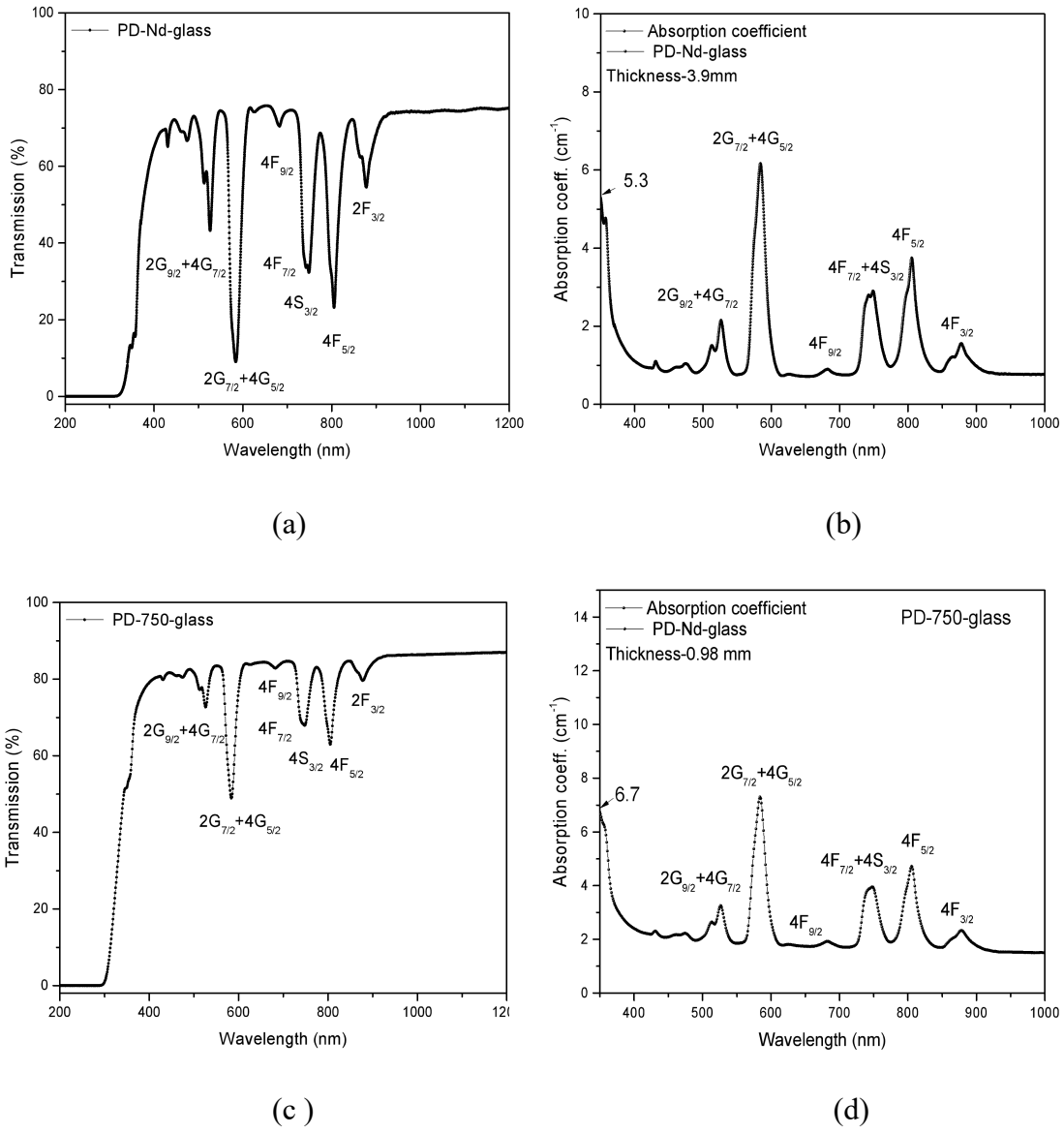

Fig. 6.26: (a, c) Transmission and (b, d) absorption coefficient spectrum of as fabricated Nd-glass and annealed at 750 ^{o}C.

The absorption coefficient for the annealed Nd-glass sample is higher 1.48 cm^{-1}, which is due to the enhanced compositional heterogeneity. The background attenuation "α" coefficient is reported to decrease with reducing absorption contaminants. The Nd-ions emit in the near infrared and in this region absorption are due to impurities metal-ions like Ni, Co, Cu and Fe. By using high purity starting reagents, this absorption coefficient can be further decreased. Optical scattering study has already shown that light is scattered in the Nd-glass rod.

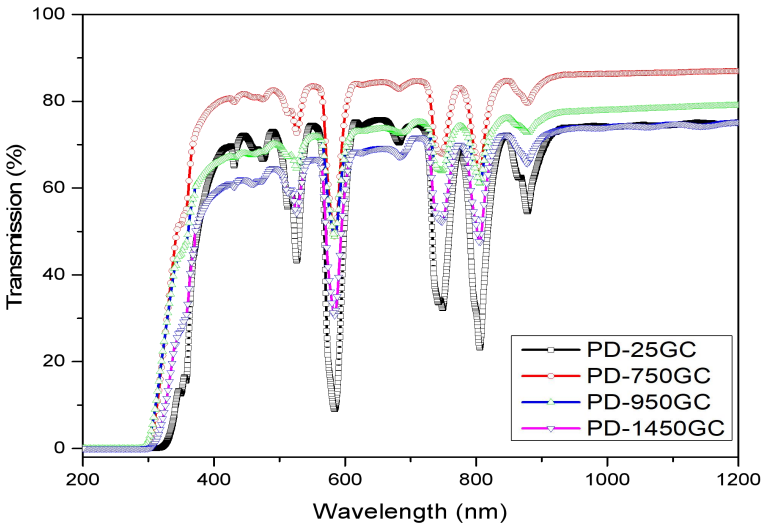

(a)

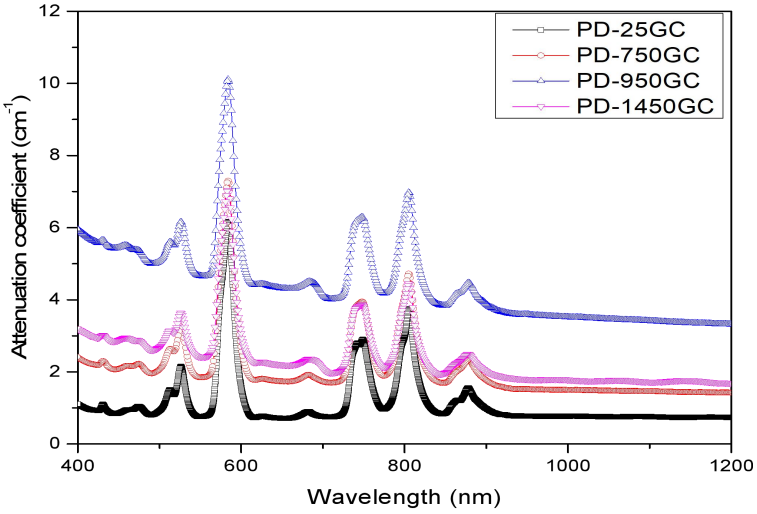

(b)

Fig. 6.27: Transmission and attenuation coefficient of all transparent glass ceramic samples

Fig. 6.27 compares the transmission and attenuation coefficient of Nd-glass, PD-700, PD-950 and PD-1450 samples. All these samples are transparent and only surface precipitation is observed for PD-950 but this sample was transparent in the center part. It may be noted from Fig. 6.27 that near UV-edge 350 nm, the transmission of as prepared Nd-glass is ~ 13% and it increases to ~ 50% with annealing at 750 °C, further annealing decreases it to ~ 44% for PD-950 and to 26% for PD-1450. The background attenuation coefficient is found to increase from 0.75 to

3.45 cm^{-1} with annealing. Higher background attenuation is due to scattering loss inside the annealed sample. With increase in annealing temperature, it is speculated that glass matrix composition is changing, which have resulted in compositional heterogeneities and contributed birefringence losses.

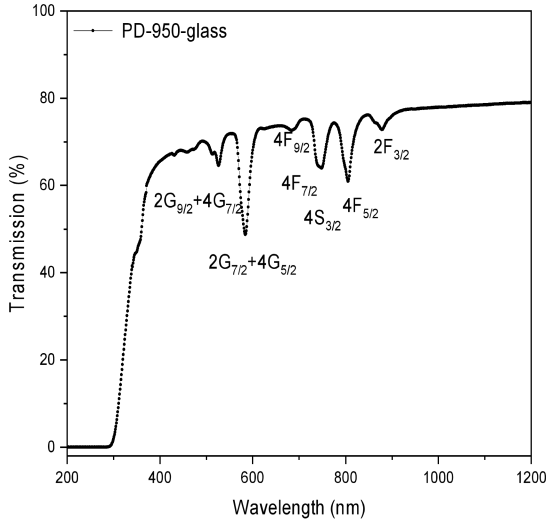

(a)

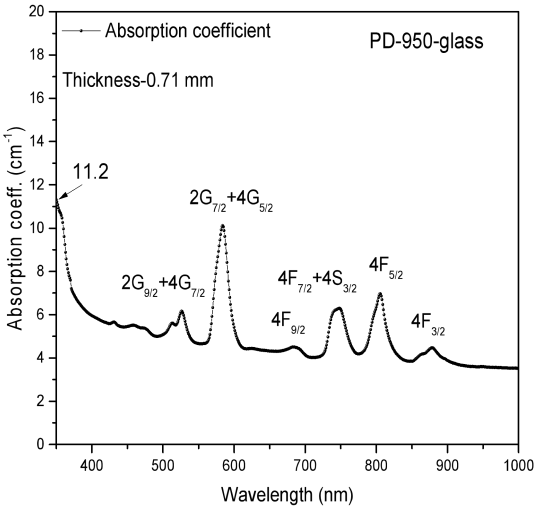

(b)

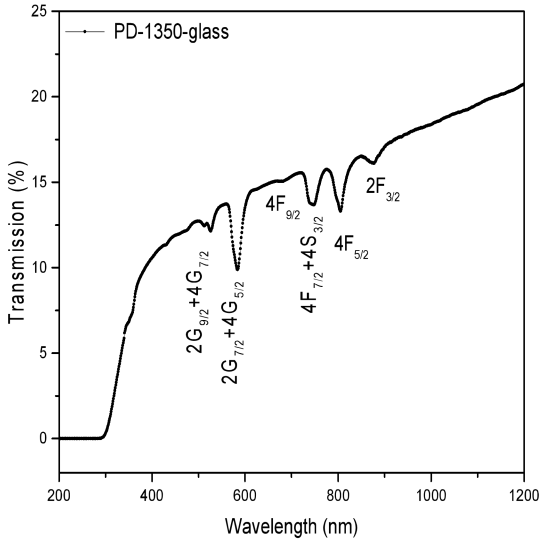

(c)

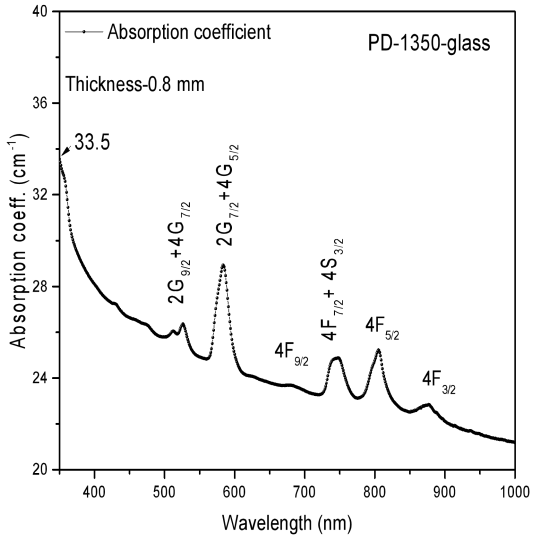

(d)

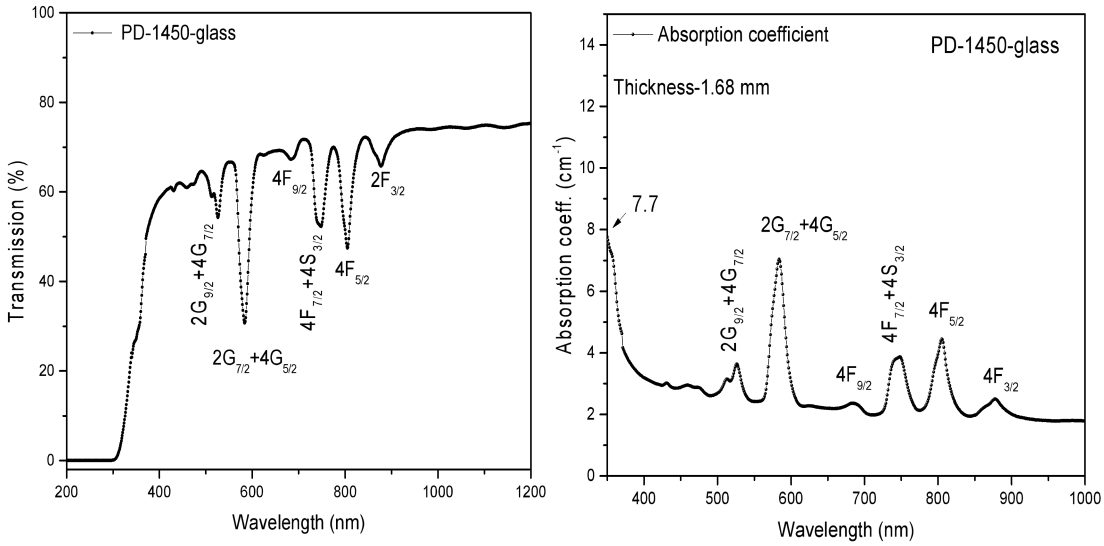

(e) (f)

Fig. 6.28: Transmission and absorption coefficient of Nd-glass heat treated at (a-b) 950, (c-d) 1350 and (e-f) 1450 ^{o}C.

Fig. 6.28(a-f) compares the transmission and absorption spectra of Nd-glass heated to 950, 1350 and 1450 ^{o}C. The sample heated to 1350 ^{o}C show least transmission and the highest 20.71 cm^{-1} background absorption coefficient at 1061 nm. An increase in the background absorption coefficient is due to scattering of light by precipitation inside the glass matrix. The precipitation is observed on the surface in PD-950GC sample and further heating resulted in the precipitation inside the bulk for PD-1050, PD-1150 and PD-1250. All these samples are opaque. Further heating to 1350 ^{o}C has resulted in the dissolution of intermediate phase and transmission increased to 19% for PD-1350. This sample has small crystal of Al_2O_3 as confirmed in the phase analysis. Further heating has resulted in transparent glass having transmission 74.2 % for PD-1450 similar to as-prepared Nd-glass. The background attenuation coefficient of this sample is 1.78 cm^{-1} at 1061nm. Table 6.11 compares the transmission, absorption coefficient at 1061 and 351 nm for different annealed samples.

Table 6.11: Comparison of the optical properties of Nd-glass against heat treated glass

Sample	Transmission (%) @ 1061	Transmission (%) @350 nm	Attenuation coefficient @1061 nm	Attenuation coefficient @ 350 nm
PD-25GL	74.5	13.3	0.7	5.3
PD-750	86.5	51.4	1.5	6.7
PD-950	78.3	44.3	3.4	11.2
PD-1350	19.1	6.8	20.7	33.5
PD-1450	74.2	26.4	1.78	26.4

6.7 Diffuse Reflectance Spectroscopy

Optical absorption for as Nd glass samples has been probed using diffuse reflectance spectroscopy (DRS). The spectra obtained from DRS are converted into equivalent absorption spectra through Kubelka–Munk [13] [14], equations:

$$F(R_\infty) = \frac{(1 - R_\infty)^2}{2R_\infty}$$

where $F(R_\infty)$ is the Kubelka–Munk function ($R_\infty = R_{\text{sample}}/R_{\text{standard}}$), R_{sample} is the diffuse reflectance of the sample, and R_{standard} is the diffuse reflectance of the standard $BaSO_4$ in the present case.

Fig. 6.29 shows the room temperature Diffuse Reflectance spectroscopy data for prepared sample.

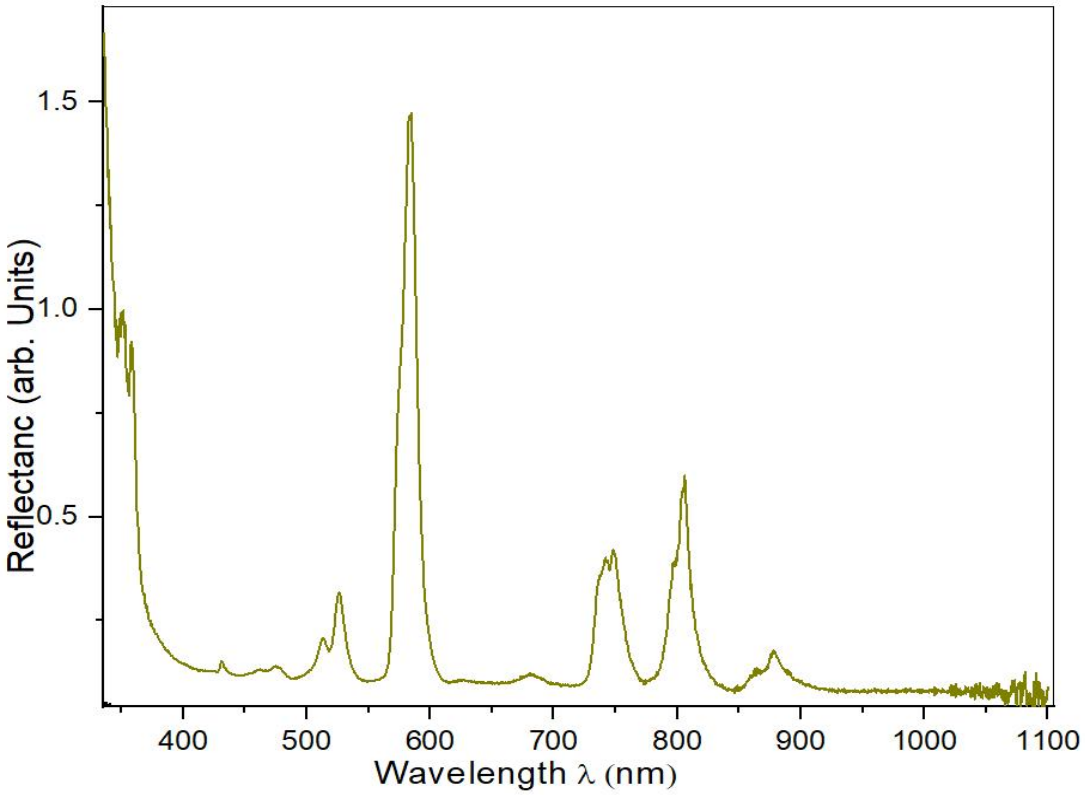

Fig. 6.29: DRS plot of untreated Nd glass Sample

From fig. 6.29 it is clearly visible that the diffuse reflectance spectra resemble with the absorption spectra as shown in figure 6.26(b) and clearly shows the crystal field transitions of Nd ions present in as fabricated sample and similar conclusions and analysis as drawn from transmission spectra may be obtained from the DRS spectra.

6.8 Photoluminescence Spectroscopy

Fig. 6.30 compares room temperature Photoluminescence (PL) emission spectra with an excitation from 585 and 808 nm wavelength. The excited light (585 and 808 nm) is absorbed by the Nd^{3+} ions and gets excited into the excited $^2G_{7/2}$ or $^4F_{5/2}$ states, respectively. The life time of this level is short, thus the excited ion relaxes quickly to the long-lived metastable $^4F_{3/2}$ state. A broad emission line at 1061.8 nm wavelength is clearly seen, which corresponds to the $^4F_{3/2} \rightarrow {}^4F_{11/2}$ transitions as depicted in the energy level diagram shown in inset of fig. 6.30.

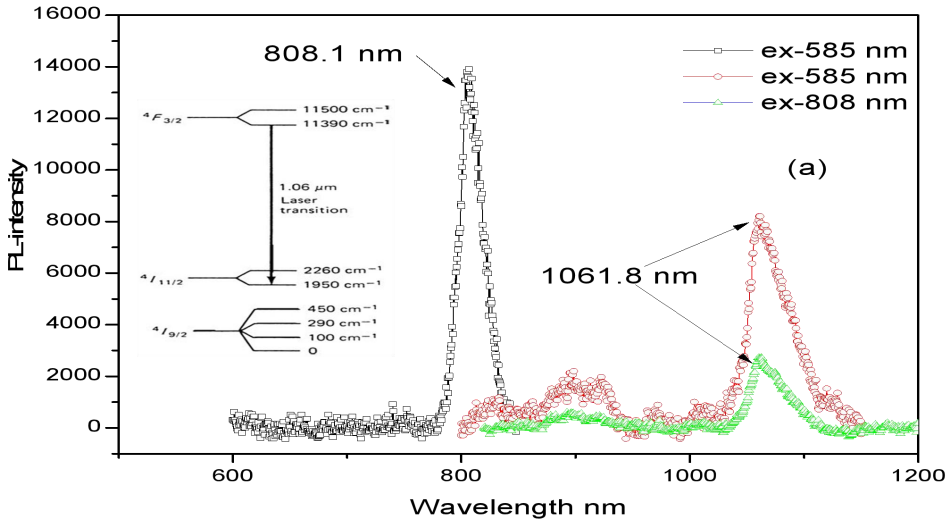

Fig. 6.30: Comparison of Photoluminescence spectra of Nd-glass before heat treatment when excited with 585 and 808 nm wavelength.

The intensity of the PL peak at ~ 1061 seems to depend upon the wavelength of emission light. High energy excitation (using 585 nm) gives approximately three times more intense peak than that for 808 nm. Similarly, the area under this peak is also approximately three times, i.e., ~340000 and ~111000 and the FWHM of 1061 nm PL peak is 39 and 34 nm when excited with 585 and 808 nm wavelength, respectively. Similar results are observed for the PL peak around 880 nm. The peak around 880 nm is broad and corresponds to the $^4F_{3/2} \rightarrow {}^4F_{9/2}$ transitions. The intensity ratio of peak at ~ 880 nm and 1061 nm is 0.26 with 585 nm and 0.24 with 808 nm excitation. The $^4F_{3/2} \rightarrow {}^4F_{9/2}$ transition is a resonant line because it is both absorbed and emitted. A strong PL peak around 808 nm with excitation 585 nm wavelength is a characteristic peak of Nd-ions which has an area ~ 390000 and FWHM = 25nm.

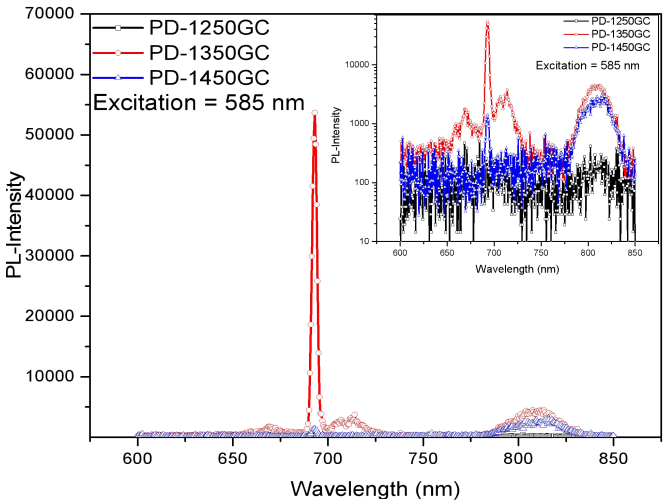
PD-1250GC
PD-1350GC
PD-1450GC
Excitation = 585 nm
PL-Intensity
Wavelength (nm)

(a)

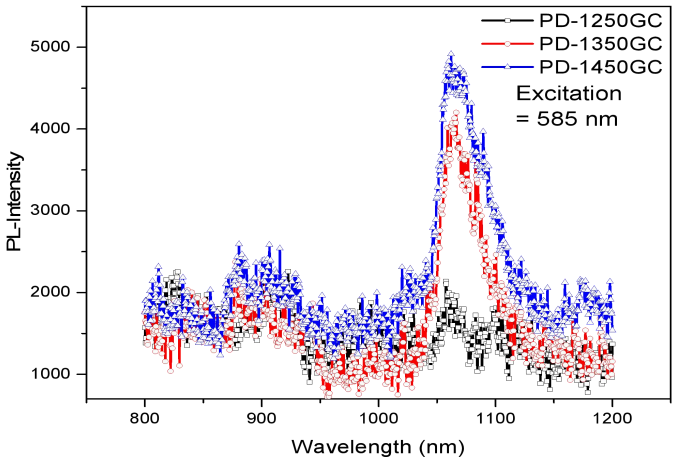
PD-1250GC
PD-1350GC
PD-1450GC
Excitation
= 585 nm
PL-Intensity
Wavelength (nm)

(b)

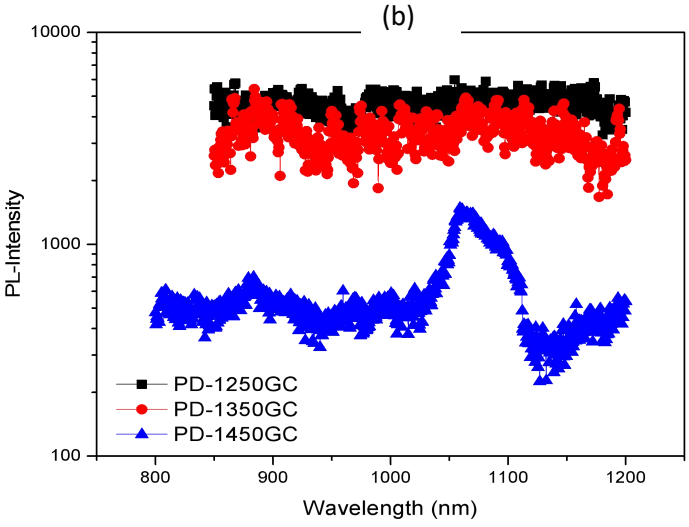
PD-1250GC
PD-1350GC
PD-1450GC
PL-Intensity
Wavelength (nm)

(c)

Fig. 6.31: Comparison of PL spectra for PD-1250, PD-1350 and PD-1450 samples when excited with (a) 585 nm in 600-850 nm wavelength range, (b) 585 nm in 800-1200 nm wavelength range and (c) 808 nm in 800-1200 nm wavelength range.

Fig. 6.31 compares the PL spectra of heat treated Nd-glass at 1250, 1350 and 1450 ^{o}C, when excited with 585 nm in (a) 600-850 nm and (b) 800-1200 nm wavelength range. A sharp peak at 693 nm is clearly seen for PD-1350 sample. The FWHM of this peak is ~ 3 nm and area under this peak is ~ 165000. There are two minor shoulder peak at 669 and 712 nm along with a broad peak at 808 nm. The peak at 808 nm has FWHM ~ 22 nm and area ~ 107000. It may be noticed that the intensity of an extra sharp peak at 693 nm reduces with increasing heat treated temperature (PD-1450). The FWHM remains the same (~ 3.5 nm) but the area under the peak reduces drastically to ~ 4600. No such extra peak is observed for PD-1250 sample. Inset of the fig6.30a shows the same plot in logarithmic Y-scale, which clearly depicts the presence of a peak at 808 nm for PD-1250.

Fig. 6.31b compares the PL-spectra of PD-1250, PD-1350 and PD-1450, when excited with 585 nm in 800-1200 nm wavelength range. Two broad peaks at 880 and 1061 nm are due to transition from the $^{4}F_{3/2} \rightarrow {}^{4}F_{11/2}$ and the $^{4}F_{3/2} \rightarrow {}^{4}F_{9/2}$ levels are clearly shown for PD-1350 and PD-1450 compared to that of PD-1250. The peak at 1061 nm is asymmetrically broad having similar intensity ~ 3200 and 3400. Other peak characteristics like FWHM and peak area is more 42 (35) and 167000 (137000) for PD-1450 (PD-1350).

Fig. 6.31c compares the PL-spectra of PD-1250GC, PD1350GC and PD1450GC, when excited with 808 nm in 800-1200 nm wavelength range. It is observed that no distinct peak is observed at 880 and 1061 nm for PD-1250 and PD-1350 samples. These two peaks for PD-1450 has an intensity ratio 0.25. The FWHM is 11 and 49 nm and area under the peak is 56200 and 9900 for the peak at 880 and 1061 nm, respectively.

This investigation clearly shows that an extra peak (at 693 nm) is observed for heat treated Nd-glass at 1350 and 1450 ^{o}C compared to as-prepared Nd-glass as shown in Fig. 6.32a-c. The peak intensity at 800 nm decreases with heat treatment. Table 6.12, Table 6.13 and Table 6.14 compares the peak characteristics of major PL peaks with heat treatment. It may be noted that X-ray diffraction pattern has shown no

major phase precipitation. Thus all three samples are mainly glass but has different optical characteristics.

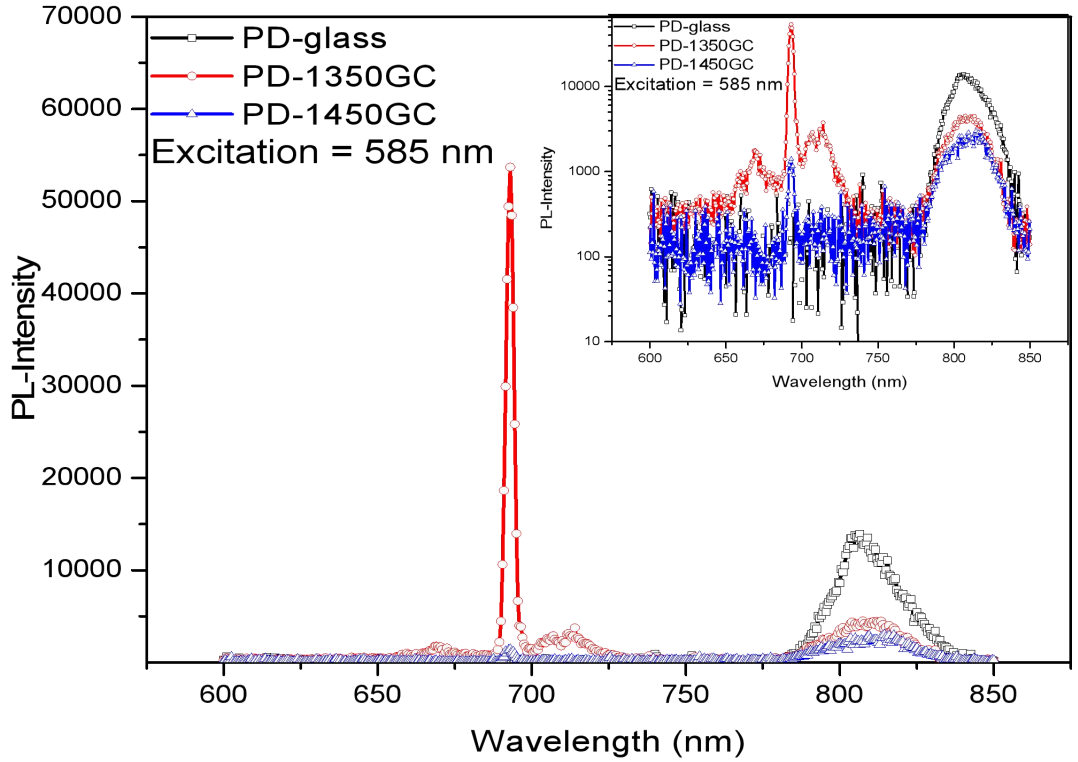

(a)

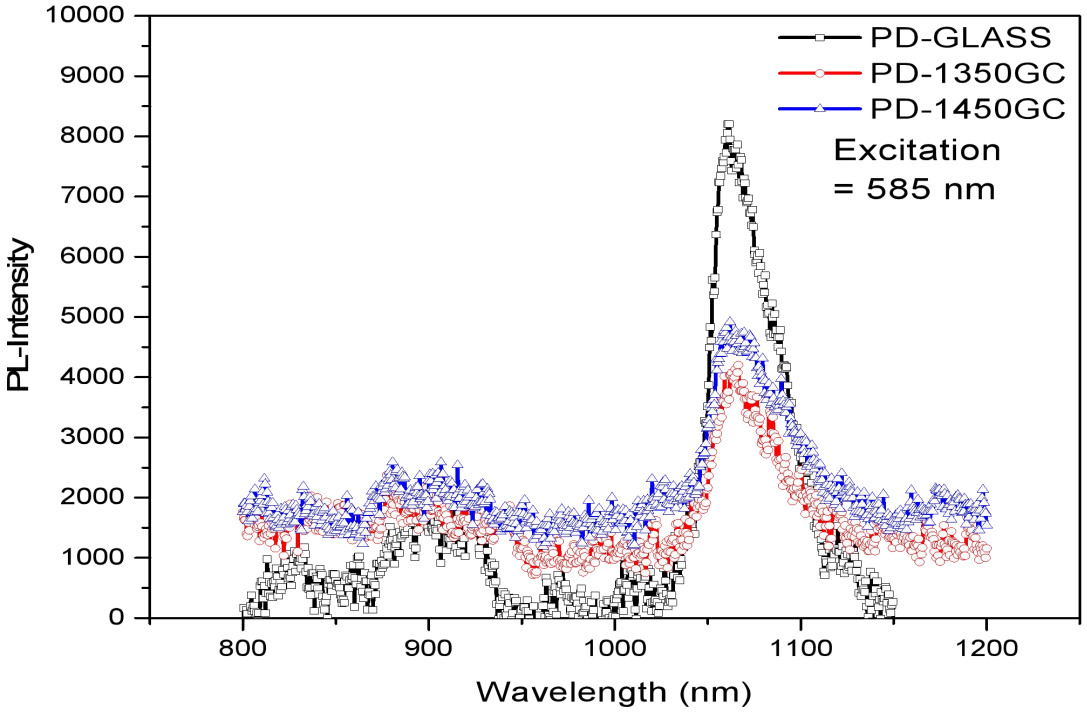

(b)

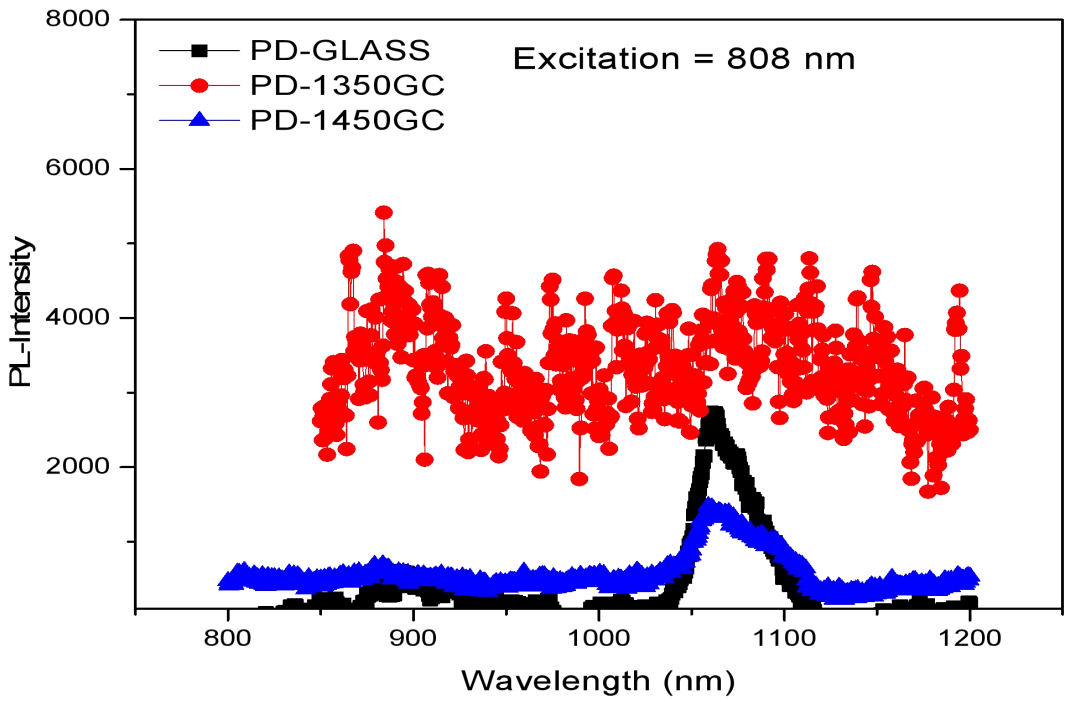

(c)

Fig. 6.32: PL spectra details for Nd-glass, PD1350 and PD1450 when excited with (a) 585 nm in 600-850 nm, (b) 585 nm in 800-1200 nm and (c) 808 nm in 800-1200 nm wavelength range.

Table 6.12: Comparison of PL-peak intensity at 585 and 808 nm in wavelength range 600-800 and 800-1200 nm for Nd-glass against PD-1350 and PD-1450 samples.

Intensity / Sample	Nd-glass	PD-1350	PD-1450
Intensity @ 808 -ex-585nm-WR-600-800 nm	14331	4215	2849
Intensity @ 880 -ex-585nm-WR-800-1200 nm	2174	1188	1124
Intensity @ 1061-ex-585nm-WR-800-1200 nm	8167	3215	3391
Intensity @ 880 -ex-808nm-800-1200 nm	691	2773	290
Intensity @ 1061 -ex-808nm-800-1200 nm	2883	2393	1167

Table 6.13: Comparison of PL-peak FWHM at 585 and 808 nm in wavelength range 600-800 and 800-1200 nm for Nd-glass against PD-1350 and PD-1450 samples.

FWHM / Sample	Nd-glass	PD-1350	PD-1450

FWHM @ 808 -ex-585nm-WR-600-800 nm	25	22	18
FWHM @ 880 -ex-585nm-WR-800-1200 nm	13	9	13
FWHM @ 1061-ex-585nm-WR-800-1200 nm	39	-	42
FWHM @ 880 -ex-808nm-800-1200 nm	33	-	11
FWHM @ 1061 -ex-808nm-800-1200 nm	34	-	49

Table 6.14: Comparison of PL-peak area at 585 and 808 nm in wavelength range 600-800 and 800-1200 nm for Nd-glass against PD-1350 and PD-1450 samples.

Sample	Nd-glass	PD-1350	PD-1450
Area @ 808 -ex-585nm-WR-600-800 nm	388079	106807	75124
Area @ 880 -ex-585nm-WR-800-1200 nm	88740	-	36192
Area @ 1061-ex-585nm-WR-800-1200 nm	339984	-	166954
Area @ 880 -ex-808nm-800-1200 nm	28986	-	9930
Area @ 1061 -ex-808nm-800-1200 nm	111023	-	56248

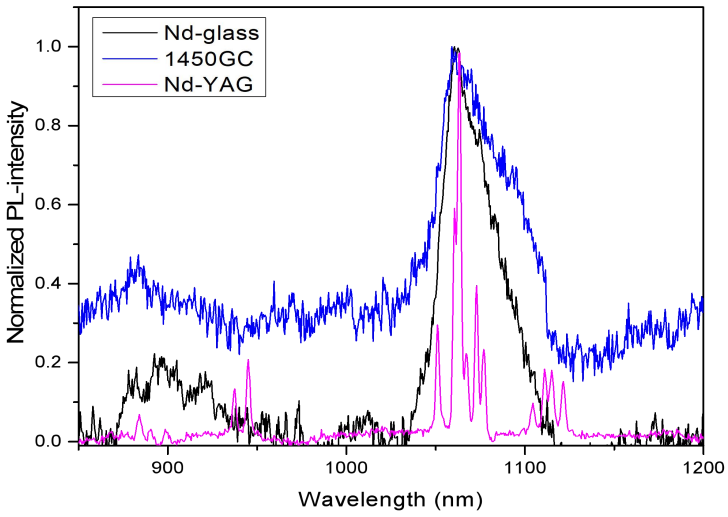

Fig. 6.33: Comparison of PL-spectra for Nd-glass and heat treated Nd-glass (1450 ^{o}C) with Nd-YAG polycrystalline ceramic.

Fig. 6.33 compare the PL-spectra of Nd-glass as prepared and PD-1450 with Nd-YAG prepared using solid state route. All the characteristics peak of Nd^{3+} ions in YAG lattice for polycrystalline sample is well defined and sharp, which is consistent

with the earlier reports. As-prepared Nd-glass and PD-1450 shows broad emission peak at the same wavelength. High background emission for PD-1450 shows substantial amount of scattering inside the sample.

The emission peak characteristics at 808, 880 and 1061 nm become less intense with thermal treatment. A strong extra emission peak for PD-1350 at 693 nm is characteristic “R-line” of Cr-doped Alumina. Since these peaks are missing in the Nd-glass, it is highly impossible that starting reagents might have some Cr-impurity. At present, it is not clear why a sharp emission peak is present in the annealed sample but it is related to the Al_2O_3 phase because X-ray analysis has confirmed the presence of this phase. It is believed that Nd-ion may have different surrounding environment in the thermally treated Nd-glass, which is due to the precipitation phase and its solubility.

Chapter 7

Conclusions

7.1 Conclusions

Development of transparent ceramic becomes more challenging with increase in size. The laser active Nd-ion when added in glass matrix as laser host is better in term of large size fabrication but Nd-glass has poor thermal conductivity compared to YAG crystal. The present work is carried out to combine size advantages of Nd-glass with excellent thermal conductivity of YAG by precipitating YAG phase in glass. Following conclusions are made during this investigation.

- A rod of Nd-doped silicate glass based on yttrium-lithium-aluminum-silicate was fabricated using melt and quench technique. The glass had absorption coefficient 0.72 cm^{-1} and ~ 75 % transmission at 1061 nm wavelength. The absorption peaks were assigned based on the transition from the ground state $^4I_{9/2}$ to the crystal field state consistent with earlier report. The emission spectra of Nd-glass disclosed a broad peak at 1061 nm when excited with 808nm wavelength, which is consistent with its glassy nature.
- The phases precipitation sequence studied using X-ray diffraction technique, revealed the precipitation of the β-spodumene ($LiAlSi_2O_6$) phase at the surface first around 950 ^oC and then $Y_2Si_2O_7$ phase in the bulk around 1050 ^oC, followed by YAG phase around 1100 ^oC. Single major YAG phase was successfully observed in the 1350 ^oC for 6 hours heat treated PD-1350 sample.
- Vibrational spectroscopic investigation had also revealed additional absorption band consistent with the phase analysis. Sudden change in the thermal expansion and mechanical hardness measured on the heat treated samples were consistent with this phase evolution sequence.
- Microstructure and composition investigation had revealed these phases present in the glass matrix of Pd-900 and PD-1300 glass ceramic samples. Composition analysis has shown an importance of Li-ions diffusion in the precipitation of the β-spodumene phase.
- Photoluminescence measurement clearly showed all the emission peak related to Nd-ions in glass matrix. An extra sharp peak is observed for PD-1350, which is found to be characteristics R-line of Cr-doped Alumina. No chromium ion impurity was present in the Nd-glass, as the R-line was missing

in the PL spectra of as-fabricated glass. At present the origin of these peaks are not known.

References

[1] Ikesue, A., Kamata, K., & Yoshida, K. (1995). Fabrication and optical properties of high-performance polycrystalline Nd:YAG ceramics for solid-state lasers. *Journal of the American Ceramic Society, 78*(4), 1033–1040. https://doi.org/10.1111/j.1151-2916.1995.tb08306.x

[2] Ikesue, A., Kamata, K., & Yoshida, K. (1996). Effects of neodymium concentration on optical characteristics of polycrystalline Nd:YAG laser materials. *Journal of the American Ceramic Society, 79*(7), 1921–1926. https://doi.org/10.1111/j.1151-2916.1996.tb08766.x

[3] Apetz, R., & van Bruggen, M. P. B. (2003). Transparent alumina: A light-scattering model. *Journal of the American Ceramic Society, 86*(3), 480–486. https://doi.org/10.1111/j.1151-2916.2003.tb03325.x

[4] Greskovich, C., & Chernoch, J. P. (1973). Polycrystalline ceramic lasers. *Journal of Applied Physics, 44*(10), 4599–4606. https://doi.org/10.1063/1.1660971467

[5] Fujita, S., & Tanabe, S. (2010). Fabrication, microstructure and optical properties of Er^{3+}:YAG glass–ceramics. *Optical Materials*, *32*(7), 886–891. https://doi.org/10.1016/j.optmat.2010.01.014

[6] Nishi, M., Tanabe, S., Fujita, K., Hirao, K., & Pezzotti, G. (2004). Phase-selective cathodoluminescence spectroscopy of Er:YAG glass- ceramics. *Solid State Communications, 132*(1),1923. https://doi.org/10.1016/j.ssc.2004.06.022

[7] Beall, G. H., & Duke, D. A. (1969). Transparent glass-ceramics. Journal of Materials Science, 4(4), 340–352. https://doi.org/10.1007/BF00552246

[8] Rosenflanz, A., Frey, M., Endres, B., Anderson, T., Richards, E., & Schardt, C. (2004). Bulk glasses and ultrahard nanoceramics based on alumina and rare-earth oxides. *Nature, 430*(7002), 761–764.https://doi.org/10.1038/nature02755

[9] Ma, X., Li, X., Li, J., Genevois, C., Ma, B., Etienne, A., Wan, C., Véron, E., Peng, Z., & Allix, M. (2018). Pressureless glass crystallization of transparent yttrium aluminum garnet-based nanoceramics. *Nature Communications, 9*, Article 1175. https://doi.org/10.1038/s41467-018-03467-7

[10] Li, P. G., Lei, M., & Tang, W. H. (2010). Raman and photoluminescence properties of α-Al_2O_3 microcones with hierarchical and repetitive superstructure. *Materials Letters, 64*(2), 161–163. https://doi.org/10.1016/j.matlet.2009.10.025

[11] Gui, Y., Yang, Q., Shao, Y., & Yuan, Y. (2017). Spectroscopic properties of neodymium-doped alumina (Nd^{3+}:Al_2O_3) translucent ceramics. Journal of Luminescence, 184, 232–234. https://doi.org/10.1016/j.jlumin.2016.12.022

[12] Krishnan, R., Kesavamoorthy, R., Dash, S., Tyagi, A. K., & Raj, B. (2003). Raman spectroscopic and photoluminescence investigations on laser surface modified α-Al_2O_3 coatings. Scripta Materialia, 48(8), 1099–https://doi.org/10.1016/S1359-6462(02)00513-9

[13] Yang, Y., & Kruse, B. (2004). Revised Kubelka–Munk theory. I. Theory and application. *Journal of the Optical Society of America A, 21*(10), 1933–1941. https://doi.org/10.1364/JOSAA.21.001933

[14] Kubelka, P. (1948). New contributions to the optics of intensely light-scattering materials. Part I. *Journal of the Optical Society of America, 38*(5), 448–457. https://doi.org/10.1364/josa.38.000448